2018

A Broadly Tunable Surface Plasmon-Coupled Wavelength Filter for Visible and Near Infrared Hyperspectral Imaging

Ajaykumar Zalavadia

A BROADLY TUNABLE SURFACE PLASMON-COUPLED WAVELENGTH FILTER FOR VISIBLE AND NEAR INFRARED HYPERSPECTRAL IMAGING

AJAYKUMAR ZALAVADIA

Bachelor of Pharmacy
Rajiv Gandhi University of Health Sciences
2007

Master of Science in Analytical Chemistry
Governors State University
2009

Submitted in partial fulfillment of the requirements for the degree
DOCTOR OF PHILOSOPHY IN CLINICAL AND BIOANALYTICAL CHEMISTRY
at the
CLEVELAND STATE UNIVERSITY
May 2018

We hereby approve this dissertation for

Ajaykumar H. Zalavadia,

Candidate for the Doctor of Philosophy in Clinical-Bioanalytical Chemistry degree for the Department of Chemistry and Cleveland State University's College of Graduate Studies

_____ Date: _____

Dr. John F. Turner II, Department of Chemistry

(Dissertation Committee Chairperson)

_____ Date: _____

Dr. David W. Ball, Department of Chemistry

(Dissertation Committee Member)

_____ Date: _____

Dr. Mekki Bayachou, Department of Chemistry

(Dissertation Committee Member)

_____ Date: _____

Dr. Baochuan Guo, Department of Chemistry

(Dissertation Committee Member)

_____ Date: _____

Dr. Petru S. Fodor, Department of Physics

(Dissertation Committee Member)

Date of Defense: March 8th, 2018

Dedicated to Bansari…

ACKNOWLEDGEMENT

I am eternally grateful to my advisor Dr. John F. Turner, II for his invaluable guidance since 2010, neither a thank you, nor this acknowledgement is enough to gratify your contribution in making the person I am today. I will try my very best to not let you down ever.

I would like to thank Dr. Petru S. Fodor, for giving me the opportunity to serve as a graduate assistant for the scanning electron microscopy facility, through which I also have received financial support during my dissertation research work.

I would like to express my gratitude to my committee members Dr. David Ball, Dr. Mekki Bayachou, Dr. Baochuan Guo, and Dr. Taysir Nayfeh for their suggestions about my research during my candidacy and annual reports. I would also like to thank the Department of Chemistry for providing me the opportunity to be a teaching assistant to advance my teaching skills, the College of Sciences for awarding me the Doctoral Dissertation Research Award for 2014 and the Cleveland State University's college of graduate studies for giving me the opportunity to advance my career and pursue a doctorate degree.

Dear Mom, Dad and Bansari, I will be forever in debt for your unconditional love during the good and the bad times of my life and never giving up on me, without your emotional and financial support I would not have been able to pursue my dreams.

I am thankful to my friends and colleagues for all the productive, and non-productive but fun; time spent together on campus or off campus. You know who you are without being named individually.

A BROADLY TUNABLE SURFACE PLASMON-COUPLED WAVELENGTH FILTER FOR VISIBLE AND NEAR INFRARED HYPERSPECTRAL IMAGING

AJAYKUMAR ZALAVADIA

ABSTRACT

Hyperspectral imaging is a set of techniques that has contributed to the study of advanced materials, pharmaceuticals, semiconductors, ceramics, polymers, biological specimens, and geological samples. Its use for remote sensing has advanced our understanding of agriculture, forestry, the Earth, environmental science, and the universe. The development of ultra-compact handheld hyperspectral imagers has been impeded by the scarcity of small widefield tunable wavelength filters. The widefield modality is preferred for handheld imaging applications in which image registration can be performed to counter scene shift caused by irregular user motions that would thwart scanning approaches. In the work presented here an electronically tunable widefield wavelength filter has been developed for hyperspectral imaging applications in the visible and near-infrared region. Conventional electronically tunable widefield imaging filter technologies include liquid crystal-based filters, acousto-optic tunable filters, and

electronically tuned etalons; each having its own set of advantages and disadvantages. The construction of tunable filters is often complex and requires elaborate optical assemblies and electronic control circuits. I introduce in the work presented here is a novel widefield tunable filter, the surface plasmon coupled tunable filter (SPCTF), for visible and near infrared imaging. The SPCTF is based on surface plasmon coupling and has simple optical design that can be miniaturized without sacrificing performance. The SPCTF provides diffraction limited spatial resolution with a moderately narrow nominal passband (<10 nm) and a large spurious free spectral range (450 nm-1000 nm).

The SPCTF employs surface plasmon coupling of the π-polarized component of incident light in metal films separated by a tunable dielectric layer. Acting on the π-polarized component, the device is limited to transmitting 50 percent of unpolarized incident light. This is higher than the throughput of comparable Lyot-based liquid crystal tunable filters that employ a series of linear polarizers. In addition, the SPCTF is not susceptible to the unwanted harmonic bands that lead to spurious diffraction in Bragg-based devices. Hence its spurious free spectral range covers a broad region from the blue through near infrared wavelengths. The compact design and rugged optical assembly make it suitable for hand-held hyperspectral imagers. The underlying theory and SPCTF design are presented along with a comparison of its performance to calculated estimates of transmittance, spectral resolution, and spectral range. In addition, widefield hyperspectral imaging using the SPCTF is demonstrated on model sample.

TABLE OF CONTENTS

LIST OF FIGURES

CHAPTER 1

INTRODUCTION

Hyperspectral imaging (HSI), known also as chemical or spectroscopic imaging, has emerged as a technique that integrates conventional imaging and spectroscopy to attain both spatial and spectral information from the sample. By integrating wavelength selection devices with imaging optics and sensitive detectors, HSI enables spectral information from each assigned pixel location on a sample or target location to be recorded. Hyperspectral data is rich with information content and has outstanding feature identification potential, which makes it highly suitable for numerous applications. Hyperspectral imagers have been developed for every optical region of the electromagnetic spectrum to measure variations in the absorption, emission, transmittance, reflectance, fluorescence and scattering of light by complex samples. To

accommodate this broad range of modalities, HSI instruments are custom-designed for specific applications.

HSI can be performed in a few different modalities; point mapping, line scanning, widefield spectral imaging, and spatial or wavelength multiplexing are common approaches. Regardless of its implementation, HSI produces a set of spectra in which each spectrum corresponds to an assigned location on or in the sample, such as the set of pixel locations corresponding the field of view within some image plane. A necessary capability of HSI instruments is wavelength tuning. For widefield HSI, electro-optic devices like the acousto-optic tunable filter (AOTF), liquid crystal tunable filter (LCTF) and Fabry-Perot tunable filter (FPTF) are frequently used to provide wavelength selection.[1-7] Besides the use of traditional optical filters, a few specialized solutions like the resonance ionization imaging detector (RIID), hybrid holographic-liquid crystal filters, and photonic crystals have been developed for the same purpose.[8-12]

The work presented here introduces a novel widefield tunable filter for visible and near infrared region based on surface plasmon coupling. The surface plasmon coupled tunable filter (SPCTF) is designed to leverage advances in consumer-based technologies so that HSI can be miniaturized and incorporated into compact devices for handheld and airborne applications. As part of this work the design and construction of the SPCTF is presented along with a theoretical description of surface plasmon generation in thin metal films. Experimental reflectance data as a function of wavelength and incident angle with respect to the metal film, deposited on a glass prism in the Kretschmann-Raether configuration, is presented along with theoretical estimates for comparison. Wavelength tuning using a coupled surface plasmon interaction in a symmetric cavity created by

closely juxtaposing two prisms with their coated hypotenuses facing each other across as airgap has been demonstrated. Using this configuration as the basis of the SPCTF design, HSI using the SPCTF has been demonstrated for the first time and the transmittance and bandpass values as a function of wavelength are provided. By exploiting the sensitivity of surface plasmon generation to the angle of incident light, a narrow passband SPCTF is presented. The bandpass and acceptance angle of the narrow passband device are given along with a brief discussion of the relationship between short-range and long-range surface plasmons in the SPCTF.

Significance: Hyperspectral imaging has emerged as a powerful tool for noninvasive and nondestructive characterization of complex samples. The integration of HSI with optical microscopy is often performed in the laboratory setting to map compositional changes in heterogeneous samples. Of the many spectroscopic methods that can be integrated with HSI, the most chemically specific ones are Raman scattering and infrared (IR) absorption or reflectance. Collectively referred to as vibrational spectroscopies, Raman and IR spectra reveal detailed information regarding the vibrational/rotational band structure of molecules. In recent years, advances in instrumentation have led to small, battery powered, handheld Raman spectrometers. Unlike the IR modality, little or no sample preparation is needed for Raman analysis. Hence these portable systems enable point-and-shoot sample identification in the field. The development of portable widefield Raman imagers has been more challenging and practical devices are not yet available. The main impediment to the introduction of compact Raman imagers is the development of efficient narrowband tunable filters. The

development of the SPCTF described here is a first step towards the creation of compact Raman imaging system based on surface plasmon coupling.

1.1 Hyperspectral Imaging

Hyperspectral imaging has originated from remote sensing and has been explored for various applications.[13] The HSI approach simultaneously delivers chemical and spatial information from the sample by generating a spatial map of spectral variations by combining imaging with spectroscopy, HSI not only allows important extrinsic characteristics of the sample (i.e. size, geometry, appearance, color, etc.) to be revealed through image feature extraction, it also enables the identification of chemical constituents of the sample through spectral analysis.[6, 14] The HSI offers many advantages over conventional analytical methods. It is a noninvasive, noncontact and non-destructive method for which no sample preparation is inherently required. It is therefore more economic than traditional methods, due to the savings in labor, time, supplies and reagent cost associated with intensive sample preparation. By acquiring spectral and spatial information simultaneously, HSI enables a more complete description of constituent concentration and distribution throughout heterogeneous samples than single channel techniques.

The ability to identify the spatial distributions of chemical and physical components in a sample makes HSI useful for biomedical[15-19], pharmaceutical[20-22], agriculture[23-26], remote sensing[13, 27-30], archeology[31-38], forensic[39-44], food quality[21, 26, 45-56], astronomy[57-66], defense[67-77] and other industrial applications, many of which have yet to be discovered.

1.1.1 Hyperspectral Imaging for Remote Sensing

Spectral imaging was originally substantiated within the remote sensing fields, such as airborne surveillance and satellite imaging. It has been successfully applied to application in mining and geology, agriculture, forestry, defense, environmental, and climate change research. For example, the airborne visible infrared imaging spectrometer (AVIRIS) is a premier instrument in the earth remote sensing and delivers 224 contiguous spectral bands in the wavelength range between 400 nm and 2500 nm.[78, 79] The AVIRIS has enabled study of water vapor maps to be generated above lakes over large time periods[80], wild fire damage assessment[81, 82], mineral mapping[83-85], the mapping of oil spills and residua spread on sea surfaces[86-88], and the environmental impact of active and abandoned mine lands[84] have all benefitted from AVIRIS remote sensing.

Forestry: The HSI has enabled the identification of tree species[89], the assessment of canopy health[90, 91], the determination of water content as well as relative abundances of photosynthetic and non-photosynthetic vegetation for the forestry research.[92, 93] Chemometric techniques were used on hyperspectral data acquired by AVIRIS over the Harvard Forest to identify plant species based on nitrogen and lignin content in the foliage.[94, 95]

Vegetation and Soil Resource Control: Airborne HSI has been employed in various agricultural application. With the use of HSI, crop variables such as wet biomass[96], leaf area index[97], plant height[98], grain yield[99], and chlorophyll content of plants can be quantified.[100] Mineralogical composition of soil, crop moisture assessment, crop yield modeling, carbon flux assessment from vegetation, and discrimination of crop residues from soils can also be estimated using HSI.[101, 102]

Environmental Analysis: Environmental studies have also benefited from the use of HSI. For example, the identification of waste piles with the potential to leach heavy metals into water streams and ground water was determined by AVIRIS data at Leadville, CO. Ultimately, millions of dollars were saved in cleanup costs.[84] Data from another HSI platform, advanced spaceborne thermal emission and reflection radiometer (ASTER) was used to create detailed maps of land surface temperature, reflectance and elevation. Hyperspectral data from airborne (i.e. AVIRIS) and spaceborne (i.e. ASTER) imagers helps environmental scientists achieve a more complete understanding of the Earth's response to change, and to better predict variability and trends in climate, weather, and natural hazards.

Climate: For over 30 years, NASA has flown instruments in space to aid our understanding of climate. Satellites equipped with hyperspectral imagers provide information about weather, carbon emission, air quality and many other factors that help us understand the Earth's climate. The Geostationary Carbon Observatory (GeoCarb) built by NASA's Jet Propulsion Laboratory (JPL) set to launch in 2020 will collect concentration of carbon dioxide, methane, carbon monoxide and solar-induced fluorescence.

Astronomy: The gorgeous images of stars and galaxies that are often published by NASA are almost never simple three channel (red, green, and blue) images but are the result of a spectral image data that has undergone extensive processing before being recast in pseudo-color. Spaceborne telescopes equipped with the ability to capture spectral images helps us understand the chemistry of distant stars and galaxies. The Chandra, NASA's flagship mission for X-ray astronomy, observes X-rays from clouds of

gases in space. For the spectral images captured by the Hubble, spectral shapes are used to previously reveal hidden astronomical objects. Peaks and dips at specific wavelengths in a spectrum indicate the presence of elements like carbon, oxygen, hydrogen, and iron among others.

Defense: Geospatial intelligence (GEOINT) provides information about human activity by collecting data from various sources. Landsat, remote sensing and radar data are often employed by GEOINT to provide terrain information to military troops stationed overseas. Landsat provides the longest temporal record of multispectral data of the Earth's surface on a global basis. Geospatial intelligence data is used for targeting, guiding missiles, damage assessment, navigating in foreign terrain, and espionage.

Surveillance: Airborne surveillance is routinely used in applications related to border protection, homeland security, command and control or even maritime surveillance. High resolution infrared imaging used in airborne surveillance activities provide valuable information regarding target shapes, temperatures and chemical nature. The spectral information provided by the infrared HSI adds selectivity and efficiency to the task of detecting and identifying ground targets based on their unique spectral signature.[103] Hyperspectral video cameras developed by Rebellion Photonics have also been employed for the real-time surveillance of oilfields, refineries, drilling sites and tanker filling sites to detect methane leaks as a means to lower methane emissions, prevent loss and prevent accidental casualties.[104]

1.1.2 Hyperspectral Imaging for Microscopy and Macroscopy

Traditional RGB cameras like the ones used for photography and video surveillance, bin the wavelength information into 3 broad spectral bands corresponding to red, green and blue. Combining HSI with optical microscopy enables the determination of the spatial and spectral characteristics of a specimen for each pixel in an image. As a result, HSI has become an attractive and powerful method for detailed nondestructive investigation of chemical distribution, in complex small heterogeneous samples. Various application areas include, but are not limited to, semiconductors, polymers, minerals, art conservation and archeology, forensics, pharmaceuticals and the study of cell and tissues.

Semiconductors: Spectral maps of absorption sites in integrated circuits (ICs) with near infrared light reveal structures that have a different optical absorption than neighboring sites. A nonuniform absorption in a semiconductor structure located near an electrical overstress defect can be an important feature in failure analysis of ICs.[105] Although non-optical, another important spectral imaging modality is X-rays mapping. X-ray imaging capability is often integrated into scanning electron microscopes for characterizing the elemental make-ups of samples like semiconductors and ICs.[106-108] Specific X-ray wavelengths or energies are selected and measured, either by wavelength dispersive X-ray spectroscopy (WDS) or energy dispersive X-ray spectroscopy (EDS). EDS generates a spatially resolved distribution of electron energy emission data, where each element on the periodic table has characteristic x-ray emission spectrum.

Polymers: Light-emitting diodes (LEDs) based on conjugated polymers have potential use in applications such as flexible displays. Spectral imaging has been used for electroluminescence (EL) characterization of a polymer blend-based LEDs to elucidate

the relationship between the morphologies of the blend polymers and EL emission properties on a microscopic scale.[109] Bio-degradable implant material poly-L-lactic acid (PLLA), have also been studied with HSI. For example, Raman HSI is used by other researchers in my lab to identify crystalline and amorphous domains in the polymer scaffolds which affect their biodegradation properties.[110]

Minerals: Lithologic and mineralogic logging of drill cores are used by the mining industries to help manage mining operations. Drill cores are often the first evidence of deep mineral deposits. Most of the time mineral identification methods are subjective and depend on the skills and experience of geologists and mineralogists which vary from person to person. To standardize and objectify these observations, HSI can be a very useful tool for mineral identification and mineral mapping process at mining sites.[111] Many minerals display unique spectral features in the infrared and Raman modalities.

Archeology and Art Conservation: Multispectral imaging and HSI are in increasing demand in the field of art conservation, art history and archaeology. Spectral imaging has mostly been applied to paintings and manuscripts. Applications of HSI in art conservation include the detection of damage and past interventions, In addition, HSI is useful for monitoring the degradation of varnish on paintings, recovering erased or overwritten scripts in old manuscripts, as well as for identifying pigments.[35]

Forensic and Crime Scene Investigations: The HSI enables investigators to analyze the chemical composition of small samples and trace constituents, and to simultaneously visualize their spatial distribution. In addition, HSI offers significant potential for the detection, visualization, identification and age estimation of forensic

traces.[43, 44] The rapid, non-destructive and non-contact features of HSI enhance its suitability as an analytical tool for forensic science.

Food Quality and Safety Control: The HSI has been employed to provide a user-friendly analytical tool for various applications in food quality and safety. For example, it is used to monitor quality and shelf life of grains and nuts[112], to estimate the sweetness and amino acid content of fresh soybeans[113], to evaluate the quality of mushroom by estimating the hunter L value[114] (commonly applied feature for mushroom quality grading), to detect the size, color and presence of defects in citrus fruits, and to correctly classify lemons and mandarins.[115, 116] A suite of HSI methods is also used to assess the quality and safety of meat, meat products and fish.[117-122]

Pharmaceuticals: In the drug industry, HSI enables mapping the distribution of an active pharmaceutical ingredient (API) in an excipient, where not only the potency of the API is of importance but also its content uniformity. Other parameters are also monitored. For example, the particle sizes, their distribution, and sometimes the layer thicknesses of the coating or other structural details may also be measured. Infrared hyperspectral imaging can be used to identify the contaminants on the surface of a tablet and can also provide information regarding dissolution problems.[123] More recent efforts have sought to replace IR methods at the bench with Raman scattering techniques which simplifies sample preparation. In fact, Raman can be used to monitor pharmaceutical tablets that are still wrapped in bubble packaging.[124, 125]

The process analytical technology (PAT) initiative emphasizes quality by design rather than testing the final product, which results in cost savings, uniform quality, and higher throughput manufacturing in pharmaceuticals.[20] The rapid analysis afforded by

HSI, and its non-destructive and non-invasive nature makes it an attractive process analytical tool for the pharmaceutical industry, for both process monitoring and quality control in the many stages of drug production.

Hyperspectral Machine Vision: Hyperspectral machine vision systems enable automated sorting by detecting very small differences in similarly colored materials that cannot be distinguished with conventional imaging technologies. Machine vision systems are widely used throughout all sectors of the manufacturing industry. Other types of applications are also benefiting from the enhanced discernment capabilities of real-time HSI. For example, the use of near-infrared HSI has been explored as a way to augment the decision-making process during surgeries for cancer removal. A suit of techniques are also being explored for use in unassisted robotic surgeries.[126-131]

1.1.3 Hyperspectral Imaging in the Biomedical Field

The HSI offers great potential for medical applications as a noninvasive diagnostic tool and for surgical guidance. The HSI is able to deliver nearly real-time images of biomarker information. The reflected, fluorescent, scattered and transmitted light from tissue captured by HSI carries quantitative diagnostic information about tissue pathology.[132] Retinal imaging spectroscopy can provide functional maps using chromophore spectra. Oxygen saturation maps show ischemic areas from diabetes and venous occlusions.[133] Oxygen saturation of hemoglobin also reveals two hallmarks of cancer, angiogenesis and hypermetabolism, which are used to distinguish between healthy and malignant tissue in cancer diagnoses.[134] The HSI has been applied to the diagnosis of hemorrhagic shock[135], the assessment of peripheral artery disease[136], early detection of dental caries[137], fast characterization of kidney stone types[138], detection of laryngeal disorders[139], and so on.

Surgical Guidance: During a surgery, HSI can help surgeon to visualize the tissue types, organs, and blood vessels, which are sometime easily obscured with the presence of blood. HSI offers the potential to aid and extend the surgeon's vision at the tissue, cellular and even molecular level, so that better judgements can be made. The HSI has already been explored in surgeries, such as intestinal surgery[140], abdominal surgery[141], and renal surgery.[142, 143]

Fluorescence: Significant advances in instrumentation and detector design, as well as growing number of new fluorophores has led to a dramatic increase in multi-color fluorescence microscopy which is a type of hyperspectral imaging. Recent advances in fluorophores include synthetic quantum dots and genetically encoded fluorescent proteins

that span the entire visible spectral region.[144] Hyperspectral imaging combined with linear unmixing is a highly useful technique that can be used to untangle overlapping florescence bands originating in cells and tissues labeled with multiple synthetic fluorophores. In addition, HSI is a very powerful tool to reduce or eliminate signal bleed and artifact in fluorescence microscopy when imaging multiply labeled specimens. By imaging many wavelengths within a fluorescence band, rather than just one wavelength near the band center, a higher signal-to-noise ratio is achieved for each fluorophore in the specimen. Wavelength bands that are representative of the spectral differences between the fluorophores are sometime useful for more rapidly identifying the target constituent in a specimen.

Raman: Raman microscopy has been gaining recognition in the biomedical field due to its ability to nondestructively measure the distribution of biochemical components within complex biological samples. Raman spectroscopy in combination with optical microscopy provides a label-free method to assess and image cellular processes, without the use of extrinsic fluorescent dyes. The sub-micrometer resolution of confocal Raman enables cellular organelles to be imaged at spatial resolution similar to conventional microscopy. Raman spectral imaging has also been employed to study intracellular delivery and degradation of polymeric nanoparticulate drug carrier systems.[145] The combined use of Raman and infrared imaging is being investigated as a complimentary diagnostic method to conventional histopathology with the hope it will provide molecular level understanding of cancers.[146]

1.2 Principle of Hyperspectral Imaging

Hyperspectral imaging is a technique that generates a spatial map of spectral variation. The essential hardware, acquisition control software, and data processing strategies can differ markedly among HSI instruments. Likewise, the type of information desired from the sample governs which type of spectroscopy is utilized. Regardless of its implementation, HSI produces a set of spectra in which each spectrum corresponds to an assigned location on or in the sample as illustrated in Figure 1.

To visualize changes in the sample across its spatial extents, data processing is performed on the hyperspectral data so that a pseudo-color image map or volume view of the sample can be rendered. Color differences in the rendered result correspond to meaningful variations in the spectral characteristics of the sample. Depending on the type of data processing performed, the numerical scores upon which this color contrast is based can be used to extract either qualitative or quantitative information, or both.

Acquisition of hyperspectral data can be achieved using various methods like point mapping, line scanning, widefield (global) HSI, spatial multiplexing and spectral multiplexing. Also, there has been significant interest in developing a non-scanning approach such as snapshot hyperspectral imaging in which a full three-dimensional hyperspectral data cube is recorded for each frame.[133, 147, 148]

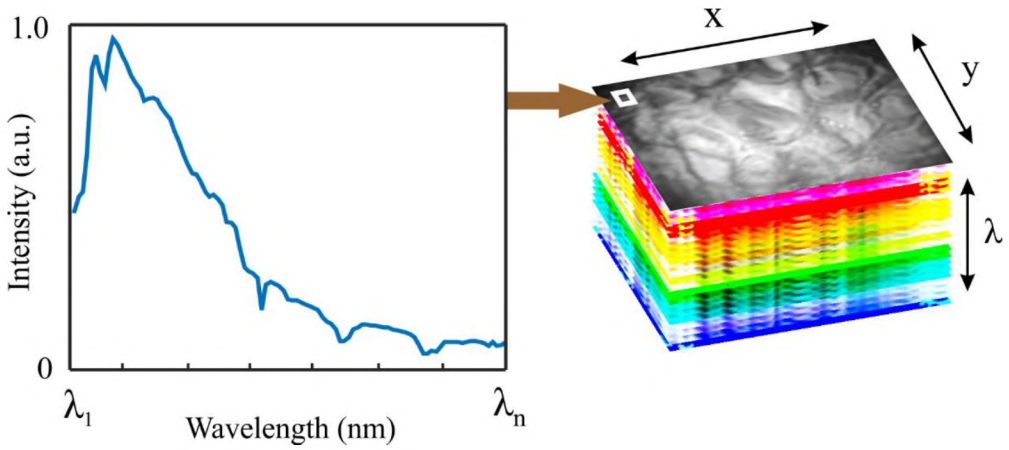

Figure 1: Illustration of Hyperspectral Data. On the right is a three-dimensional presentation of hyperspectral data cube where x and y are spatial dimensions of the sample (image plane) and the third dimension is the spectral dimension. Each pixel in the image plane can be plotted as a spectrum corresponding to that location on the sample (illustrated on the left).

In widefield hyperspectral imaging a whole frame containing the portion of the sample within the field of view is captured at a series of wavelengths. Wavelength selection is generally achieved by electro-optic tunable filters. Spatial scanning methods such as point mapping and line scanning has their own set of advantages and use scenarios. Point mapping is ideal for small samples in a benchtop setup where spectrum at each location on the sample is recorded. The sample stage or the acquisition assembly is moved in a raster pattern using a translation mechanism. Geospatial hyperspectral data is collected using line scanning where light in one dimension of the sample is dispersed via grating onto an imaging chip and the acquisition assembly is scanned across the other dimension of the sample via the motion of airborne spectral imagers.

Multiplexing can be performed via spatial multiplexing or spectral multiplexing. In the spatial multiplexing method whole field of view is illuminated, and a series of binary spatial mask are applied to the light coming from the sample. Spatial masking can be accomplished using a device like digital micromirror device (DMD), which consists of a two-dimensional array of many microscopic mirrors, these mirrors can be controlled individually to on or off position. Spectrum is collected for each mask and the resulting data is deconvoluted using Hadamard transform to reconstruct spectral and spatial information. Spatial multiplexing offers better signal to noise ratio in low signal-to-noise ratio applications.[110, 149]

1.3 Wavelength Selection

A necessary capability of HSI instruments is wavelength tuning. Early multispectral imagers often utilized a small number of fixed bandpass filters, mounted in a filter wheel, that could be individually introduced into the optical path of the imaging detector. The data, while limited in scope, was often sufficient to allow meaningful differences across the field of view to be revealed by performing simple calculations such as dividing the image acquired for one band by another. Global illumination of the sample, either by sunlight or the use of a diffuse source, simplified data acquisition by enabling concurrent capture of pixel locations across the widefield area in a single snapshot using detector arrays. For these experiments, the image resolution was determined by the magnification, the wavelength of light, and the pixel geometry and pixel density of the detector array. Many applications in remote sensing and microscopy, even today, use multispectral imaging. It remains an attractive alternative to HSI due to its high image resolution, small acquisition times, comparatively straightforward data analyses, ease of data visualization, and lower cost.

Even so, spectral imaging has advanced far beyond these early multispectral implementations and there are now many types of imaging approaches. For widefield HSI, electro-optic devices like the acousto-optic tunable filter (AOTF)[5, 150-155], Fabry-Perot tunable filter (FPTF)[7, 156-158], and liquid crystal tunable filter (LCTF)[6, 64, 159-162] are frequently used to provide wavelength selection. A number of specialized filters like the resonance ionization imaging detector (RIID)[9, 163], hybrid holographic-liquid crystal filters[164], and photonic crystals are also used.[11, 12, 67] In addition, wavelength multiplexing has been performed in widefield applications using step-scan interferometers and radio

frequency (RF) multiplexed AOTFs.[152, 165] Comparatively simple instruments that utilize a series of angle tuned fixed filters are also available.[166] Each of these approaches has been utilized for the widefield modality because they provide sufficiently high spatial resolution, are electronically tunable, and can be implemented in a way that imparts suitably small spatial aberrations.

Apart from the widefield modality, point-mapping and line scanning approaches that use optic fiber-coupled spectrographs equipped with sensitive multichannel detectors are also common.[167-170] An adaptation of line scanning, sometimes called pushbroom imaging, is useful in remote sensing applications in which the detector is moving relative to the target area. In scanning approaches, each frame of the array detector captures the wavelength-dispersed spectral information and the spatial map is built-up over time. To improve the signal-to-noise ratio in low-light applications, spatial multiplexing can be performed by introducing imaging optics and a spatial light modulator (SLM), such as a digital micromirror device (DMD), between the sample and the collection fiber. For binary encoding sequences in which each pixel either contributes fully or not at all to a measurement, Hadamard-based transformations are commonly used to recover the spectrum at each pixel in the image.[149, 171] The benefits of scanning and spatial multiplexing approaches include high spectral resolution and large spectral range.

1.4 Widefield Tunable Wavelength Filters

Among the traditionally used wavelength filtering devices the AOTF, LCTF, FPTF and angle tuned dielectric filters are commonly employed in various commercially available widefield hyperspectral imagers.

AOTFs are solid-state birefringent crystals that provide an electronically tunable passband in response to an applied acoustic field. A generalized schematic of the AOTF is shown in Figure 2A, a piezo-electric transducer is bonded to one face of a tellurium dioxide (TeO_2) crystal. Here, a change in birefringence as a function of incident angle is used to compensate for the momentum mismatch that occurs between the incident light and the applied acoustic wave across a large input angle. The AOTF requires a variable radio frequency (RF) driver, making the system bulky overall and hard to miniaturize. Because the angle of diffracted light in the AOTF changes according to the scanning wavelength, an image shift can result as a function of tuning wavelength. Image blur is also a challenging problem in AOTFs and occurs as a tradeoff between scene shift and image clarity. Improving one worsens the other.

LCTFs are tunable birefringent (Lyot) filters constructed from liquid crystal variable phase plates sandwiched between linear polarizers. There are main two ways to make a birefringent filter tunable. The first is to vary the physical thickness of the birefringent material in the optical path. This effectively changes the retardation of one polarized component relative to the other and can be accomplished using liquid crystal waveplates. The second approach makes use of a quarter-wave plate followed by a rotating half-wave plate in front of the exit polarizer. A device with an electronically tunable variable retarder (liquid crystal variable phase retarder) can be used as an

alternative to the rotating half-wave plate (Figure 2B). Nominal bandpasses of <2 nm can be achieved with LCTF but the overall peak transmission, out-of-band rejection and temperature stability of the filter are often poor.

The free spectral range of the angle tuned Fabry-Perot (FP) filter is limited by the occurrence of harmonic and overtone bands, the tuning of the passband is achieved by tilting the thin-film interference filter. Spectral transmission of most thin-film filters shifts toward shorter wavelengths when the angle of incidence increases from normal incidence to higher angles. However, the filtered spectrum becomes highly distorted at higher angles, and the shift can be significantly different for σ- polarized and π-polarized light, leading to a significant loss in performance and strong polarization dependence with limited free spectral range.

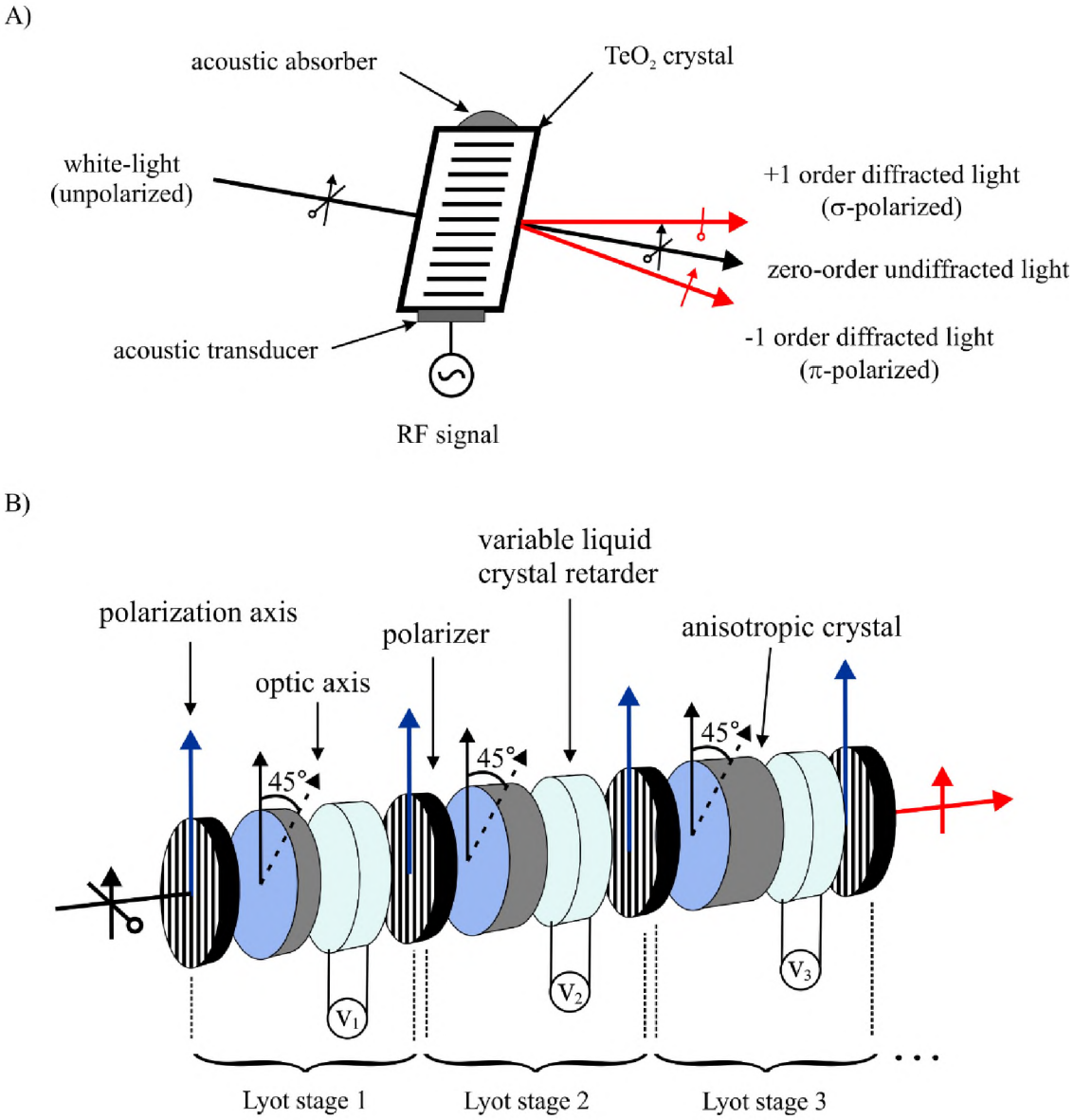

Figure 2. Schematics of the Acousto-Optic Tunable Filter (AOTF) and the Liquid Crystal Tunable Filter (LCTF): A) The AOTF is made up of an anisotropic material (TeO_2), which is bonded to a piezoelectric acoustic transducer driven by a radio frequency waveform synthesizer and an amplifier. B) The LCTF consists of a series of cascaded Lyot filters, each consisting of a birefringent element and liquid crystal waveplate sandwiched between polarizers. The number of Lyot stages depends on the desired bandpass and narrow passbands require more Lyot stages.

1.5 Summary of the Work Presented

The work presented here introduces a novel widefield tunable filter for visible and near infrared HSI based on surface plasmon coupling. The surface plasmon coupled tunable filter (SPCTF) is designed to leverage advances in consumer-based technologies so that HSI can be incorporated into compact handheld devices. As already discussed, there are many types of HSI implementations. The complexities associated with these approaches have slowed the use of HSI beyond basic materials research, bioresearch, remote sensing, industrial applications, and military applications. Until recently, the high cost of sensitive array detectors, light sources (lasers), high performance imaging optics, and the need for specialized computer hardware for acquisition and data processing impeded the spread of HSI to the consumer marketplace. In the last decade, the use of large imaging arrays in consumer products like smart cell phones, aerial drones, self-driving vehicles, and powerful portable computers has become ubiquitous. The necessary components for high resolution imaging, including data storage and on-board graphical displays, are embedded into these devices along with wireless networking and file transfer capabilities. In addition, bright optical sources like solid-state lasers and broadband LEDs (light emitting diodes) are commonplace, affordable, and already exist in many of these products. The last impediments to consumer-based HSI by non-specialists are turnkey software applications for automated data processing and the availability of compact, inexpensive, high performance, and low power wavelength selection devices.

The choice of which imaging strategy to use for compact, field-capable, HSI devices accounts for the capabilities and limitations of the potential modalities. Rapid

data acquisition, high image resolution, narrow spectral resolution, broad spurious-free spectral range, and high signal-to-noise level are desirable. Unfortunately, there exist tradeoffs among the number of pixels imaged, the number of optical bands interrogated, the desired signal-to-noise level, and the total acquisition time.[172] Although a full consideration is beyond the scope of this work, some generalizations are useful to consider. For example, as the number of wavelengths increases, the widefield acquisition time increases, but the time for the scanning methods remains unchanged. Conversely, as the number of pixel elements increases, there is no change in the duration of the widefield experiment, but longer acquisition times are needed for the scanning modalities. Data sparsity, a term used to describe that portion of the data that yields no relevant information, often leads to unnecessarily long acquisition times. For spatially complex samples, which are commonly studied using HSI, sparsity in the wavelength dimension is often greater than in the spatial dimensions, thereby making the widefield implementation more attractive. It is also important to consider the optical characteristics of the sample. For instance, longer exposure times are required to reach the desired signal-to-noise level in light-sensitive applications in which optical attenuation is applied to avoid sample damage. If a scanning modality is used in this circumstance, longer dwell times at each pixel location are needed and the overall acquisition time increases. Conversely, little or no attenuation of the light may be needed for the widefield approach if the same radiant source is used because the light will be defocused, thereby resulting in less optical power per pixel at the sample. Hence the disparity between the scanning and widefield acquisition times diminishes when the total number of scanned steps approaches the number of optical bands for these types of samples.

The SPCTF was designed to exploit existing and forthcoming technologies to achieve useful HSI capability. The large detector arrays and embedded circuitry of existing consumer products are most easily adapted for the widefield imaging modality in which no mechanized or tightly-regimented scanning protocols are needed. Software modification of existing platforms can readily provide image postprocessing to account for image registration errors that might result from detector or sample motion during the acquisition period. In fact, many consumer cameras already make use of image registration algorithms but do so to provide image stabilization during video recording or for reducing image blur in still pictures. Recent advances in computational imaging that enable post-acquisition refocusing of the image[173] will likely benefit widefield HSI approaches by allowing the user to retroactively confine the depth of field to within the sampled region so that off-sample regions in the image are ignored. Because the SPCTF preserves the trajectory of light rays in the Fourier space that lie within its acceptance angle, it can be easily integrated with computational imaging detectors.

As part of this work, a theoretical description of surface plasmon generation in thin metal films, and design and construction of the SPCTF are presented. Experimental reflectance data as a function of wavelength and incident angle with respect to the metal film, deposited on a glass prism in the Kretschmann-Raether configuration, is presented along with theoretical estimates for comparison. Also demonstrated is wavelength tuning using a coupled surface plasmon interaction in a symmetric cavity created by closely juxtaposing two prisms with their coated hypotenuses facing each other. Using this configuration as the basis of the SPCTF design, HSI using the SPCTF is demonstrated for the first time. The transmittance and bandpass values as a function of wavelength are also

reported. By exploiting the sensitivity of surface plasmon generation to the angle of incident light, a narrow passband SPCTF is introduced as a proof of principle. The bandpass and acceptance angle of the narrow passband device are given along with a brief discussion of the relationship between short-range and long-range surface plasmons in the SPCTF.

CHAPTER 2

THEORY OF THE SURFACE PLASMONS

Plasma oscillations are cooperative oscillations of free electrons such as those that can be induced in metals. The quasi-particle representation of the collective oscillation frequency is called a plasmon. Surface plasmons are said to exist when the oscillations are mostly localized at the surface, usually at the interface of a thin metal film with a dielectric. Other types of interfaces, such as those that form at dielectric-dielectric and dielectric-semiconductor boundaries can also support surface plasmons. The plasma waves are confined to the interface and exist as transverse magnetic (TM) waves that travel along the interface. At planar interfaces, the combined effect of the electron motion with the electromagnetic (EM) fields it creates in and around the metal (Figure 3) are referred to as a surface plasmon polariton (SPP).[174, 175]

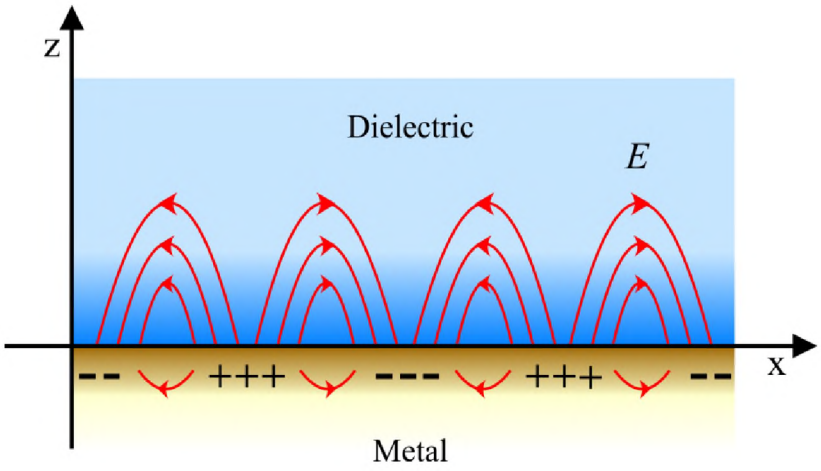

Figure 3. Surface Plasmon Polaritons (SPPs): SPPs are electromagnetic waves that travel along a metal–dielectric interface. The wave involves both charge motion in the metal surface and evanescent electromagnetic waves in the bulk dielectric.

While a full description of SPP generation is given by electromagnetic field theory, a classical treatment is useful for describing those aspects that involve reflection, transmission, and absorption of optical energy.[176, 177]

2.1 Optical Excitation of Surface Plasmon Polaritons

In optical refraction, which is described by Snell's Law and the Fresnel equations, the refractive index, $n = c_o/c_m$, is used to relate the velocity of light, c_o, in a vacuum to the wave velocity in a refractive medium, c_m.[178] In non-optical substrates such as in metals, the behavior of electromagnetic radiation is described by Maxwell's equations (Appendix A) which depend on the electric permittivity, ε, and magnetic permeability, μ. Because of dispersion, the refractive index, permittivity, and permeability are frequency dependent. It is convenient to recast the permeability and permittivity values for a substrate relative to their vacuum values so that $\varepsilon_r(\omega) = \varepsilon(\omega)/\varepsilon_o$ and $\mu_r(\omega) = \mu(\omega)/\mu_o$, where ω is the angular frequency and ε_r and μ_r are the relative permittivity and relative permeability, respectively. Maxwell's equations are generalized expressions that apply to optical refraction as well. The relationship between the n, ε_r, and μ_r is given by $n = \sqrt{\varepsilon_r \mu_r}$. Because most refractive substrates are non-magnetic at optical frequencies where $\mu_r \approx 1$, the refractive index can be approximated by letting $\approx \sqrt{\varepsilon_r}$. In metals where damping occurs, the complex permittivity, $\bar{\varepsilon_r} = \varepsilon_r + i\varepsilon_r'$, is used where ε_r' is the imaginary part of the permittivity. Hence, there exists a complex refractive index, $\bar{\varepsilon_r}$, with real, n, and imaginary, κ, parts such that $\bar{\varepsilon_r} = n^2 = (n + i\kappa)^2$.

The interaction of metals with electromagnetic radiation is largely dictated by the free electrons of the conduction band in metals. Light incident on a metal film interacts with the free electrons in the film that move in a manner to compensate for the incident field gradients. This motion accounts for the reflection of light by highly conductive metals. The extent to which electrons compensate for the applied field oscillations can be understood by considering the plasma frequency of the metal. When electrons are displaced by a small amount from their ions, a Coulombic restoring force results. The plasma frequency, ω_p, of a metal is the natural frequency at which the electrons collectively oscillate upon removal of the applied field. The magnitude of the Coulomb force governs the value of ω_p. At low field frequencies, the electrons can move in way that prevents the electric field from entering the metal. When the applied frequency exceeds ω_p, the field oscillations are too fast for the electrons to follow. Consequently, the metal can no longer reflect the light and the field propagates into the metal.

The momentum of optical photons at a given frequency is much smaller that the momentum associated with electron oscillations in most metals at the same frequency. This momentum mismatch makes it impossible to directly excite SPPs on a metal surface using light traveling in air. By exploiting the geometric arrangement between the incident ray and the metal surface in an optically refractive material, and by relying on damping in the metal, plasmonic motion can be induced on a metal surface by the incident ray. Two common geometric arrangements, the Kretschmann-Raether and Otto configurations, enable coupling of SPPs to incident photons (Figure 4).[174, 179, 180] In both cases π-polarized light traveling in a right-angle prism is incident to the prism hypotenuse at an angle above the critical angle. In the Kretschmann-Raether configuration, which is used

here to construct the SPCTF, the hypotenuse surface is coated in a thin metal film (~48 nm Ag).

In the Otto geometry if a metallic substrate is placed in the vicinity of the prism so that the evanescent fields of the reflected light impinge onto the metal, and the incident angle is appropriate, SPPs can be excited along the metal surface. In Otto geometry the metal thickness can be much larger than the decay length of the surface-plasma field in the metal.

In the Kretschmann-Raether configuration, the metal film is deposited on top of a glass prism. The film is illuminated through the dielectric prism at an angle of incidence greater than the angle of total internal reflection. The wave vector of light is increased in the optically dense medium. At a certain angle of incidence θ, the in-plane component of the photon wave vector in the prism can coincide with the SPP wavevector on an air-metal surface. The result is photon-plasmon coupling and the formation of surface plasmon polaritons.

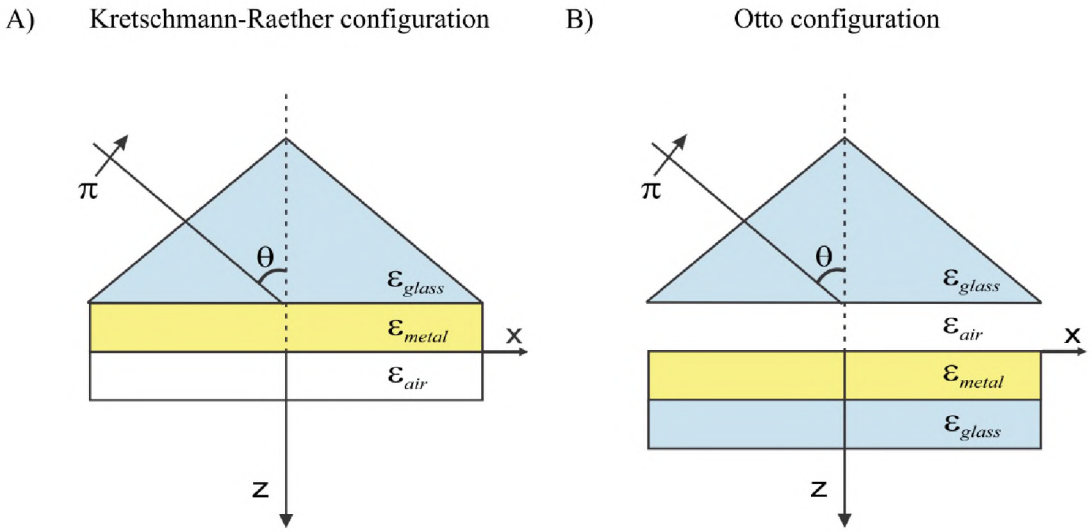

Figure 4. Optical Excitation of SPPs: A) Kretschmann-Raether configuration. B) Otto configuration. The electromagnetic field associated with incident π-polarized light is converted to electron density fluctuations (surface plasmons) at the metal-dielectric interface corresponding to the boundary between ε_{metal} and ε_{air}.

2.2 Dispersion Relation of Surface Plasmon Polaritons

For optical refraction in transparent materials, dispersion describes the change in refractive index as a function of the applied optical frequency. In the more complex case of a coupled interaction between photons and plasmons, dispersion can be thought of as the relationship between the applied optical frequency and the angular wavenumber, $k_x = 2\pi/\Lambda_x$. Here, Λ_x is the wavelength associated with the collective electron oscillation at the metal-dielectric interface. The wavevector, $\boldsymbol{k}_x$, lies within the plane of incidence along the metal-dielectric (air) interface. A plot of the dispersion curve as a function of angular wavenumber k_x along the metal film is shown in Figure 5.

In air, the angular frequency of light, ω_{air}, exceeds the plasmon frequency except where k_x approaches zero. In refractive materials such as glass, the slope of the light line changes by $1/n$, enabling the light line to intersect the dispersion curve for electron motion at a suitably large k_x value. For the ω and k_x values at the intersection, coupling between photons and SPPs is possible for π-polarized light. Even though the incident angle at the prism hypotenuse exceeds the critical angle, θ_c, the reflected intensity approaches zero at the angle of surface plasmon resonance, θ_{sp}, which is dependent on the wavelength of light (λ), metal film thickness, and the dielectric properties of the metal and glass. While the surface plasmon dip is broad as a function of wavelength, SPPs occurs over a narrow range of incident angles and a sharp minimum is observed in the reflectivity as a function of incident angle at the hypotenuse. As the film thickness increases, the efficiency of SPP coupling diminished due to the additional damping experienced by the electromagnetic fields during tunneling.

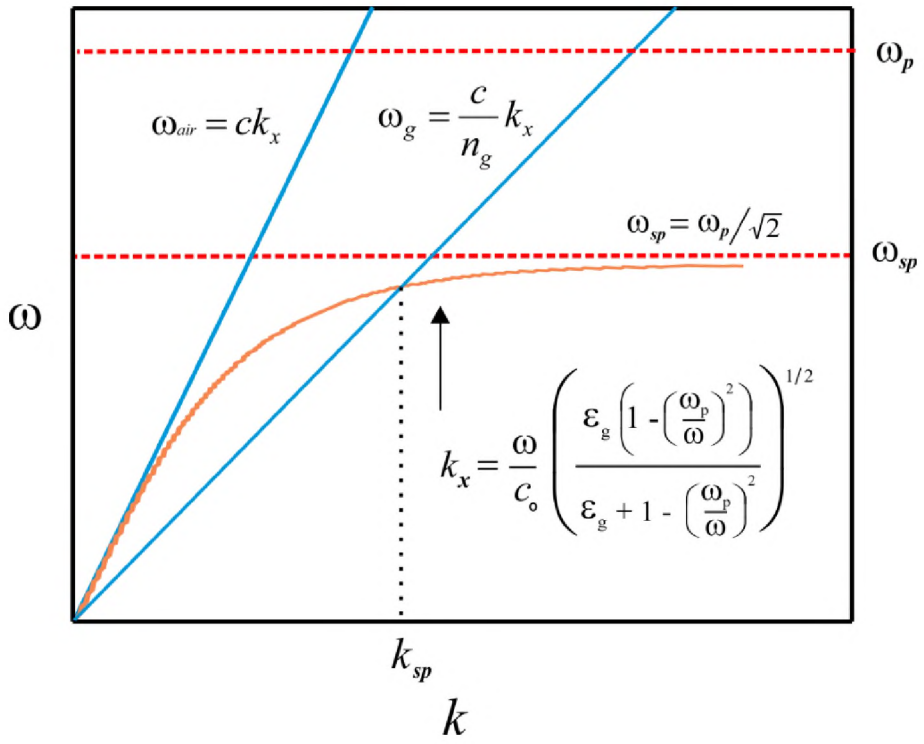

Figure 5. Dispersion Relation: In the Kretschmann-Raether configuration surface plasmons are generated at k_{sp} which corresponds to the point where the dispersion curve in the metal (orange) intersects with the light line in glass, ω_g. The light line in air, ω_{air} is shown for comparison.

2.3 Permittivity of Thin Metal Films

In metals, the permittivity has real and imaginary parts. The imaginary part is related to damping and determines the frequency bandwidth over which SPP generation is possible. In addition, damping limits the propagation distance of SPPs along the metal surface and is responsible for short-range surface plasmon polariton (SRSPPs). For efficient SPP generation, the real part of the permittivity should be negative and larger in absolute magnitude than that of the dielectric. Au and Ag meet these requirements and are relatively easy to deposit on glass as thin films. Because Au and Ag are dispersive, and because the SPCTF is designed to operate over a large spectral range, it is necessary to consider the change in permittivity as a function of wavelength.

A published table of permittivity values for Ag was used to estimate the real and imaginary permittivity values between 400 nm and 900 nm as shown in Figure 6A and 6B.[181] For gold a table of optical constants was used to obtain the refractive index values (*n)* and extinction coefficients (k) as a function of the photon energy in electron volts (eV).[182] Conversion of the energy, E, from eV to wavelength in nm was performed using 1239.8 eV·nm such that λ(nm) = 1239.8(eV·nm) /E (eV). From n and k, the complex permittivity is calculated as: $\bar{\varepsilon_r} = \varepsilon_r + i\varepsilon_r' = (n + ik)^2$, where ε_r and ε_r' are real and imaginary parts of complex dielectric constant $\bar{\varepsilon_r}$.

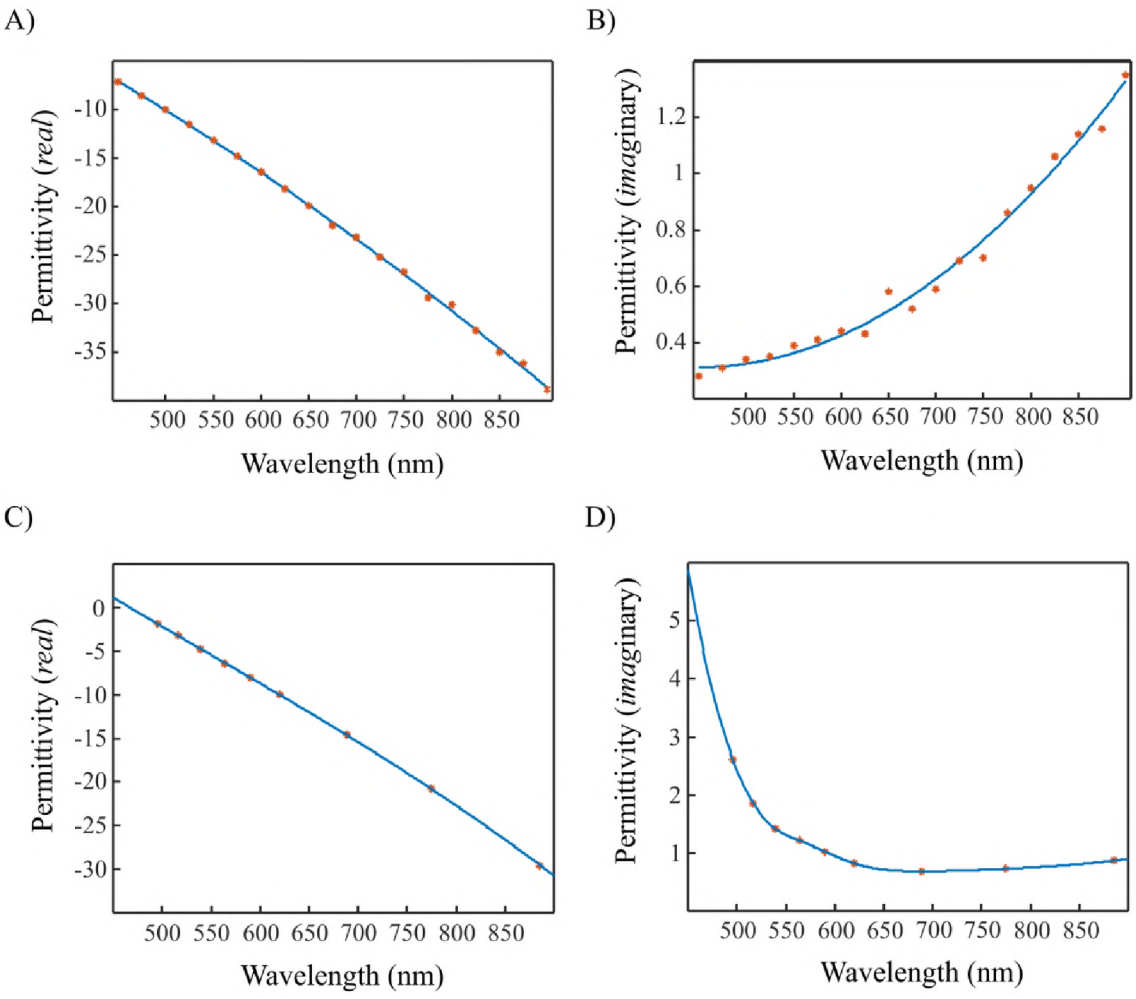

Figure 6: Complex Permittivity ($\overline{\varepsilon_r}$) of Ag and Au. A) The real (ε_r) and B) imaginary part (ε_r') of the relative permittivity as a function of wavelength for Ag. A second order polynomial (blue) was used to fit the data. C) and D) real (ε_r) and imaginary (ε_r') part of the complex permittivity of Au. A cubic spline (blue) was used to fit the data for interpolation.

Expanding the right-hand side of the complex permittivity equation yields $\varepsilon_r = n^2 - k^2$ and $\varepsilon_r' = 2nk$. The real part of the complex permittivity is an indication of dispersion in the material and the imaginary part is an indication of damping of the field. The real and imaginary parts of the permittivity for Au are shown in Figure 6C and 6D.

Permittivity is a measure of how an electric field affects, and is affected by, a medium. The permittivity of a medium describes how much electric field is generated per unit charge applied to that medium and it relates to a material's ability to resist an electric field. The complex permittivity curves for both Ag and Au show each having large negative real part of the permittivity, the meaning of negative permittivity is related to the non-resistance of the material to the electric field. The larger imaginary component of the complex permittivity of Au compare to Ag indicates that more energy loss resulting from damping of the electric field occurs in Au. For wavelengths shorter than ~550 nm, photons promote electrons of lower-lying bands into the conduction band in Au, thereby accounting for the large values for the ε_r'.[183] Hence Ag provides more efficient SPP coupling in the low wavelength portion of the visible region than Au.

2.4 Theoretical Calculation of Reflectance Loss by Photon-Polariton Coupling

For a metal-coated prism in the Kretschmann-Raether configuration, the reflectance of light at the glass-metal interface will be attenuated by the generation of SPPs at the metal-air interface. Given the permittivities of the glass and metal film, Fresnel's equations can be used to calculate the reflectance at specified angle of incidence. A drop in the reflectance at angles greater than the critical angle are attributed to the conversion of photon energy to surface plasmons. A summary of the equations that result from the Fresnel approach are included here. The variable assignments are described in Figure 7 for the Kretschmann-Raether configuration employed in the construction of the SPCTF. The Fresnel expressions enable the calculation of the reflectance for the glass-metal and metal-air interfaces which are needed for elucidating the SPP conditions. The reflectance, R, is calculated from

$$R = |r_{ij}|^2 \ , \tag{1}$$

where r_{ij} is the reflection coefficient at the interface between the i^{th} and j^{th} substrates. For the glass-metal interface,

$$r_{gm} = \frac{\varepsilon_m k_{z_g} + \varepsilon_g k_{z_m}}{\varepsilon_m k_{z_g} - \varepsilon_g k_{z_m}} \ . \tag{2}$$

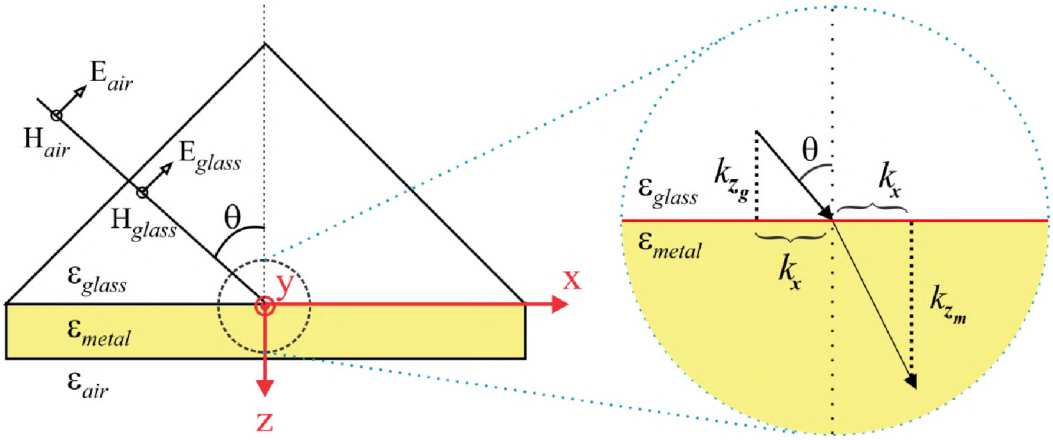

Figure 7: Variable Assignments of the Kretschmann-Raether Configuration for Use in the Fresnel Calculation of Reflectance. Because the permittivity of air is close to the vacuum permittivity, $E_{air} \approx E_0$ and $\varepsilon_{air} \approx \varepsilon_0$.

The magnitudes of the wavevector components along the z-axis are given by k_{z_g} in the glass and k_{z_m} in the metal, where

$$k_{z_g} = \sqrt{\varepsilon_g {k_0}^2 - {k_x}^2} \ , \tag{3}$$

and

$$k_{z_m} = \sqrt{\varepsilon_m {k_0}^2 - {k_x}^2} \ . \tag{4}$$

The magnitude of k_0 can be calculated from the vacuum wavelength, λ_0, according to $k_0 = 2\pi/\lambda_0$ and k_x, where

$$k_x = \eta_g k_o \sin\theta \ . \tag{5}$$

Because k_x is situated along the glass-metal interface and electromagnetic fields are continuous across the interface, k_x is a boundary condition and has the same value for the glass and metal. This process is repeated for the metal-air interface in which the reflection coefficient is calculated from

$$r_{ma} = \frac{\varepsilon_a k_{z_m} + \varepsilon_m k_{z_a}}{\varepsilon_a k_{z_m} - \varepsilon_m k_{z_a}} \ , \tag{6}$$

where the permittivities, ε_a and ε_m, and z-axis components of the wavevectors in the metal, k_{z_m} (Eq. 4), and air, k_{z_a}, are used. Although not shown in Figure 7, the assignment of k_{z_a} is consistent with that for glass and metal, and its value can be calculated from

$$k_{z_a} = \sqrt{\varepsilon_a {k_o}^2 - {k_x}^2} \ . \tag{7}$$

For the multilayer glass-metal-air system, the complex amplitude of the π-polarized reflected light can be determined from Maxwell's equations by applying the condition of continuity to both interfaces. Upon simplification, the combined reflection coefficient, r_{gma} becomes

$$r_{gma} = \frac{r_{gm} + r_{ma} e^{i2dk_{z_m}}}{1 + r_{gm} r_{ma} e^{i2dk_{z_m}}} \tag{8}$$

and is dependent on the thickness, d, of the metal film.[176, 177] The total reflectance of the glass-metal-air system can now be determined using the relation given in Eq. 1 so that

$$R = |r_{gma}|^2 = \left| \frac{r_{gm} + r_{ma} e^{i2dk_{z_m}}}{1 + r_{gm} r_{ma} e^{i2dk_{z_m}}} \right|^2 . \tag{9}$$

Figure 8 is the plot of calculated reflectance (Eq. 9) as a function of incident angle onto the hypotenuse of a BK7 prism coated with a 48 nm Ag thin film. A minimum in the plot of reflectance as a function of incident angle θ, represents the conversion of energy away from the reflected beam. When $\theta \geq \theta_c$, the energy loss is not accounted for in either the reflected or transmitted beams. Instead, the energy excites SPPs at the metal-air interface.

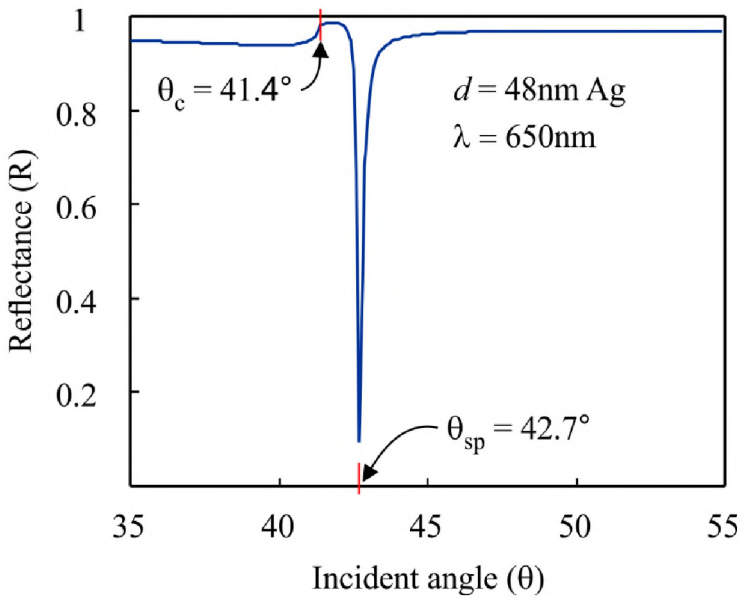

Figure 8. Plot of Calculated Reflectance as a Function of Incident Angle. Reflectance is calculated for 650 nm light from glass-metal interface of 48 nm Ag film using eq. 9. Minimum in the reflectance occurs at 42.7 degree (θ_{sp}) corresponds to coupling of SPPs to incident photons.

CHAPTER 3

DETERMINATION OF REFLECTANCE AS A FUNCTION OF INCIDENT ANGLE AND WAVELENGTH

Before proceeding with the construction and characterization of the SPCTF it was important to study the surface plasmon coupling in Kretschmann-Raether configuration. This chapter includes the process of preparing a prism with a thin Ag film followed by characterization of the film, a description of a custom-built apparatus designed to measure the reflectance for the Ag film in the Kretschmann-Raether configuration as a function of incident angle and wavelength, the calculated reflectance for the thin film coated on the hypotenuse of the prism, and results of the reflectance measurements as a function of incident angle and wavelength for the spectral range between 550 nm and 850 nm.

3.1 Experimental and Methodology

3.1.1 Sputter Deposition of Ag on BK-7 Glass Prisms

Thin Ag films were deposited using a 5.1 cm diameter 13.56 MHz magnetron sputter gun on the hypotenuses of BK-7 right angle prisms (Edmund Optics, 15 mm) to a target thickness of 48 nm. A modified sample mount was used that enabled a pair of prisms to be coated along with a polished piece of silicon wafer without having to reopen the sputter chamber. The silicon substrates were used to experimentally validate film thickness using scanning electron microscopy (FEI, Inspect-F50), Figure 9A-B. Sputtering was carried out in Ar gas at ~8 mTorr pressure using an RF power of 60 W. The background pressure measured with the Ar purge turned off and the pump throttle valve set partially closed as it would be during deposition, was 2.2×10^{-5} torr. A pressure of $\sim1\times10^{-6}$ torr was achieved with the pump throttle valve open.[184, 185] The sputter time was determined from earlier calibration trials in which Ag was sputtered on polished silicon substrates for a range of deposition times under the same experimental conditions that were used for the prisms. In addition, a quartz microbalance was used to monitor progress. Once coated, the prisms and silicon substrate were removed and immediately placed in a sealed air tight vessel under Ar purge. Electron micrographs were acquired along the interface of a cross section of the silicon substrate to measure the thicknesses across. Number of Ag film thickness measurements were recorded, and normal distribution was applied to those measurements to verify the final Ag film thickness. The thickness distribution plot is shown in Figure 9C.

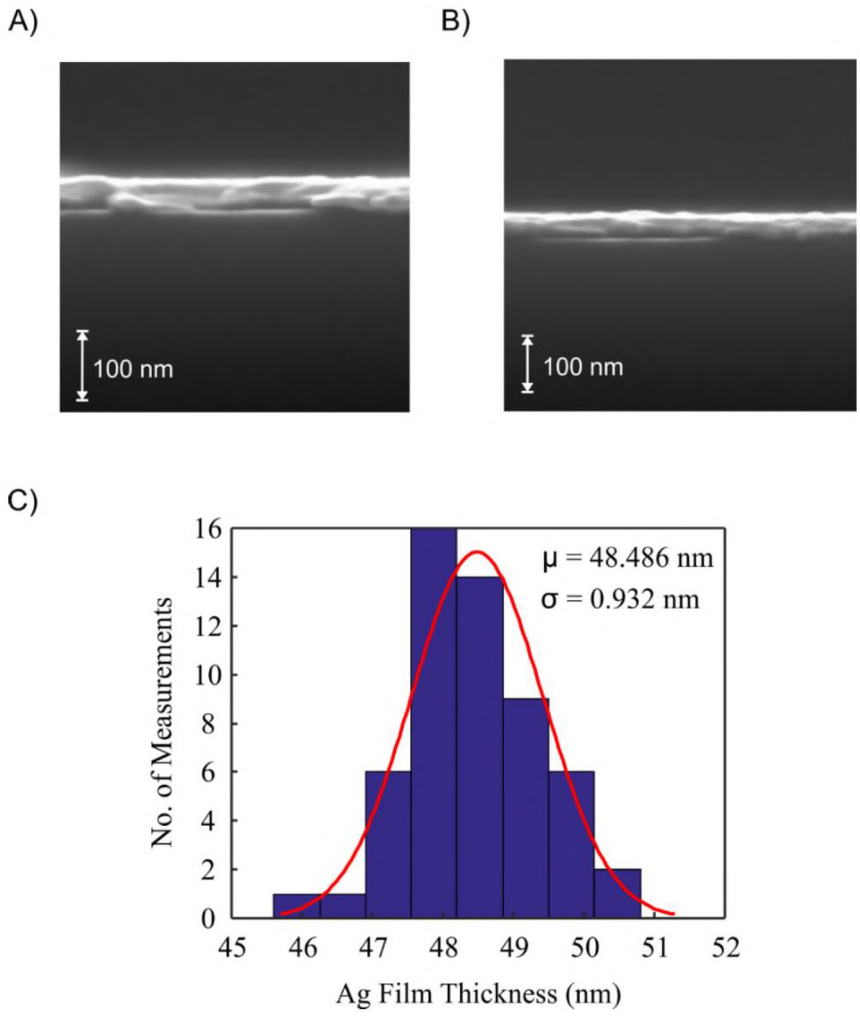

Figure 9: Scanning Electron Micrographs of Ag Film and Thickness Distribution. Electron micrographs A) and B) were obtained at 10 kV for different magnification, of the Ag film deposited on to silicon wafer under same condition and duration as the prism. Several thickness measurements were made across the silicon wafer. C) Normal distribution plot of the Ag film thickness measurements made on the silicon substrate. Average thickness of the Ag film is 48.486 nm.

3.1.2 Apparatus for the Reflectance Measurements as a Function of Incident Angle and Wavelength

To determine the angle of incident illumination necessary for SPP formation, the coated prism was placed on the central stage of a pair of rotational stages that shared a common axis of rotation as shown in Figure 10. Independent rotation of each motorized stage (Cognisys, ROTO_TAB_01) was provided by a USB connected controller (Cognisys, STKS-C-3X) to achieve a step accuracy of 0.01^{o}. A 150 W quartz tungsten halogen (QTH) lamp (GELCO FDS/DZE 24V) coupled to a 3mm diameter liquid light guide (Thorlabs, 2000 Series) was used to provided broadband illumination. Light exiting the light guide was collimated using an f/2 lens and then wavelength filtered to the desired range between 550 nm and 850 nm using a 550 nm long-pass filter followed by an 850 nm short-pass filter (Edmund Optics). Further collimation was achieved using series of 1 mm apertures placed before and after a linear polarizer (Thorlabs, GTH10MA) that was oriented to provide π-polarized light at the prism hypotenuse. A slit placed immediately before the prism was used to further reduce beam spread in the plane of incidence. A reference fiber was used to monitor the light source intensity changes over time. Light reflected from the prism hypotenuse was focused into a 200 μm collection fiber (CeramOptec) using an f/2 lens (Edmund Optics). The lens and collection fiber were mounted on a rail extending out from the center of the second rotational stage to enable angular positioning.

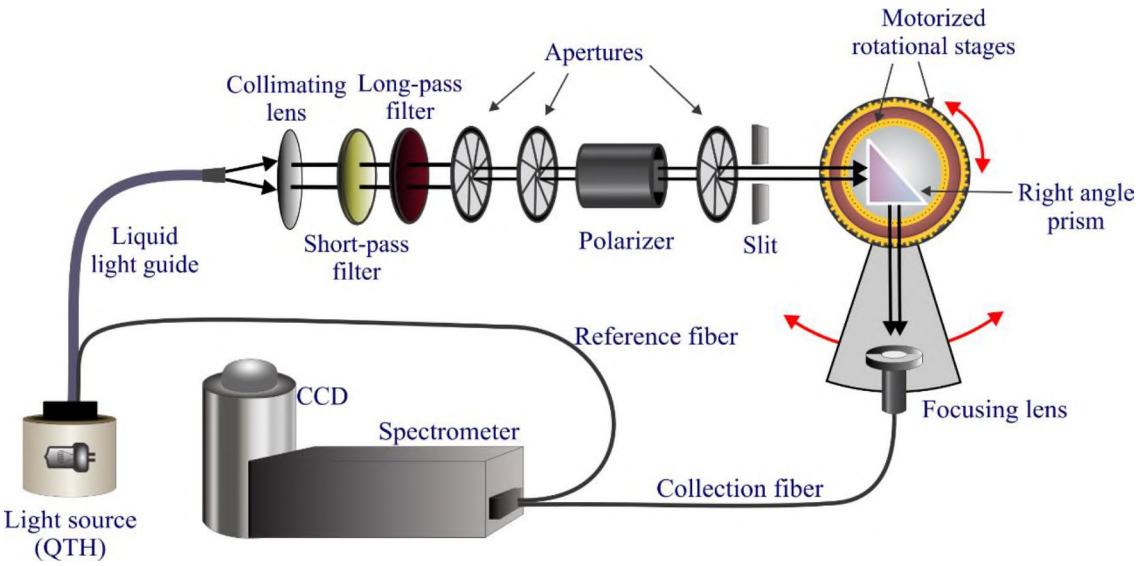

Figure 10: Schematic Diagram of the Optical Setup for Reflectance Measurements. Two independently controlled motorized rotational stages share the same axis of rotation. The Ag coated prism is mounted on top of the inner rotational stage and the collection optics are mounted on an extension rail attached to the outer rotational stage.

The distal end of the collection fiber was coupled to an imaging spectrograph (Chromex, 500IS/SM) equipped with a liquid nitrogen-cooled charge coupled device (CCD) detector (Roper/Princeton Instruments, EEV 400X1340B) for spectral acquisition. To ensure capture of the reflected light, a series of spectra were recorded for each 0.1^{o} increment of prism rotation by scanning the collection fiber by 0.05^{o} increments across the reflected beam. This approach also safeguarded against any mechanical play in the rotational stage assembly.

Data collection was automated using a Windows application written in Visual C++ that controlled the rotational stages as well as all aspects of CCD acquisition such as exposure time, chip-temperature (-90° C), and file handling. Wavelength calibration was performed using a spectrum acquired from a neon lamp (Newport, 6032). To enable calculation of the SPCTF reflectance a blank illumination spectrum was required. To accomplish this, the prism was removed and a spectrum of the illumination was recorded. A background spectrum, recorded by blocking the illumination, was subtracted from all spectra prior to taking the ratio of the reflected light spectra with respect to the illumination spectrum. Comparison of this data to theoretical estimates is performed by first adjusting the theoretical calculation to account for reflection losses at the entrance and exit faces of the BK-7 prism. All data processing was performed using code written in MATLAB (The MathWorks).

3.2 Result and Discussion

3.2.1 Calculated Reflectance from the Glass-Metal Interface in the Kretschmann-Raether Configuration

A theoretical description of the reflectance calculation from the glass-metal interface in the Kretschmann-Raether configuration is described in the section 2.4. Results from these calculations were obtained by original code written in MATLAB (Appendix B) and are shown in Figure 11. Figure 11A shows the calculated reflectance for 550 nm, 580 nm, 610 nm, 650 nm, 685 nm, 731 nm, and 794 nm light for incident angle between 38° and 48° onto prism hypotenuse (glass-metal interface). Since BK7 is a dispersive material, it is important to account for its dispersion because of each wavelength could potentially take a different path through the BK7 material. The light entering the prism will also undergo Fresnel reflection off of the entrance face of the prism and the same applies when the reflected light off of the hypotenuse leaves the prism exit face. The losses due to Fresnel reflections at the prism faces are calculated and subtracted from the theoretical reflectance of the glass metal interface to present the reflectance curve for each individual wavelength in a manner that is suitable for comparison with empirical data. The complex permittivity of a thin metal film is also a function of wavelength, as described in the section 2.3. Hence it is important to perform the reflectance calculation by factoring in dispersion with the complex permittivity of Ag. These theoretical calculations are performed for the wavelength range between 550 nm and 850 nm to match with the experimental conditions described in section 3.2.1. The theoretical reflectance surface is shown as a function of illumination wavelength and incident angle in Figure 11B.

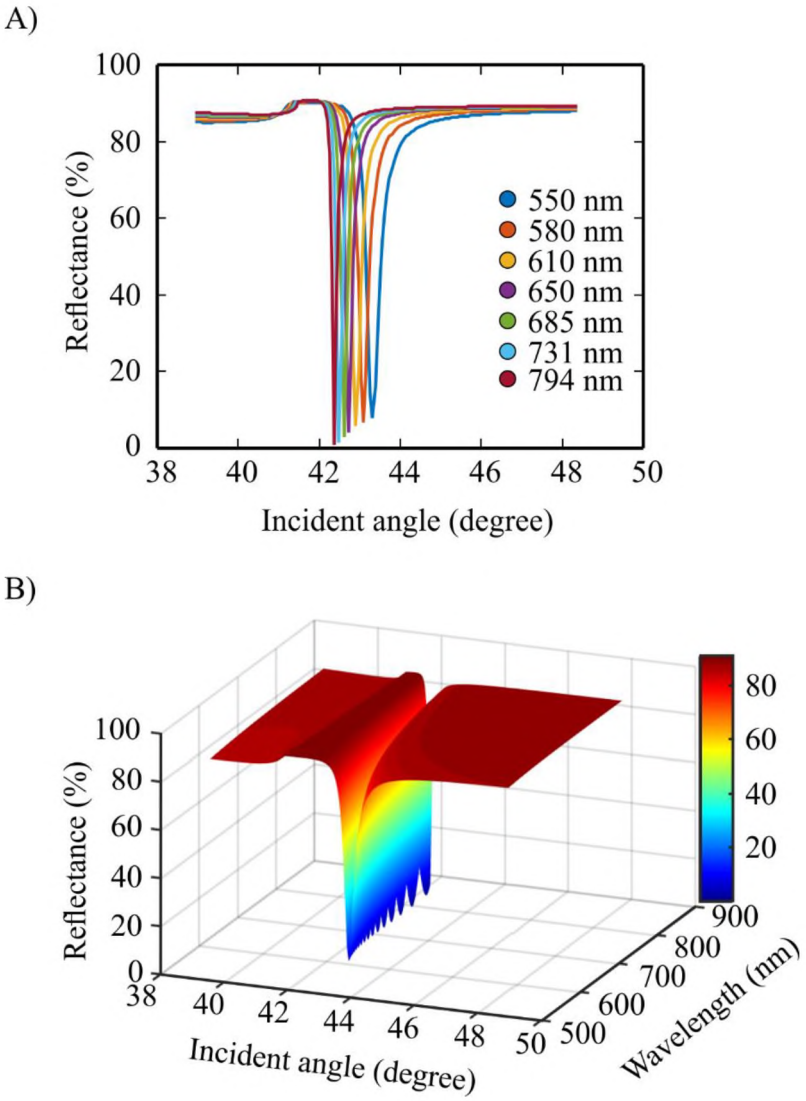

Figure 11. Theoretical Reflectance from the Glass-Metal Interface of a Prism Coated with Ag in the Kretschmann-Raether Configuration. A) Plot of reflectance vs incident angle calculated for various wavelengths. A sharp drop in the reflectance corresponds to the formation of SPPs at angles greater than the critical angle. B) The reflectance surface calculated for incident wavelengths between 550 nm and 850 nm and at incident angles between 38° and 48°.

There is an increase in the reflectance as the incident angle approaches the critical angle of ~42°. For larger incident angles in uncoated prisms, the reflectance is ~1. For a coated (Kretschmann-Raether) prism, there is a sharp dip in the reflectance between 43° and 44° that corresponds to SPP generation at the metal-air interface. As shown more clearly in Figure 11A, there is a wavelength dependence on the angle of maximal surface plasmon generation. The oscillatory appearance at the base of the plasmon dip in Figure 11B is an artifact arising from the finite increments for wavelength and incident angle that were used in the script to calculate the reflectance surface.

When the reflectance surface is viewed from top (Figure 12A) the angular dependence of SPP formation is apparent. Reflectance vs wavelength curves, extracted for various incident angles as shown in Figure 12B, shows that a broad range of wavelengths are able to couple at each discrete incident angle. Hence the coupling of SPPs is more strongly dependent on incident angle than the illumination wavelength.

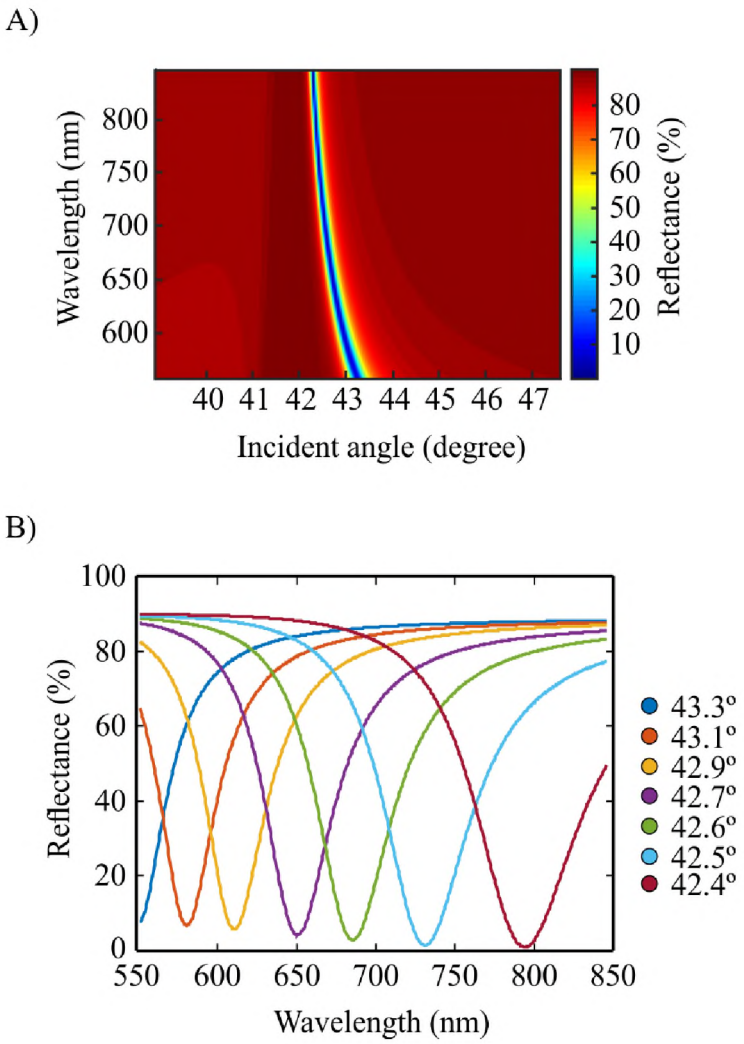

Figure 12: Incident Angle and Wavelength Dependence of Surface Plasmon Coupling. A) The calculated reflectance surface viewed as an image (top down view). The wavelength dependence of the incident angle necessary for plasmon formation is apparent. B) A series of reflectance curves extracted from the surface as a function of wavelength for various incident angles. For each incident angle a broad band of wavelengths are able to couple to SPPs.

3.2.2 Measured Reflectance from the Glass-Metal Interface in the Kretschmann-Raether Configuration

Using the experimental setup described in section 3.1.2, the reflected intensity from the glass-metal interface of a Ag coated prism was measured as function of wavelength and incident angle. For each 0.1° increment of the prism rotation, a series of 30 spectra were collected by scanning the collection fiber across the reflected beam at 0.05° increments. The surface plot in Figure 13A shows a set of 30 spectra collected for one incident angle on the prism, the intensity is the highest at the center collection position of the fiber and drops on either side as the fiber moves away from the angle of reflection. Figure 13B is the top-down view of the surface showing the reflected intensity as a function of wavelength and collection angle. Figure 13C is a plot of the 740 nm wavelength as a function of collection angle where the intensity is dropping away from the collection angle of zero. Each spectrum in a set is summed along its wavelength dimension, and the spectrum heaving greater summed value was used to calculate the reflectance. Figure 13D is the reflected intensities for the spectrum having highest sum. The profile of the illumination spectrum is apparent since the incident angle on prism is still below θ_{sp}, hence all the wavelengths are being reflected.

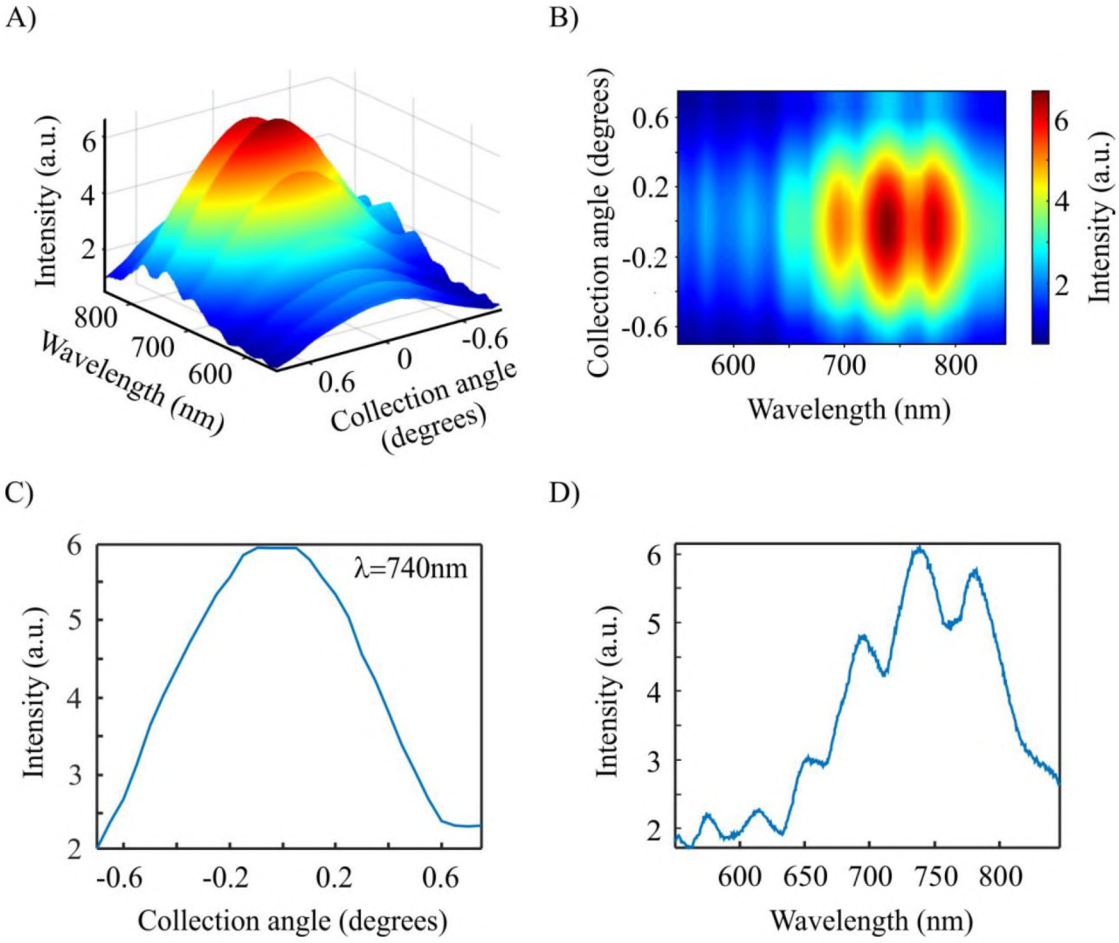

Figure 13: Preprocessing of the Reflected Intensity Measured from the Glass-Metal Interface of a Silver-Coated Prism. A) A set of 30 spectra collected for one incident angle by scanning the collection optic across the reflected beam is shown. B) The top-down view of the data showing the reflected intensity as a function of wavelength and collection angle to the angle of reflection is shown. C) The reflectance observed for 740 nm as a function of collection angle is plotted. The intensity is higher at the angle of reflectance and drops off on either side as the collection optic moves away from the reflected beam. D) Each spectrum in the set of 30 was summed along its wavelength dimension, spectrum with the highest is plotted, and used for the calculation of the reflectance. This process is repeated for all 200 sets collected for the whole range of incident angles onto the glass-metal interface.

A spectrum of the illumination source was collected after removing the prism. The background spectrum was recorded by blocking the incident beam and was subtracted from the reflected spectra and the illumination spectrum. The reflectance spectra were calculated as the ratio of the background corrected reflected light spectra with respect to the background corrected spectrum of the source. A plot of the reflectance as a function of incident angle and wavelength is shown in Figure 14.

The data results are shown in Figure 14 and are in qualitative agreement with the theoretical estimates (Figure 11 and 12) to within experimental error carried by the position uncertainty in the motions of the dual stages. For example, there is an increase in the reflected light as the incident angle approaches the expected critical angle of 42° and the angular position of the surface plasmon dip, in the vicinity of 43°, exhibits the expected wavelength dependency. Because the silver was not protected from oxidation during data acquisition, significant attenuation of the SPP is expected. Due to the large amount of data necessary to generate the reflectance surface, a short exposure time (1 s) was used to reduce the total acquisition time. While sufficient, the moderate signal-to-noise level is a consequence of the tradeoff between signal intensity and acquisition time. Traces from the reflectance surface for several angles of incidence and wavelength are shown in Figures 14C and 14D respectively. The surface plasmon dip is broad in the wavelength dimension and its full width half maximum nominally spans ~70 nm. Conversely, the formation of SPPs is very sensitive to the angle of incidence, spanning less than 2° over the wavelength range from 550 nm to 850 nm as shown in Figure 12D. This angular sensitivity can be exploited to reduce the optical bandpass of the SPCTF as shown in chapter 5.

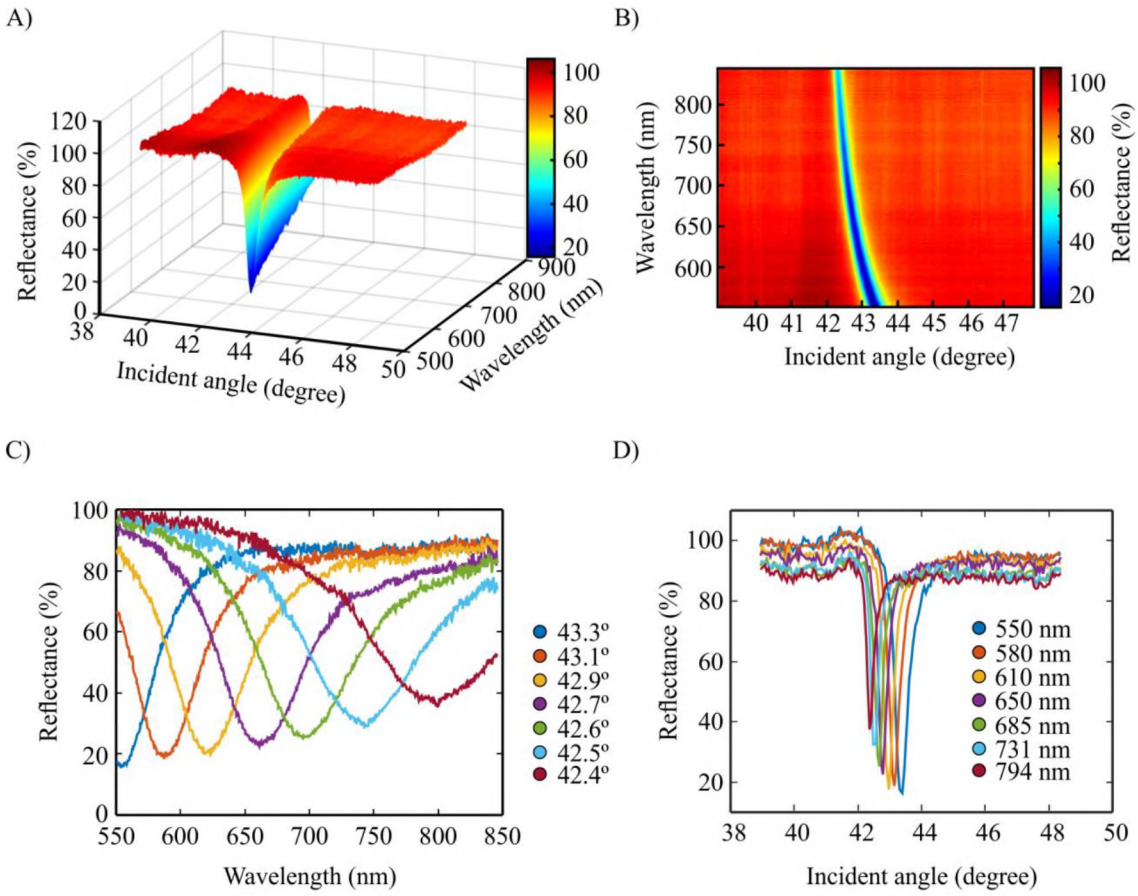

Figure 14: The Measured Reflected Intensity from the Glass-Metal Interface of a Silver-Coated Prism as function of Wavelength and Incident Angle. The reflectance surface and image, shown in A) and B) agree qualitatively with the theoretical estimates shown in Figure 11 and 12. Traces of the reflectance surface as a function of wavelength and incident angle are shown in C) and D). Although SPPs can couple over a large wavelength range, they are very dependent on the angle of illumination.

Optical characterization of metal-coated prism in the Kretschmann-Raether configuration is relatively straightforward as both the reflected and transmitted beams are readily accessible. Energy losses beyond those associated with non-ideal behavior of the substrates can be accounted for, to the extent that theory allows, by the formation of SPPs. While imperfect, there is substantial agreement between theory and empirical findings. The more challenging issues are related to understanding the SPP character, the behavior of electron groups as well as individual charges, and the way that surface non-uniformities in the metal and support substrate affect SPP formation and propagation.

CHAPTER 4

SURFACE PLASMON COUPLED TUNABLE FILTER

This chapter describes the coupled surface plasmon resonator along with the design of the surface plasmon coupled tunable filter (SPCTF). The SPCTF can be loosely thought of as a merging of the Kretschmann-Raether and Otto configurations. The SPCTF is constructed from two prisms, each constructed in Kretschmann-Raether configuration. The prisms are aligned to one another with their Ag-coated hypotenuses facing each other, yet separated by a thin dielectric (airgap). The electromagnetic fields at the metal-air interfaces arising from electron motion as well as any evanescent contribution from the incident and coupled light fields are acted upon by the conditions of the resonant cavity as a whole. Hence, the extent of coupling of SPPs across the airgap is strongly dependent on the cavity geometry and dielectric properties of each layer. In addition, the phase relationship between plasmon oscillations in each metal influences the

SPP coupling efficiency. The SPCTF exploits these properties to achieve wavelength tuning of the coupled light by varying the dielectric thickness (airgap thickness). For uncollimated monochromatic light, a range of incident angles is presented to the SPCTF and more than one coupling mode can be populated simultaneously, depending on the airgap distance.

An ideal tunable wavelength filter for hyperspectral imaging should demonstrate sufficient throughput, a suitable bandpass for the application, a large spurious-free spectral range, and diffraction limited spatial resolution. In this chapter, the SPCTF performance is characterized, wavelength tuning is explored as function of airgap thickness in the range between 550 nm and 850 nm, transmittance and its bandpass is measured as a function of tuning wavelength. The spatial resolution of the filter is measured, and hyperspectral imaging is demonstrated using a model sample.

4.1 Experimental and Methodology

4.1.1 Design of the Surface Plasmon Coupled Tunable Filter

The SPCTF described here is constructed from two prisms as described in Figure 15 that are closely juxtaposed with their metal-coated hypotenuses facing each other. In this arrangement, light incident on the first glass-metal interface can excite SPP at the metal-air interface. Due to the proximity of the second (identical) metal-coated prism, dipole-dipole coupling can drive SPP formation at the air-metal interface of the second metal-coated prism. Because both metal-coated prisms are identical, photon-plasmon coupling at the metal-air interface of the first prism can be expected to lead to plasmon-photon coupling at the air-metal interface of the second prism.

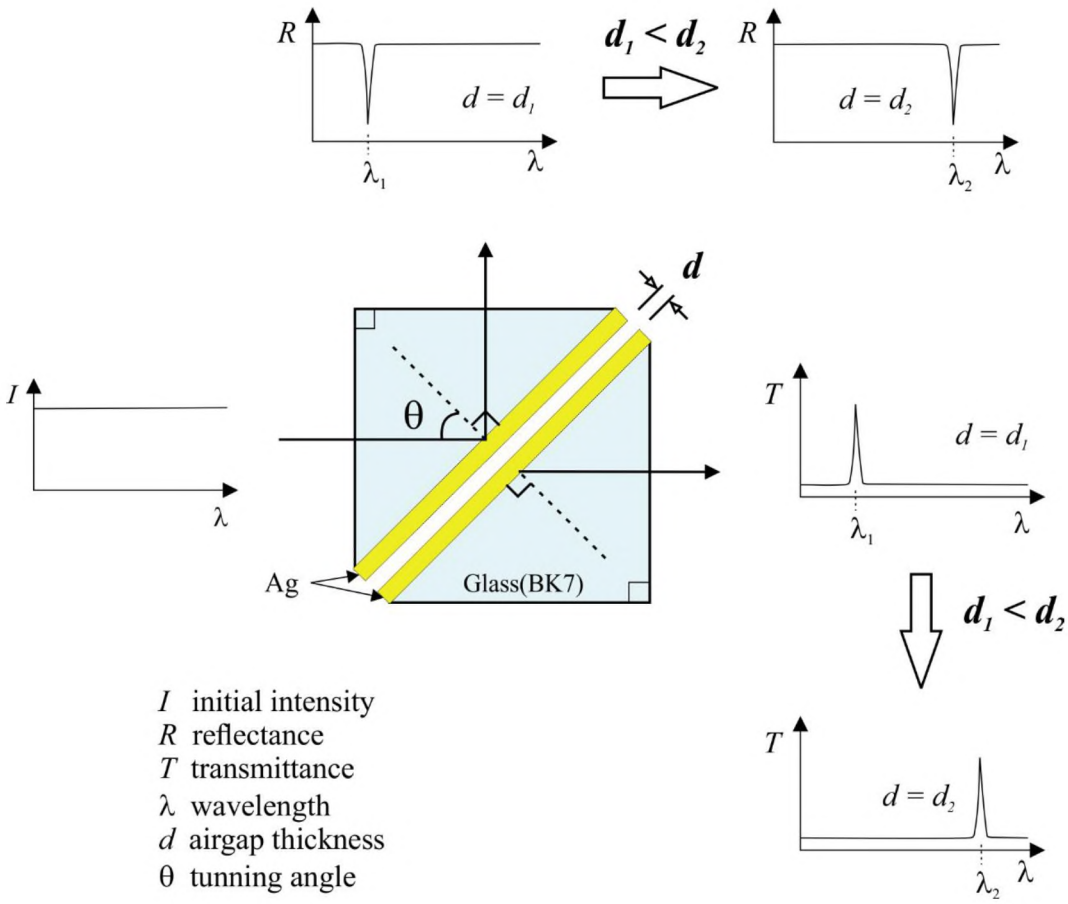

Figure 15: The Surface Plasmon Coupled Tunable Filter (SPCTF). Two metal coated prisms separated by a small tunable air-gap are used to provide wavelength tuning. Increasing the airgap from d_1 to d_2 causes the transmitted light to shift to a longer wavelength. The surface plasmon dip in the reflected light also shifts towards a longer wavelength.

As illustrated in the enlargement of Figure 7, the wavevector projection along the interface, k_x, is shared by both the incident and transmitted radiation such that $k_x = \eta_g k_o \sin\theta = 2\pi/\Lambda_x$, where η_g is the refractive index of the BK7, k_o is the wavevector in vacuum, θ is the incident angle and Λ_x is the wavelength related to SPPs. For coupling to occur, both frequency and momentum must be matched between the photon and plasmon. This occurs at an incident angle θ_{sp}, in the direction along k_x.

The incident angle required to reach the transmission maximum in the SPCTF is not the same as the incident angle at which SPP coupling is maximum for the case of the single Kretschmann-Raether prism, neither are these angles separated by a constant amount. In the single interface case, a minimum in the reflectance occurs when the component of the incident wavevector parallel to the interface, after undergoing modifications by the metal film, matches the real part of the surface SPP wavevector. The maximum in the surface charge density occurs when the normal electric field component peaks. The coupled dielectric system of the SPCTF behaves in the similar fashion, but must be considered as a whole.[186]

4.1.2 Construction and Characterization of the SPCTF

The SPCTF was constructed by affixing both prism to aluminum rods using 330 epoxy (Hughes Associates). The rods were inserted into the channels of a custom aluminum mounting that had openings to expose the optical surfaces of the SPCTF. One prism was held stationary while that other could be moved by turning a finely threaded screw, thereby adjusting the air gap between the prisms. Insertion of the prisms into the mounting was performed prior to curing of the epoxy so that the prisms could be brought into contact with each other as the epoxy set to establish a sufficiently parallel alignment between their hypotenuses. Once construction of the SPCTF mounting was complete, the assembly was positioned in place on the rotating stages, described in section 3.1.2 and the fiber collection optics were repositioned as shown in Figure 16. A series of spectra were collected for a range of SPCTF gap distances along with a spectrum of the illumination that was acquired by removing the SPCTF. A background spectrum, obtained by blocking the illumination path, was subtracted from all spectra prior to taking the ratio of the transmitted light spectra with respect to the illumination spectrum.

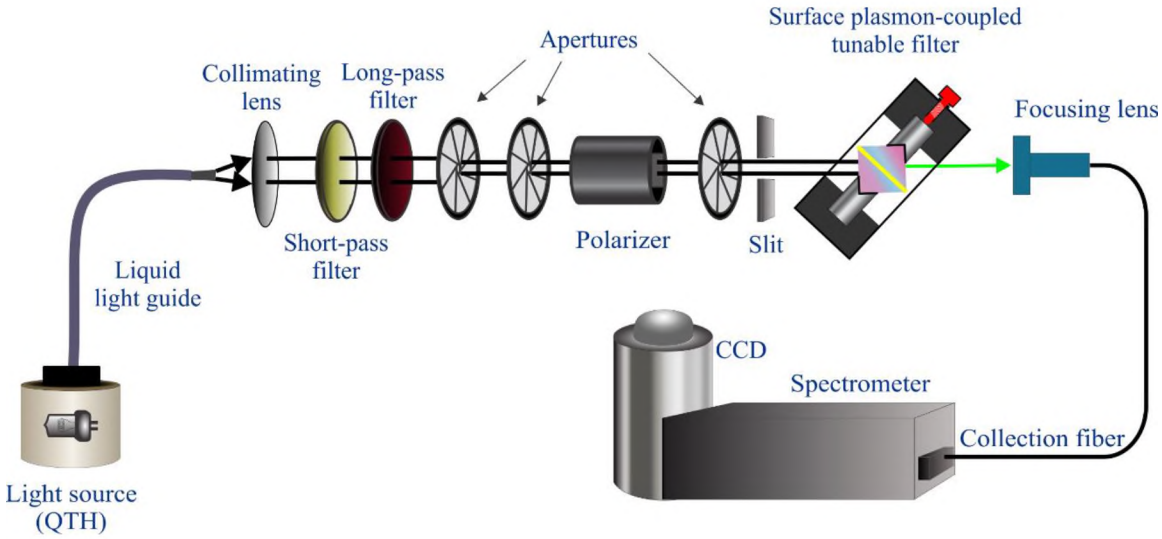

Figure 16: Apparatus for Measuring SPCTF Transmittance. Transmitted light through the SPCTF was measured for a series of airgap distances by carefully turning the micrometer screw. The transmittance and bandpass were calculated as a function of airgap distance and tuning wavelength.

4.1.3 SPCTF Hyperspectral Imaging Microscope

The schematic diagram in the Figure 17 is an illustration of the optical setup used to perform proof-of-principle SPCTF hyperspectral imaging for the first time. Illumination was performed in transmission mode using a broadband QTH light source coupled to a refractive microscope (Olympus, BX-60). The transmitted light from the sample was collected using an infinity corrected 10× objective (Olympus, 0.30 NA). To selected only the π-polarized component of the light a Glan-Thompson polarizer (Thorlabs, GTH10MA) was placed before the SPCTF. Wavelength filtering was achieved by adjusting the airgap of the SPCTF, a mirror placed after the SPCTF directed the light to a spectrometer via a fiber optic, to verify the tuning wavelength. The mirror is removed when imaging, image acquisition was performed using a liquid nitrogen-cooled CCD (Roper Scientific EEV1024x1024B) coupled to image reformation optics.

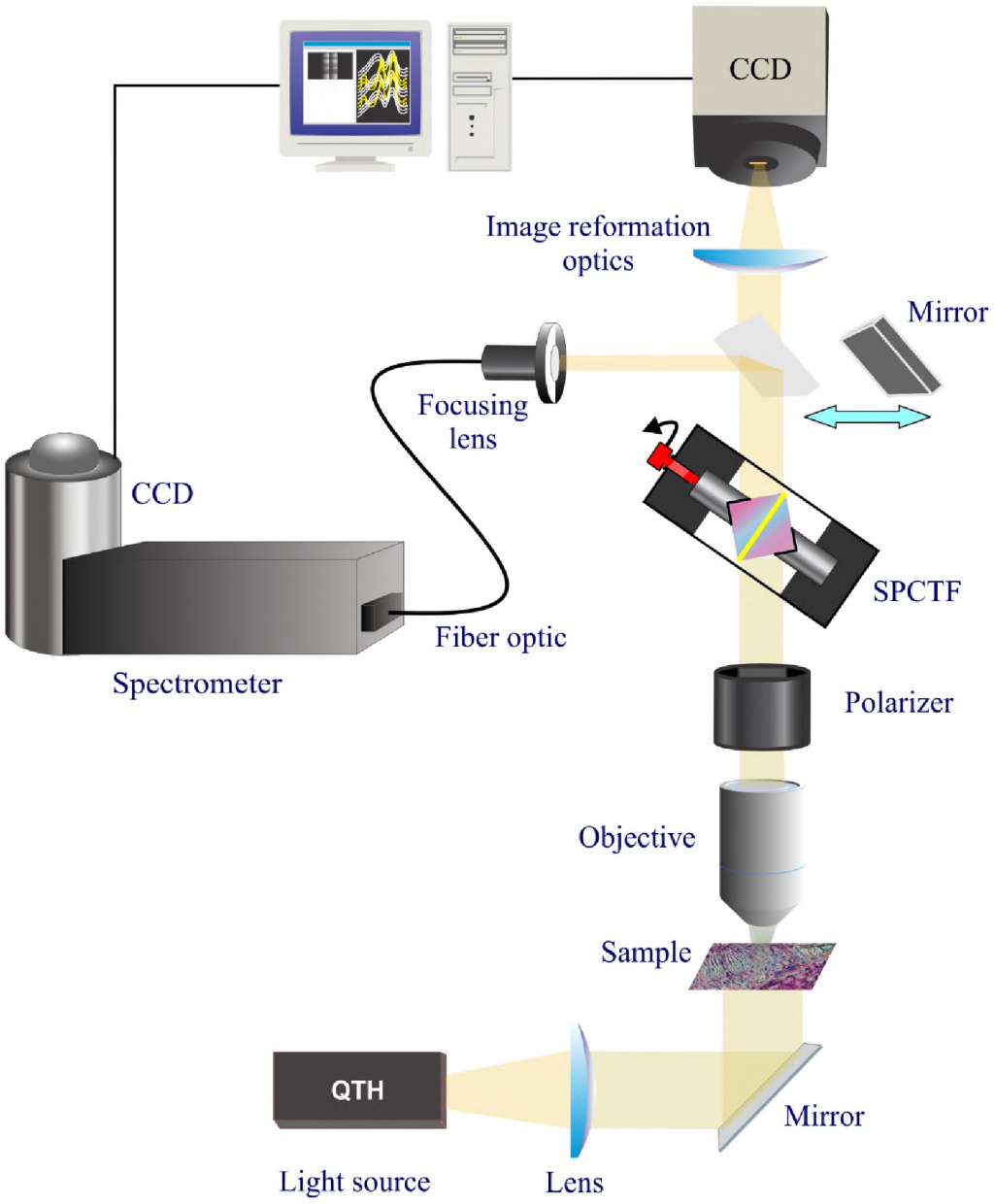

Figure 17: SPCTF Hyperspectral Imaging Microscopy. A mirror was placed in the path after the SPCTF to direct the light to the spectrometer to verify the tuning wavelength and removed while imaging.

4.1.3.1 Determination of Image Resolution

To measure the image resolution of the SPCTF microscope, a USAF 1951 resolution target was imaged in reflectance mode using a 10x objective. Illumination was provided by the QTH lamp of the microscope.

4.1.3.2 SPCTF Hyperspectral Imaging

Hyperspectral imaging is performed on a commercially prepared sample, a stained pine stem cross section (Carolina Biology Supply Co.) mounted in glass. Images of the sample were collected at 25 nm increments from 450 nm to 700 nm at the full pixel resolution of the CCD (1024x1024). The exposure time for each image was 1 s. Wavelength tuning was achieved by adjusting the airgap as described in section 4.1.2. Once collected, post-processing of the data to reveal image color-contrast based on spectral shape was performed in MATLAB using the spectral identity mapping algorithm.[187, 188]

4.1.4 Measuring SRSPPs and LRSPPs

Measurement of the short-range surface plasmon polaritons (SRSPPs) and long-range surface plasmon polaritons (LRSPPs) was performed using 650 nm light from a diode laser in place of the QTH source in the optical set-up described section 4.1.2. Spectra of the light transmitted by the SPCTF were collected over a ±6° range of incident angles. The process was repeated for the range of airgaps in which SRSPPs and LRSPPs could both be observed as well as for appreciably thick airgaps in which only the LRSPPs were observable.

4.2 Results and Discussion

4.2.1 SPCTF Transmittance and Bandpass

For a single metal-air interface, different wavelengths couple at different incident angles. Wavelength tuning in the SPCTF, however, is accomplished for a fixed incident angle by changing the air gap distance between the two metal-air interfaces that comprise its resonant cavity. A series of SPCTF transmittance spectra are shown in Figure 18A for a progression of airgap distances that increase for increasing passband wavelength. While the nominal airgaps are between 1 μm and 2 μm, the tuning was performed manually and precise estimates of the gap distances were not achievable using this experimental setup. The measured bandwidths are likely larger than would be predicted for ideal substrates due to surface roughness in the glass and metal. In addition, no feedback mechanism was in place to either monitor or actively control the degree of parallelism of the metal-air interface during tuning. Hence the observed SPCTF transmittance (25%-35%) and bandpass values (~70 nm, nominally) would likely improve by employing smaller and flatter substrates, and by replacing the mechanically-adjusted air gap with precision electro-optic tuning.

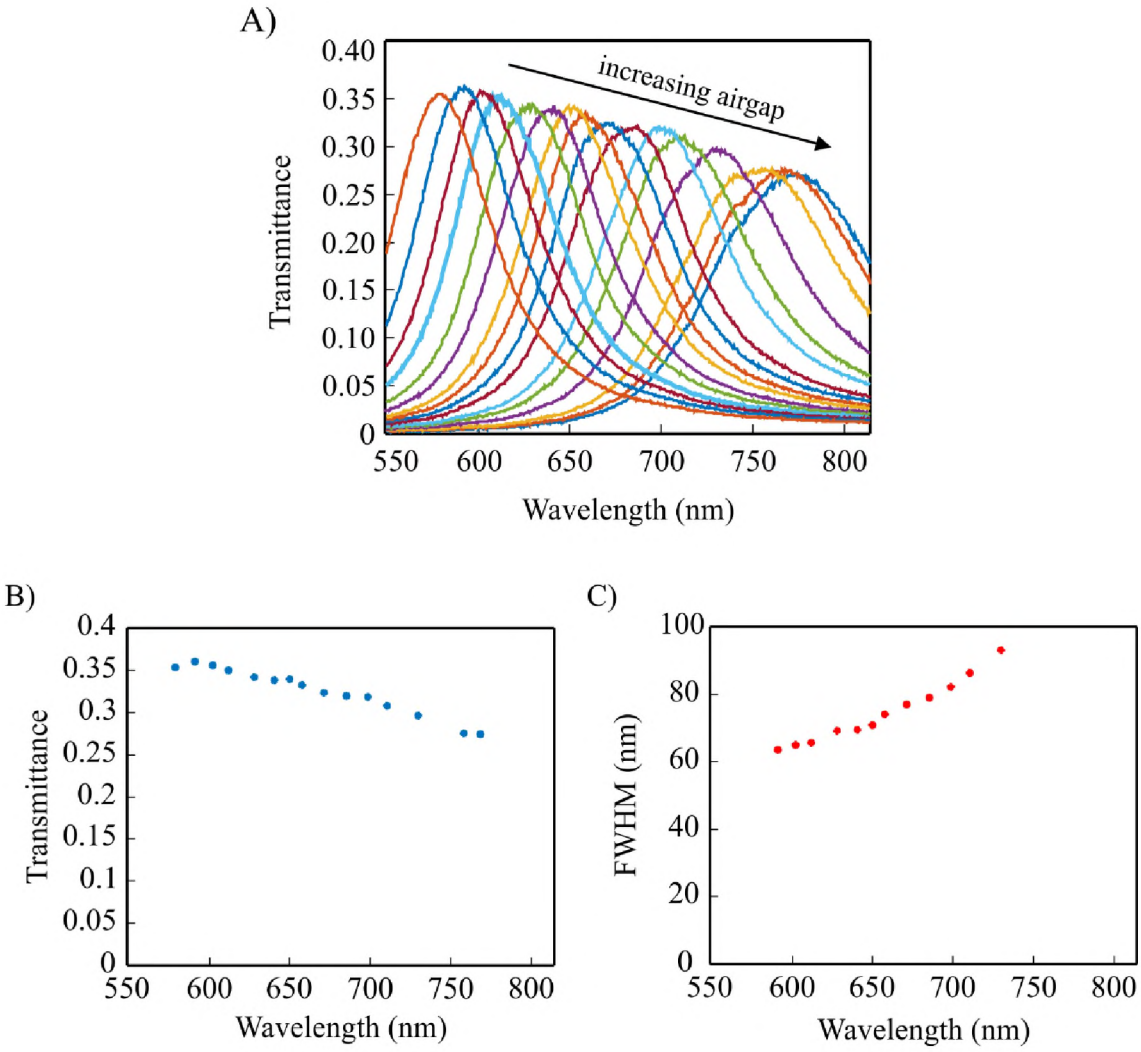

Figure 18: Wavelength Tuning of the SPCTF. A) Transmittance spectra are shown for a series of air gap distances. With increasing airgap distances, the passband shifts to longer wavelengths. B) The transmittance of the SPCTF and C) the SPCTF bandwidths (FWHM) are shown as a function of passband wavelength.

4.2.2 SPCTF Microscope Image Resolution

The light from an infinitesimally small source, a point-source, spreads out as it propagates according to its point spread function, which is dependent on the optical properties of the materials through which it propagates. Because light has wave character, its diffraction and scattering limits the achievable spatial resolution of an imaging system. The diffraction of light is wavelength dependent, so the resolution limit observed in the far field is also function of wavelength. Hence, the image of a point source appears as an Airy (blurry) disk with a diameter much larger than the source itself. Because the Airy disks of two neighboring point sources overlap, the image may not show two distinct sources of light. The minimal distance between the point sources that enables them to appear as sufficiently separated in the image is the resolution limit of the imaging system. The degree to which two overlapping Airy disks must be separated is a matter of some subjectivity. Fortunately, three well-recognized resolution criteria have been widely adopted; the Rayleigh, Abbe, and Sparrow criteria have been formulated into mathematical estimates of the resolution limit. These closely related concepts mainly differ in the degree of Airy disk separation required to assert that the point sources are resolvable. The Rayleigh, Abbe, and Sparrow formulations are given by

$$r_{Rayleigh} = \frac{0.61\lambda}{n\,sin\theta}\ , \tag{10A}$$

$$r_{Abbe} = \frac{0.5\lambda}{n\,sin\theta}\ , \text{ and} \tag{10B}$$

$$r_{Sparrow} = \frac{0.47\lambda}{n\,sin\theta}\ , \tag{10C}$$

where r is the distance between the two objects (point sources), λ is the wavelength of light, and n is the index of refraction of the medium between the sample and collection optic (objective lens). It should be noted that each denominator, $n \sin\theta$, is just the numerical aperture (NA) of the collection optic. From the numerators, it is clear that the Rayleigh criteria requires the most separation between the point sources while the Sparrow criteria requires the least.

An image of the USAF 1951 resolution target acquired through the SPCTF tuned at 700 nm passband is shown in Figure 19. The smallest element of the target has 228 line-pairs/mm. Hence each line pair, consisting of one bright and one dark line, is ~4.4 μm across. For 700 nm light in air, using a 0.30NA objective, the resolution limits are $r_{Rayleigh} \approx 1.4$ μm, $r_{Abbe} \approx 1.2$ μm, and $r_{Sparrow} \approx 1.1$ μm. Based on the line profile of intensity values across element #6 of group #7 (Figure 19), the SPCTF microscope can resolve features smaller than 4.4 μm. This is evident because the degree of separation between adjacent bright lines, each appearing 4.4 μm apart, is greater than that required for any of these resolution criteria. The image performance in this case is limited by the pixel coarseness of the CCD detector. By fitting Gaussian profiles to the bright lines of the resolution target and adjusting their overlap to that of the Rayleigh criteria, an estimate of the effective image resolution that takes into account both the diffraction limit and the CCD pixel geometry is obtainable. The effective Rayleigh resolution is ~ 3.5 μm. Hence, while the optical performance of the SPCTF may be diffraction limited, the microscope as a whole approaches the diffraction limit.

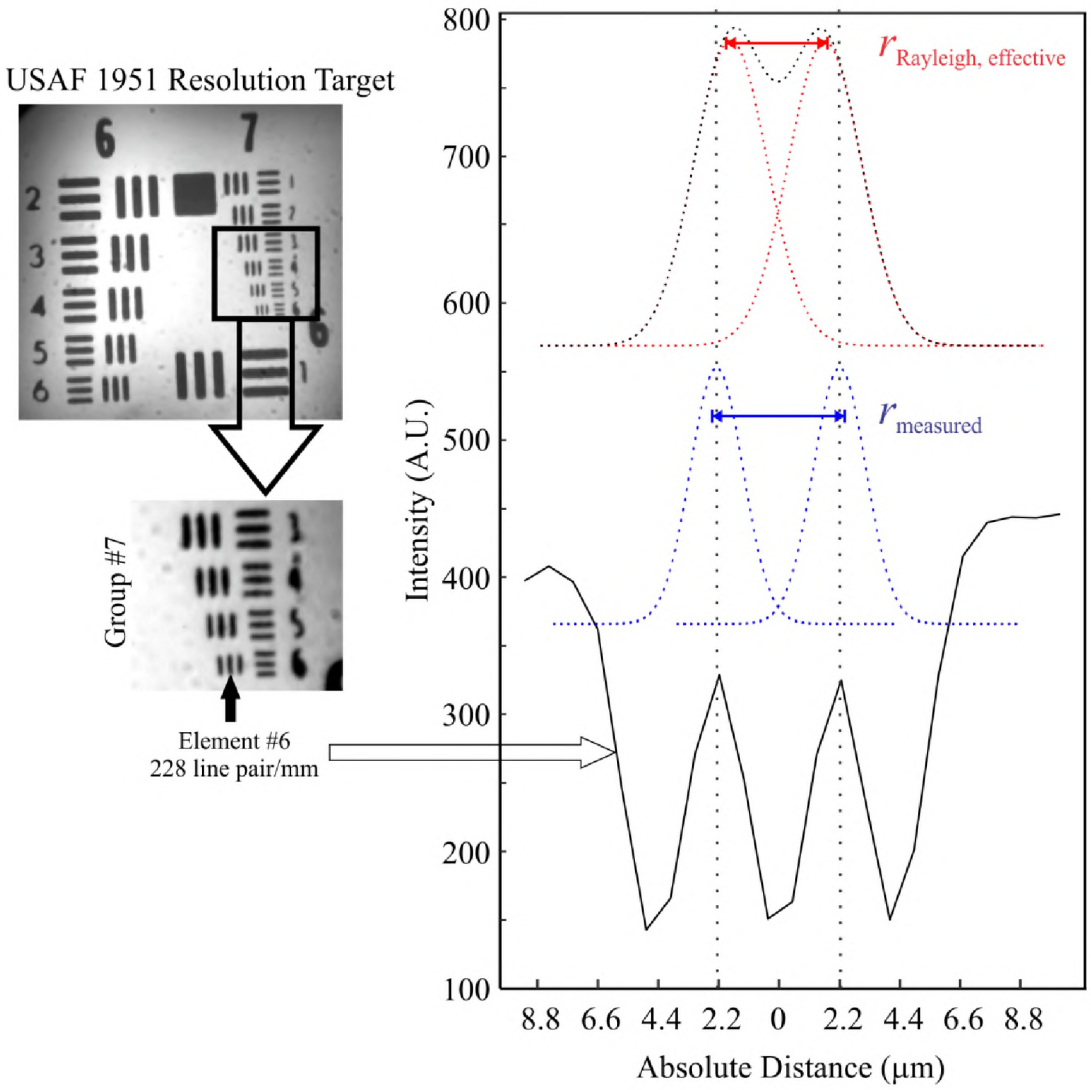

Figure 19: Image of the 1951 USAF Resolution Target Acquired Using SPCTF Imaging Microscope. The line spacing for the element 6 in group 7 is 228 line-pair/mm. An intensity plot across the lines pairs of the element #6 is shown on the right along with the effective Rayleigh criteria for resolution illustrated.

4.2.3 SPCTF Hyperspectral Imaging of Pine Stem

To explore the potential of the SPCTF for use in widefield hyperspectral imaging, a series of images of a model sample were collected through the SPCTF as a function of its tuning wavelength. A stained pine stem cross-section was chosen as a model sample for its inherent color-contrast in the operating range of the SPCTF and its well-defined morphology.

The collected images, shown in Figure 20A, exhibit subtle wavelength-dependent changes in the intensity values between image frames. A bright filed image of the sample was also acquired (Figure 20B) by removing the SPCTF from the path. The hyperspectral data were processed using spectral identity mapping (SIM) analysis to reveal wavelength-dependent differences across the field of view.[187] A spectral identity map (SIM) was produced (Figure 20C) from the data in which shape variations in the spectra at each pixel location are exploited to generate a single pseudo color image. Pixels that exhibit different colors in the SIM image result correspond to differently shaped spectra in the image dataset. Because SIM is scale invariant, these color differences represent qualitative differences in composition. This data represents the first use of the SPCTF for spectral imaging.

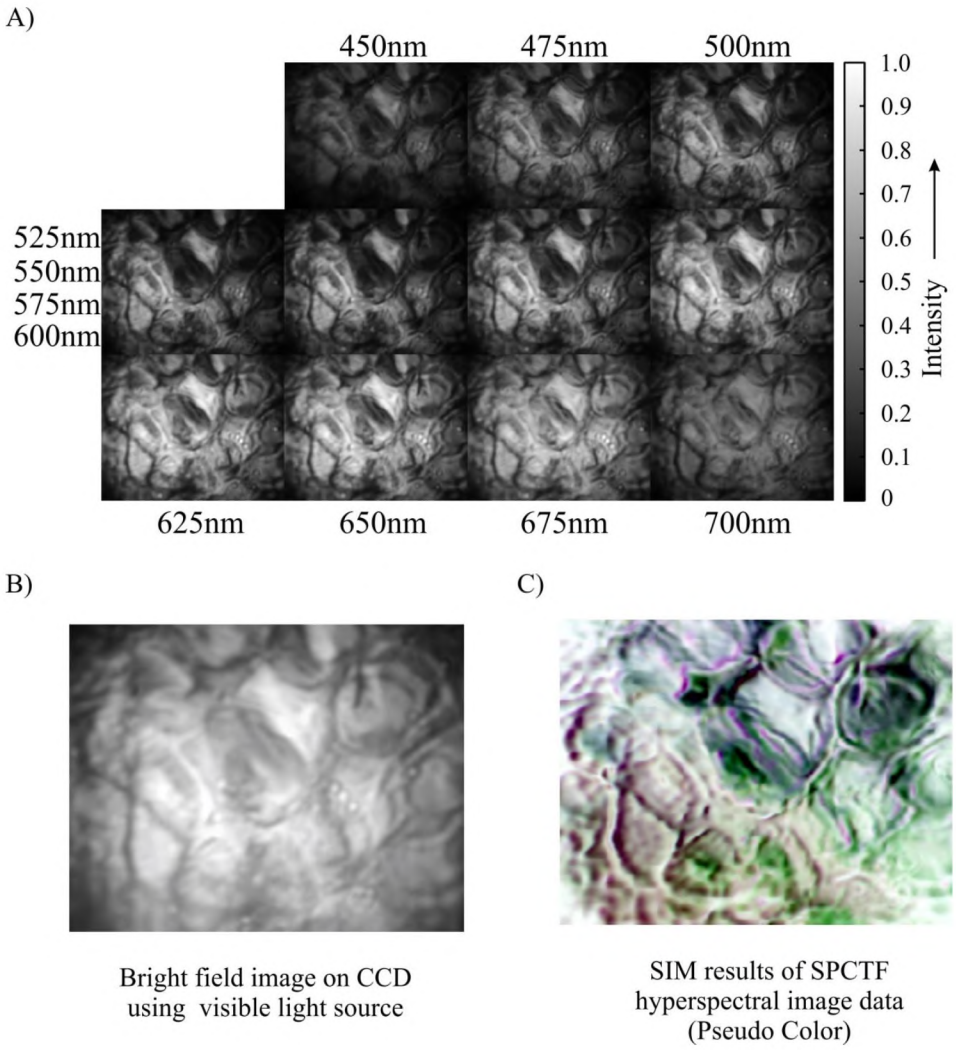

Figure 20: SPCTF Spectral Imaging. A) A set of widefield spectral images collected through the SPCTF as a function of passband wavelength are shown for wavelength between 450 nm and 700 nm at 25 nm increment. B) A bright field image of the sample is shown and was acquired by removing the SPCTF. C) A spectral identity map (SIM) of the image data shows qualitative changes in sample composition.

4.2.4 Short-range and Long-range Surface Plasmon Polaritons in a Coupled System

Due to free electron scattering in the metal and surface roughness along the interfaces, SPPs localized to different regions on the metal films can experience different amounts of attenuation.[189-191] The attenuation range can span 100-fold or more, leading to a spread of SPP propagation distances. Therefore, only some of SPPs will meet the resonance conditions of the SPCTF cavity where their electric field components normal to the interface are either in phase or out of phase. Those SPPs which experience little attenuation exhibit greater propagation lengths and are known as long-range SPPs (LRSPPs). The short-range SPPs (SRSPPs) can be highly attenuated, thereby producing more localized effects across shorter distances.

As the thickness of the airgap in the SPCTF varies the maxima in the transmitted signal move with respect to the minima in the reflected signal for both, the LRSPPs and the SRSPPs. The shift in the transmitted maxima or reflected minima of the SPCTF are not independent of each other. But, there exist conditions of the airgaps at which this shift is the least. For understanding the resonance conditions of the LRSPPs and the SRSPPs it is important to look at the Poynting vector field ($\vec{S}$) and the electric field component in the direction parallel to the interfaces (E_x) as a function of position within the dielectric cavity of the SPCTF. The Poynting vector is the energy transfer per unit area per unit time of an electromagnetic field. Poynting vector has both the direction and magnitude and it represents directional energy flux, and it is given as $\vec{S} = \vec{E} \times \vec{H}$, where $\vec{E}$ is the electric field vector and $\vec{H}$ is the magnetic field's auxiliary field vector. The electric field

$\vec{E}$ is a vector quantity, and it gives vector field in three-dimension. The electric field $\vec{E}$ has components, E_x, E_y, and E_z that defines the electric field in x- , y- and z-direction.

From the calculation by Welford and Sambles[186], presented here is an illustration of the Poynting vector (Figure 21) and the E_x component of the field (Figure 22) in the dielectric gap for the LRSPPs and the SRSPPs. The horizontal axis in the presentation of Poynting vector and the E_x component of the field is z-direction, while the vertical axis represents the x-direction.

Poynting vector illustration of SRSPPs (Figure21B) suggests that it has more energy in the metal than the dielectric gap where it approaches zero, compare to LRSPPs (Figure 20A). Due to damping in the metal, energy loss in the SRSPPs coupling mode is greater than that of LRSPPs, hence the transmission maxima are smaller for SRSPPs than that of LRSPPs.

Illustration of the E_x component of the electric field for the LRSPPs (Figure 22A) showing node in the airgap because of the electron oscillations in phase with each other at both the metal-air interfaces resulting in greater coupling of energy across the gap, resulting in higher transmittance compare to SRSPPs (Figure 22B).

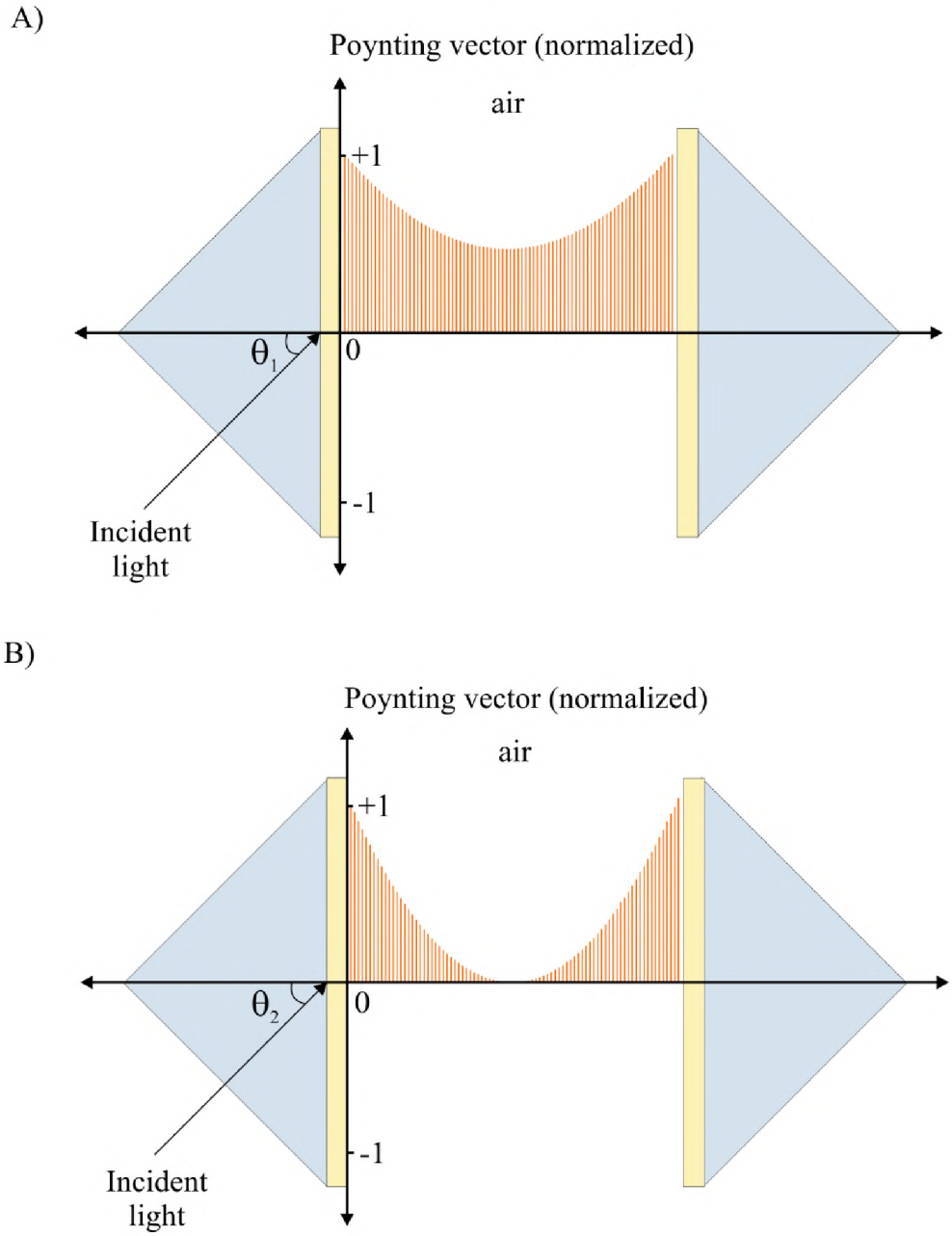

Figure 21. Illustration of Poynting Vector Profile for Surface Plasmon Coupled (Metal-Dielectric-Metal) System. A) The normalized Poynting vectors (orange) as position along the airgap corresponding to long-range surface plasmon at incident angle θ_1 is shown. B) The normalized Poynting vector as position along the airgap corresponding to short-range surface plasmon at incident angle θ_2 is shown. Here $\theta_1 > \theta_2$.

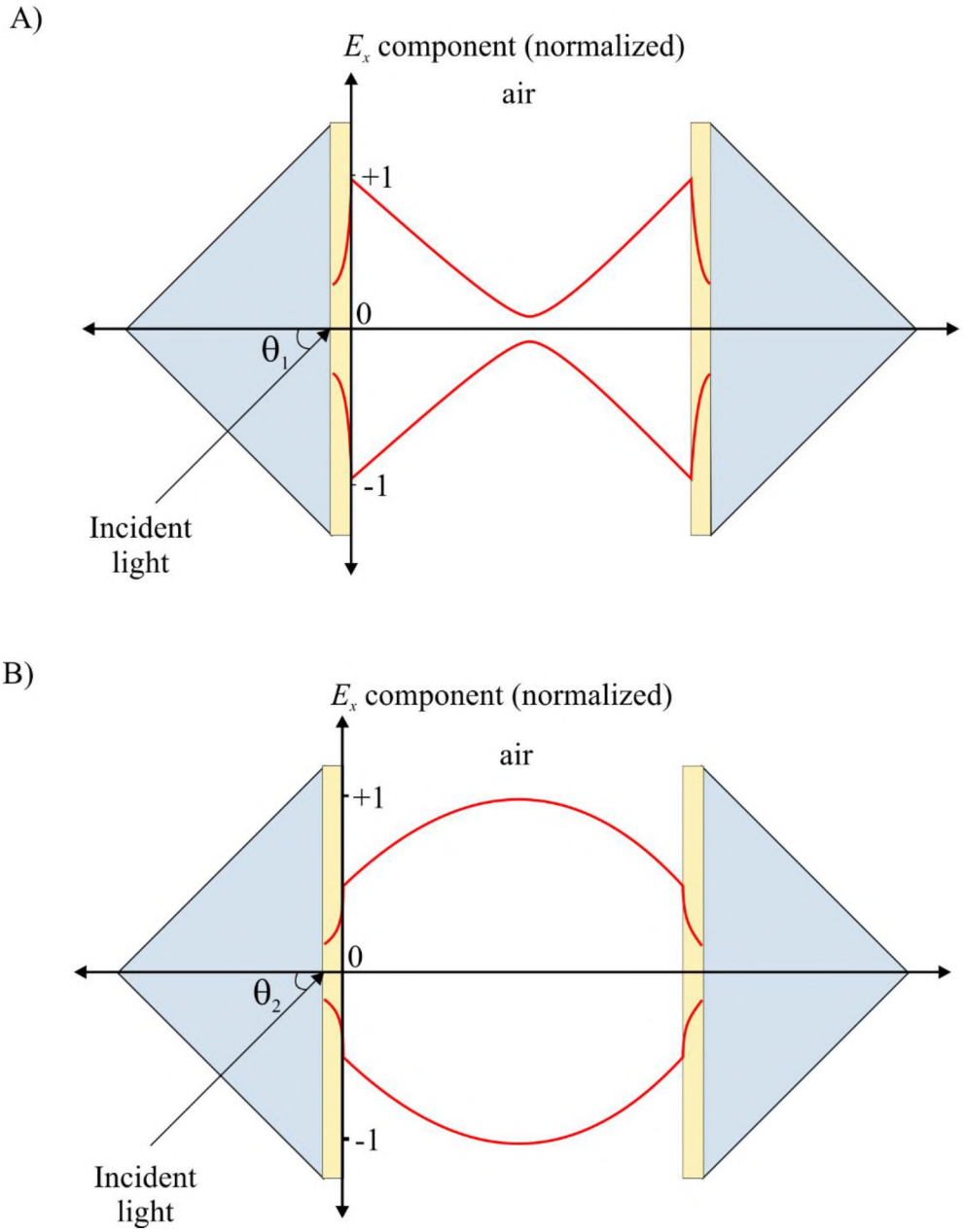

Figure 22: Illustration of the Normalized E_x Component of the Electric Field as the Time Average Envelop Along the Airgap. A) Electric field profile (red) for long-range surface plasmon at θ_1 is shown B) Electric field profile (red) for short-range surface plasmon at θ_2 is shown. Here $\theta_1 > \theta_2$ and prism size not to scale.

For a large range of airgap thickness the LRSPPs may be excited and the corresponding wave vector increases progressively as the airgap is reduced. For a fairly small (<270 nm) airgap only the LRSPPs exist. At a greater airgap SRSPPs may be excited at low angles of incident. Increasing the airgap further (~586 nm) causes the LRSPP and the SRSPP resonance to move closer to the θ_{sp} for a single interface in the Kretschmann-Raether configuration. Progressively increasing the airgap thickness causes the LRSPPs and the SRSPPs to converge. For a small change in the airgap thickness, the SRSPP wave vector changes by more than the LRSPP wave vector, hence the resonance angle moves more for the SRSPPs.[186] If the prism hypotenuses are not parallel or wedged instead, the SRSPPs will be the most affected, resulting in the more severe broadening of the SPCTF transmittance.

4.2.5 Selecting LRSPPs Coupling Mode with Monochromatic Light

The distances over which SPPs propagate are dependent on the amount of attenuation. Free electron scattering in the metal and surface roughness at the interfaces are important causes of SPP attenuation that can adversely affect the performance of plasmonic devices. While low attenuation leads to the sought-after LRSPPs, plasmonic devices often have imperfections that lead to the formation of both SRSPPs and LRSPPs. Because the SPCTF cavity is tunable, the LRSPPs can be preferentially selected over the SRSPPs by choosing the largest gap distance capable of generating SPPs at the desired wavelength. If the hypotenuses of the two prisms were not parallel if instead, they are wedged, wavelength broadening of the plasmon coupling occurs.

Using monochromatic light, the transmitted light corresponding to the LRSPP and the SRSPP modes can be observed. Figure 23 shows the SPCTF passband intensity for 650 nm laser light when the SPCTF is rotated over a ±6° range of incident angles. The transmittance as a function of wavelength and incident angle is represented as top-down view of the surface plot where red corresponds to higher transmittance value and blue color correspond to lower (near zero). The data was collected using the apparatus shown in Figure 16 with slight modification to accommodate range of incident angles. For a smaller airgap, two transmitted components that correspond to the SRSPPs and the LRSPPs can be seen. Increasing the airgap by small increments (Figure 23) leads to a converging of the SRSPPs and LRSPPs.

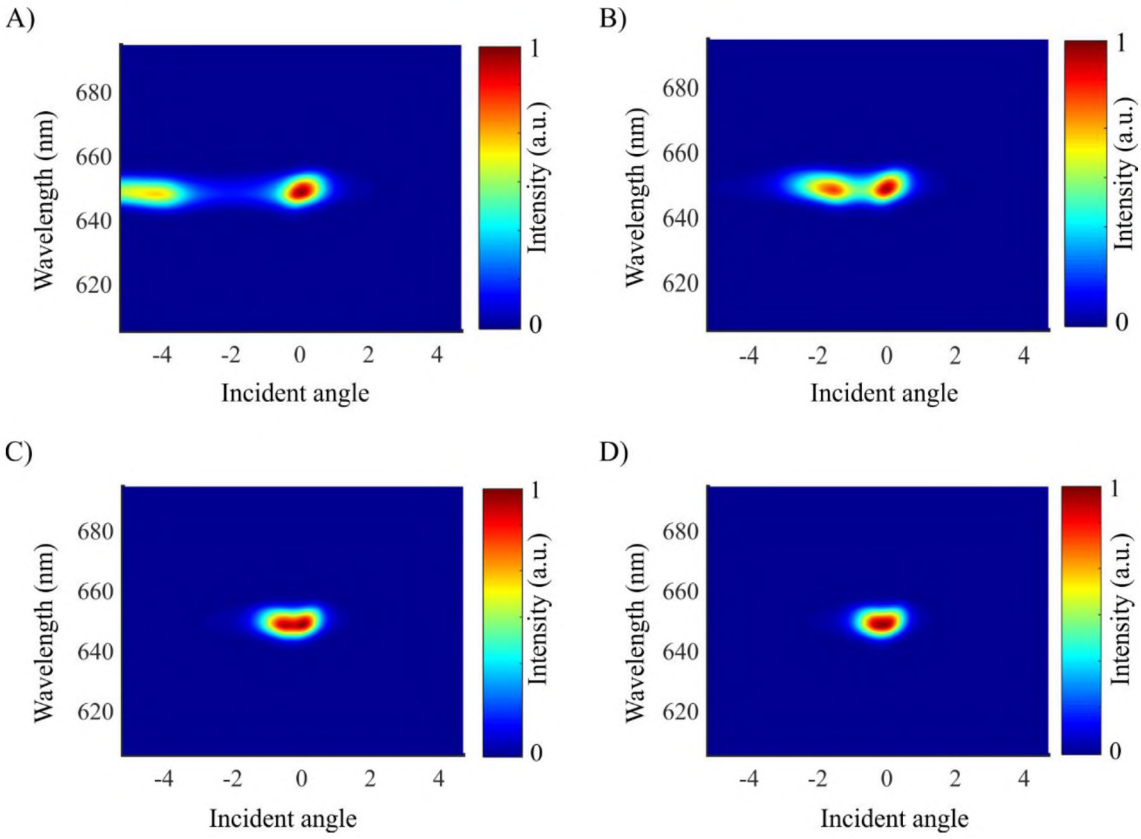

Figure 23: The Dependence of SRSPPs and LRSPPs on Airgap Distance in the SPCTF. A) Laser at 650 nm couples over a range of incident angles in the SPCTF. Two overlapping bands are observable and represent resonant coupling of both SRSPPs and LRSPPs. B) and C) as the airgap increases the LRSPPs and SRSPPs are converging D) At a greater airgap, only LRSPPs are able to couple with the incident light.

In Figure 24, the transmission band for 650nm is extracted from the data presented in Figure 23 and two separate bands are observable, a less intense band for SRSPPs at ~4.2° and a more intense, yet narrower, LRSPPs band at 0°. By increasing the airgap at very small increments, the SRSPP band converges towards the LRSPP band. Because SRSPPs are more localized, the influence of their fields more rapidly diminishes with distance than the LRSPPs. Increasing the SPCTF gap distance even further lessens the resonance ability of SRSPP in the cavity and provides a way to distinguish the LRSPPs from the SRSPPs.

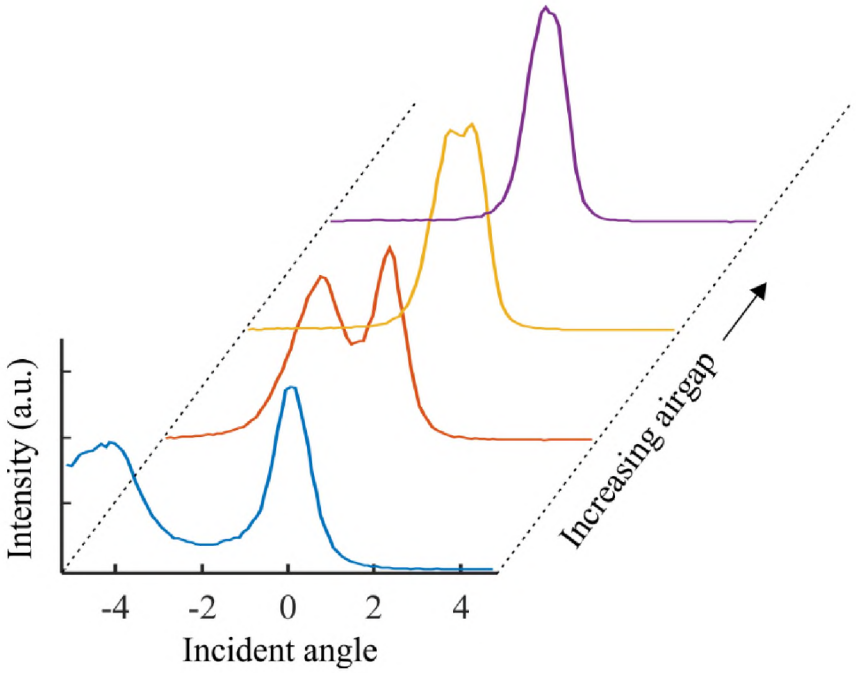

Figure 24: Converging of the SRSPPs and LRSPPs with Increasing Airgap for 650 nm Light.

CHAPTER 5

EFFECT OF DISPERSION ON SURFACE PLASMON COUPLING AND SPCTF BANDPASS

The calculated and measured reflectance for the metal-dielectric interface in the Kretschmann-Raether configuration are presented in chapter 3. The findings in chapter 3 demonstrated the angular sensitivity of the surface plasmon coupling. In this chapter the reflectance at the metal-dielectric interface for the Kretschmann-Raether configuration is measured using angularly dispersed incident light as function of incident angle and wavelength. Also presented is the bandpass of the SPCTF with angularly dispersed light. By exploiting the angular sensitivity of the surface plasmon coupling, the effective bandpass of the SPCTF is reduced.

5.1 Experimental and Methodology

5.1.1 Apparatus for the Measurement of the Reflectance of Angularly Dispersed Light as a Function of Incident Angle and of Wavelength

Because the formation of SPPs is very sensitive to the angle of incident light, the use of angularly dispersed light can significantly reduce the spectral bandwidth of light that can couple to SPPs. There are a number of applications that would benefit from the use of thin transmissive dispersers in combination with plasmonic devices to provide narrow passband tuning. To test the efficacy of this approach, the reflectance of angularly dispersed light from the prism hypotenuse is measured using a modified version of the apparatus described in Figure 10. In the first of two modifications, a transmission grating (Thorlabs, GT25-06V) was placed in the optical path immediately before the prism. The angular change in the optic path caused by the diffraction grating necessitated the second modification, a repositioning of the dual stage and fiber collection optics as shown in Figure 25.

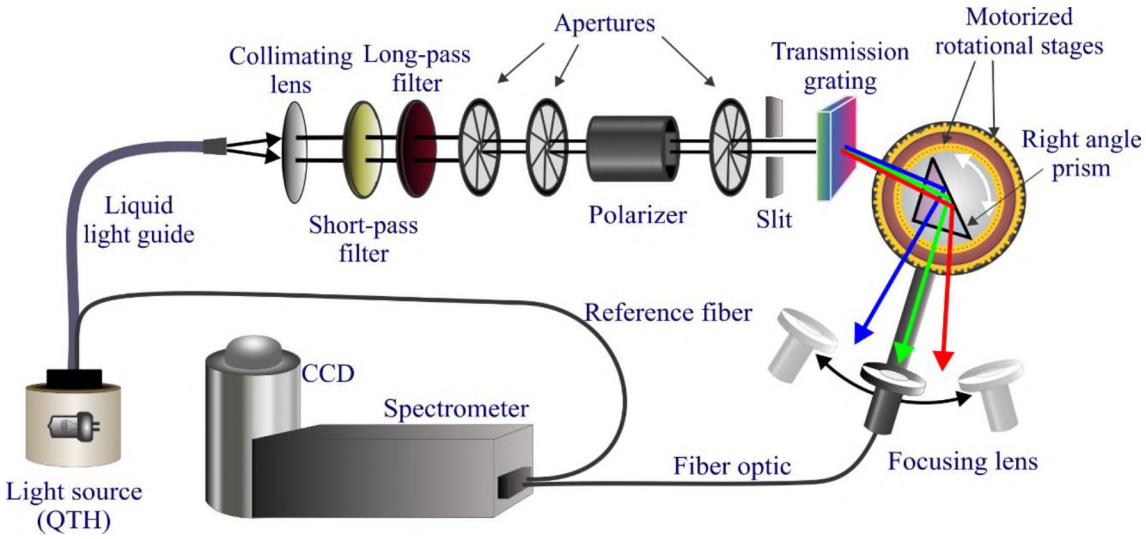

Figure 25: Schematic Diagram of the Optical Setup for Reflectance Measurements Using Angularly Dispersed Light. The apparatus described in section 3.1.2 is modified by placing a 600 grooves/mm transmission grating before the prism to achieve angular spread in the incident light. A right-angle prism with 48nm thick Ag coating on its hypotenuse is placed in the path of the strongest diffraction order of the grating. Since the reflected light is angularly dispersed, it is necessary to measure the reflected light at all angles in the dispersed beam. This was accomplished by recording the spectrum for incremental position of the rotating stage that was affixed to the collection optics.

The data collection procedure previously described in section 3.1.2, was modified so that now for each position of the prism (each incident angle) with respect to the incoming light from the grating, spectra at 70 neighboring positions were collected. A total of 14000 spectra, each covering the wavelength range between 500 nm and 850 nm, were recorded of the reflected angularly dispersed light over a 20^{o} range of incident angles Because the light is collected over a range of reflected angles for each orientation of the prism, and because each reflected angle corresponds to a different wavelength, most of which are not generating SPPs, it is not necessary to take a separate spectrum of the illumination in order to calculate the transmittance.

Because the incident angles in the dispersed beam are above the critical angle, the set of maxima extracted from each spectrum acquired for one prism orientation, after subtracting the background spectrum, is an envelop function that matches the illumination spectrum except in the vicinity of the surface plasmon-coupled wavelengths. The neighboring sets of envelop functions, acquired for other prism orientations that exhibit a wavelength shift in the SPP coupling, can be used to establish an intensity surface as a function of wavelength and prism orientation angle. Surface contours that neighbor the plasmon intensity dip in the surface can be used to make accurate estimates of the illumination intensity in the plasmon dip regions. This self-referenced approach avoids many of the experimental errors and alignment challenges related to removing the prism so that a properly scaled illumination spectrum can be acquired.

5.1.2 Characterization of the SPCTF Coupled to a Dispersive Element.

The bandpass and acceptance angle of the SPCTF was determined for angularly dispersed light using the apparatus shown in Figure 26. A reflective grating (Thorlabs, 600 grooves/mm) was placed in the optical path to provide angular dispersion. Although not shown, the grating was mounted on a rotational mount (Thorlabs, PR01) to enable wavelength tuning along the optical path of the SPCTF. Spectra of the transmitted light were acquired over a range of SPCTF angles for each of several gap distances using a rotational stage (Cognisys, ROTO_TAB_01). The collection fiber remained fixed in position.

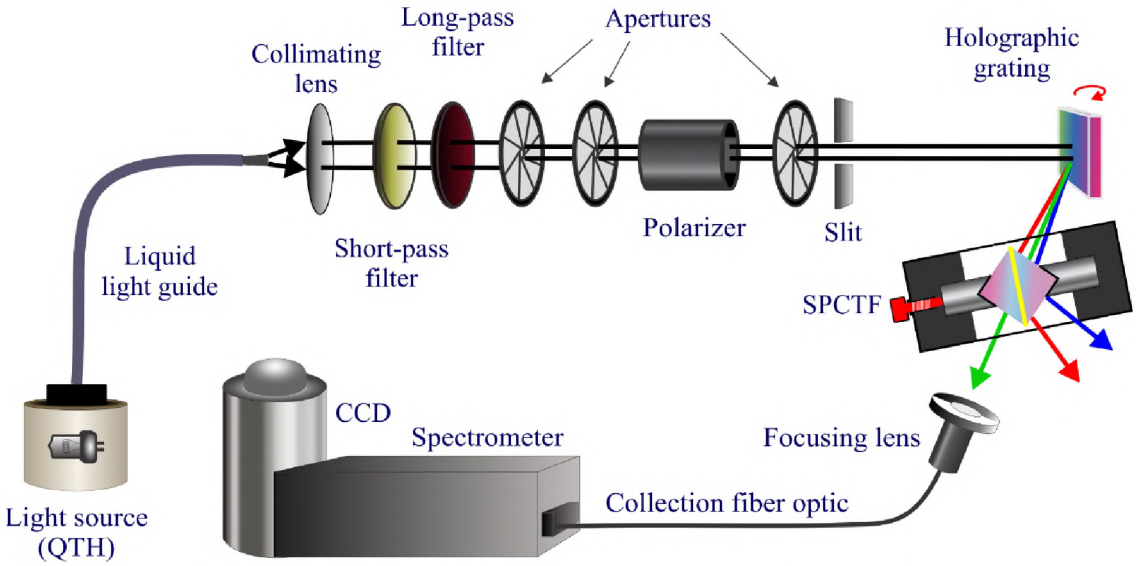

Figure 26: Apparatus for Measuring the Bandpass and Angle of Acceptance of the SPCTF Coupled to a Dispersive Element.

5.2 Result and Discussion

5.2.1 Reflectance of Dispersed Light from the Glass-Metal Interface

The apparatus used for collecting the angularly dispersed light is described in section 5.1.1 and Figure 25. As described previously, neighboring sets of spectra were collected for a range of incident angles on the prism hypotenuse. Here it is important to note that each wavelength will have a different angle of incident onto the prism hypotenuse, because the light is angularly dispersed by the grating. Hence angle used to generate the plots of reflectance for angularly dispersed light relies on the incident angle of the center wavelength of the range of interest with respect to the prism hypotenuse.

For each position of the prism, a set of 70 spectra were collected in the vicinity of the angle of reflectance by scanning the collection fiber, this was done to collect as much of the angularly dispersed light as possible. The process was repeated over the range of incident angles. The background corrected intensities of one set of spectra obtained for one incident angle is shown in Figure 27. In Figure 27A, the intensity plotted as a function of collection angle and wavelength. The collection angle is reported with respect to the center angle, an estimate of the reflected angle based on the incident angle. In Figure 27B, the intensities as a function of wavelength are shown to accentuate the overall envelop shape of the entire set of spectra. At the incident angles where the surface plasmons couple, there will be a corresponding dip in the reflectance spectra of that set, but the dip would be spread across multiple acquisition angles as shown in Figure 28 and 29.

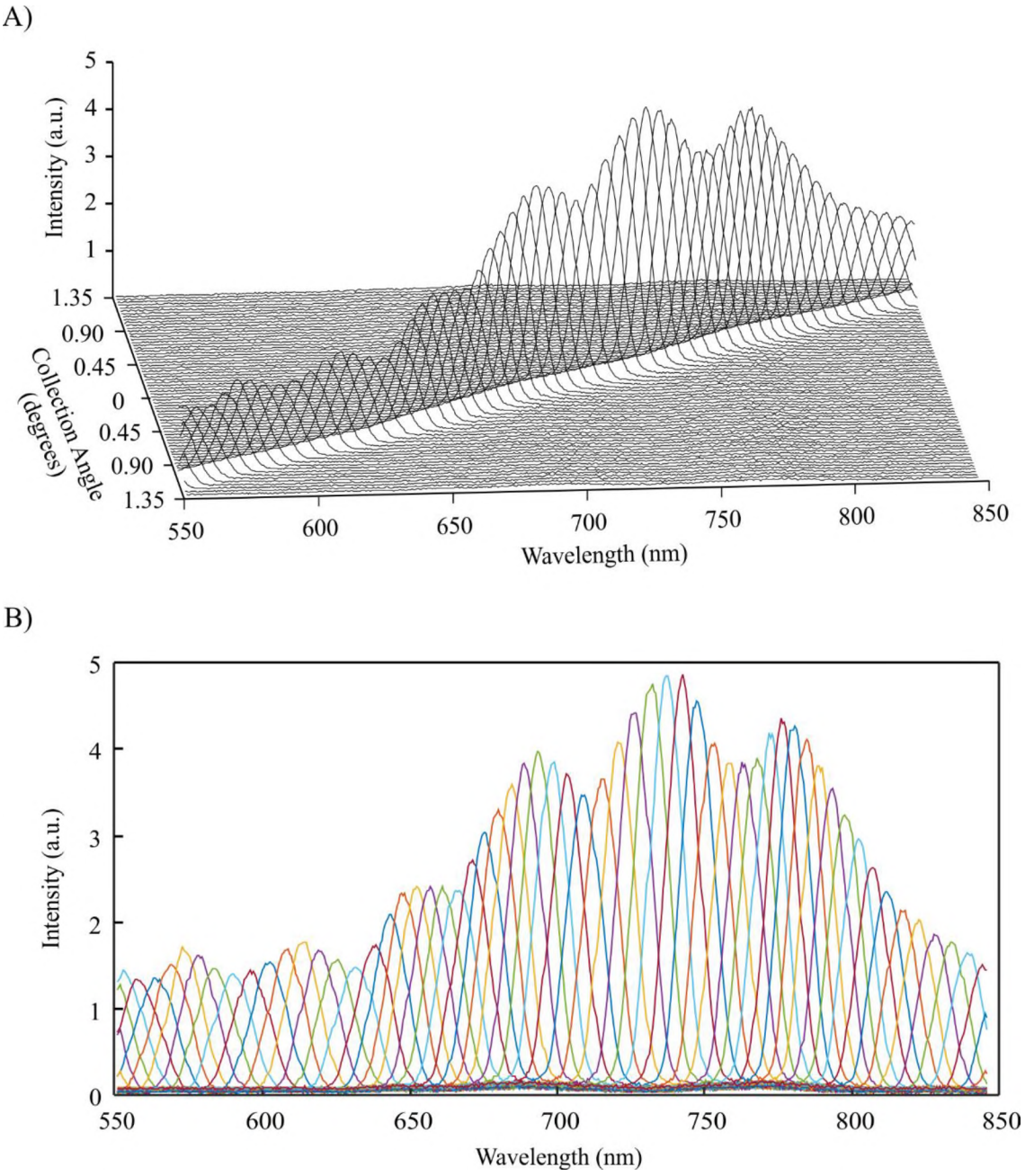

Figure 27: Preprocessing Reflected Intensity Acquired as a Function of Collection Angle for Angularly Dispersed Light. Background corrected set of 70 neighboring spectra for one position of the prism is shown in A) where the spectra are plotted in 3-dimensional space and in the B) same data plotted in 2-dimesion to accentuate the overall envelop profile of the reflected light.

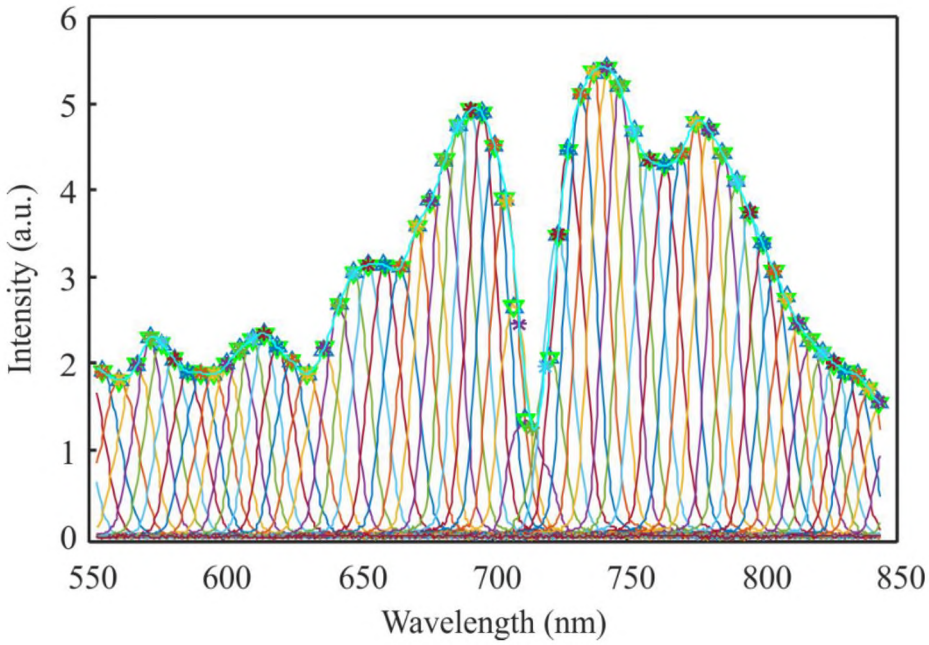

Figure 28: Data with Peak Centers Marked for Extraction of the Envelop Function of the Angularly Dispersed Reflected Light. Shown in the figure is a set of 70 spectra for one incident angle onto the prism hypotenuse. The process was repeated for total of 200 sets corresponding to range of incident angles.

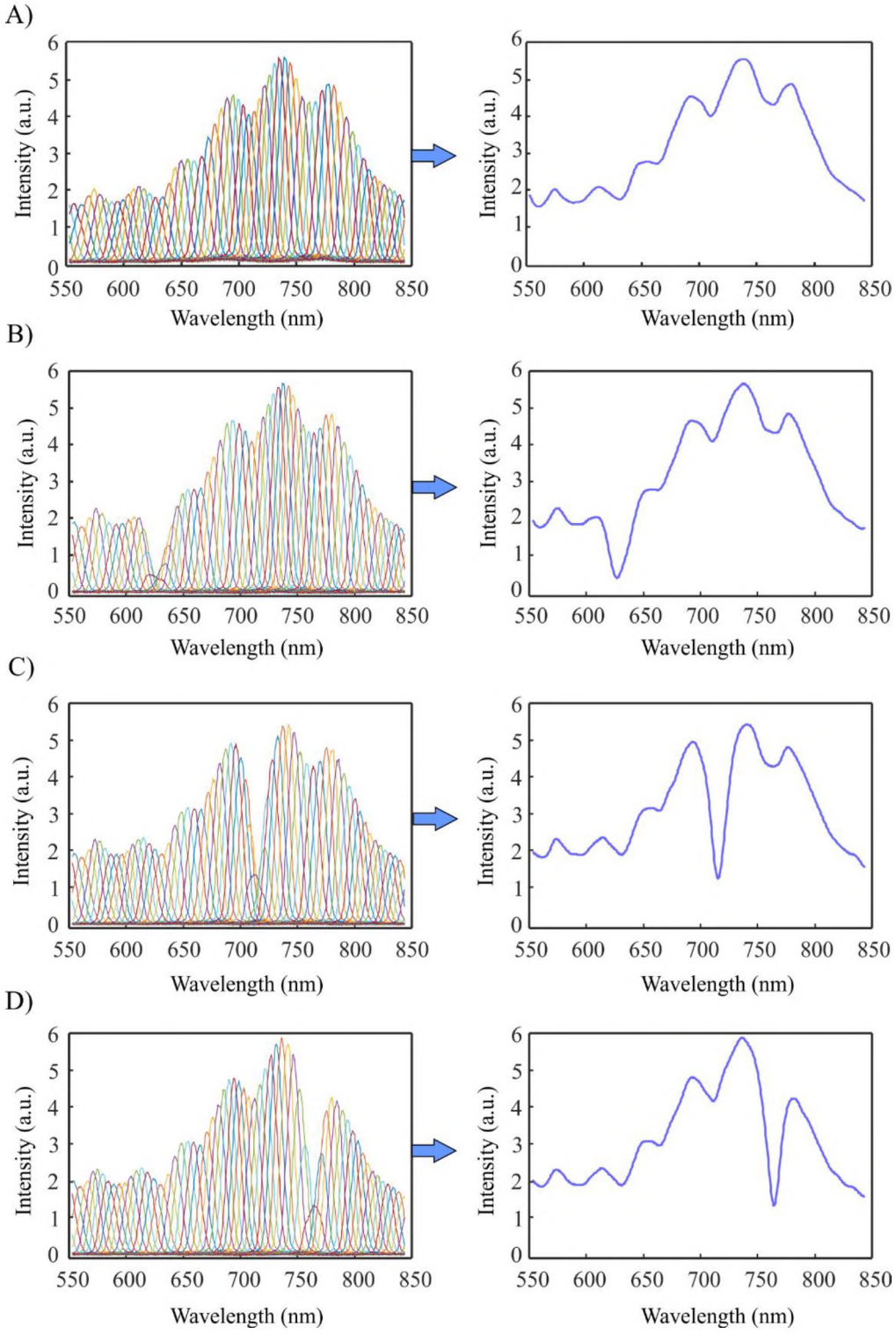

Figure 29: Extracted Envelop Functions from the Data. Only four sets are shown here.

For the calculation of the reflectance, it is important to extract the envelop function from each set of 70 spectra. An algorithm, written for MATLAB, was created to accomplish this task. The algorithm operated on each set of 70 spectra that were acquired for a given illumination angle on the prism. For each individual spectrum, the peak position was identified using a correlation calculation with respect to a predetermined peak shape. The plot of peak intensity vs. wavelength was extracted and fit using a cubic spline. The envelop function of the set of 70 spectra is given by the spline result. Because the peaks in the region of a surface plasmon dip, do not have the characteristic peak shape, the algorithm exploited the periodicity of the peaks in the wavelength dimension to estimate the peak center wavelength for the peaks in the region of the dip. The intensities at these positions were used to calculate the envelop function at these wavelengths (Figure 28).

The plots in Figure 29 show the extracted envelop functions for sets of spectra acquired at different incident angles onto the prism hypotenuse. For the calculation of reflectance, the envelop data were then processed for calculating the initial light intensity via self-referencing. In the self-referencing method, the intensities at the region away from the dip is used to estimate the illumination envelop. The measured reflectance is plotted as surface in Figure 30. The redder regions exhibit higher reflectance values than bluer regions.

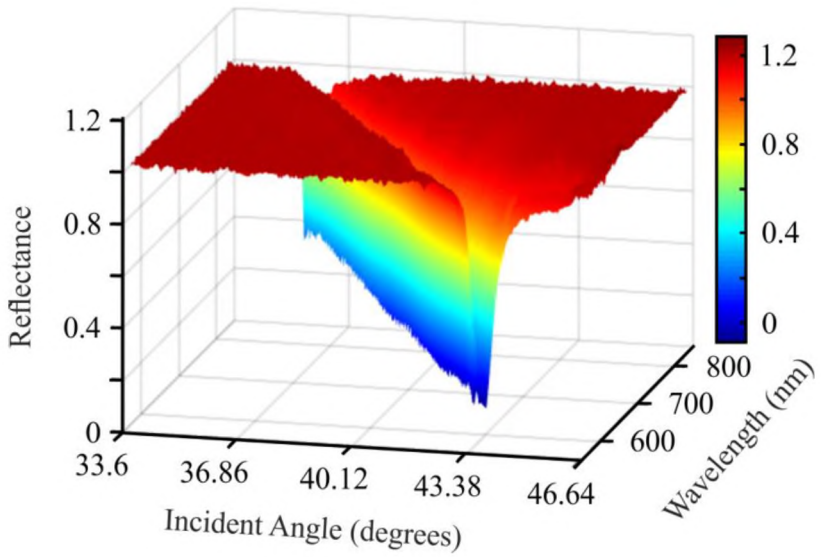

Figure 30: Reflectance Data as a Function of Wavelength and Incident Angle for Angularly Dispersed Illumination. The incident angle onto prism face were measured for center wavelength (~700 nm) and from that incident angle on to hypotenuse were calculated.

The top-down view of the surface from Figure 30 is shown in Figure 31A. A comparison of the image in Figure 31A to the one shown in Figure 14B reveals that the use of a dispersive element in the optical path of the prism reduces the wavelength bandwidth over which photon-polariton coupling can occur. The measured bandwidth using dispersed light is plotted in Figure 31D. This data demonstrates that angular dispersion in conjunction with plasmonic excitation can be used to create a narrowband optical filter. A description of the potential impact of this illumination approach is given in section 5.2.2 for the SPCTF.

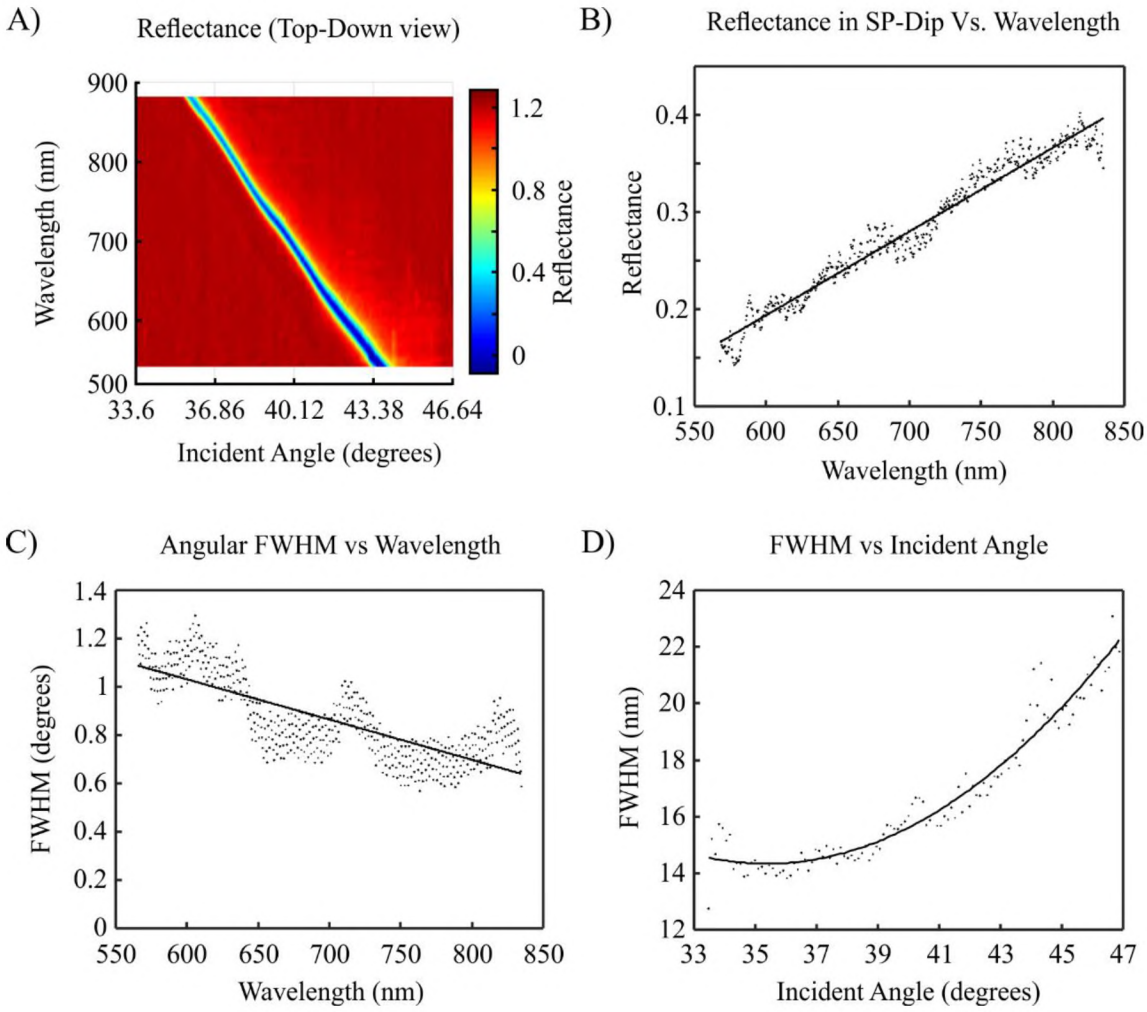

Figure 31. Narrow Band Coupling of the SPPs with Angularly Dispersed Illumination. A) Top-down view of the reflectance surface from Figure 29 is shown. The location of the surface plasmon dip is shown in blue while red regions indicate reflectance values that approach 1. B) Measured reflectance minima in the dip as a function of wavelength is shown. C) Angular bandpass as a function of wavelength is plotted. D) Bandpass in nm as a function of incident angle is plotted which shows the use of angularly dispersed light, narrows the optical bandwidth, over which photon-polariton coupling can occur.

5.2.2 SPCTF Acceptance Angle and Bandpass with Angularly Dispersed Light.

To assess its potential as a tunable widefield image filter, the SPCTF passband was studied as a function of wavelength and illumination angle using broadband angularly dispersed light (Figure 32). The SPCTF was tuned to three different wavelengths that correspond to laser light at 532 nm, 650 nm and 785 nm. The airgap was set to a suitably wide position so as to ensure one coupling mode, LRSPP coupling, as described in section 4.2.5. Bandpass of the SPCTF using dispersed white light was measured while tuned at 532 nm, 650 nm and 785 nm light. The nominal bandpass (FWHM) was measured to be 7.23 nm within the range of operations (550 nm to 850 nm) and the bandpass plots are shown in Figure 32 with their respective FWHM. Bandpass was reduced by factor of about 10, compared to the bandpass with collimated light, described in section 4.2.1.

The use of the SPCTF as a widefield filter for imaging applications requires a sufficiently large acceptance angle to permit image reformation. Plots for the acceptance angle measured for 532 nm, 650 nm and 785 nm are shown in Figure 33. The acceptance angle describes the steradian field of view over which the SPCTF functions. While apertures can be used to select those components of the Fourier space that are better collimated, doing so greatly diminishes the light intensity and reduces the signal-to-noise level. The Numerical Aperture (NA) is a measure of how much light can be collected by an optical component such as an optical filter, optical fiber or a microscope objective. By measuring the acceptance angle of the SPCTF we can calculate its NA. The. NA is given by $NA = n\,sin\theta$, where θ is half of the acceptance angle and n is the refractive index.

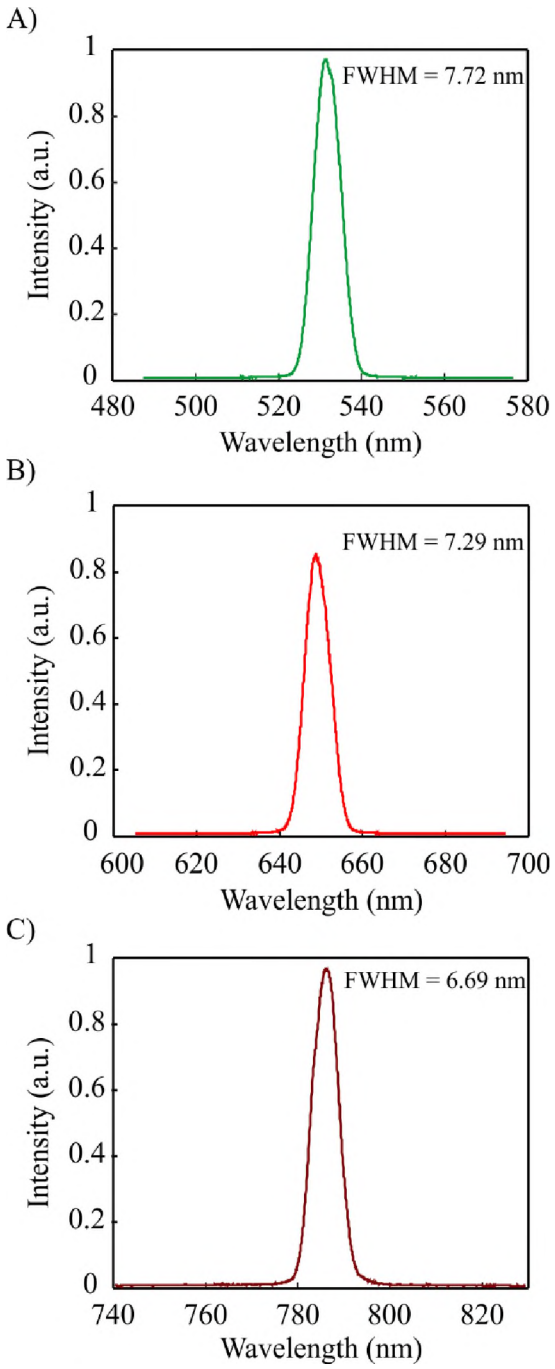

Figure 32: The Bandpass of the SPCTF Coupled to a Dispersive Element. Plots of the SPCTF passband are shown for the A) 532 nm, B) 650 nm, and C) 785 nm passbands, as intensity vs wavelength using white light. The nominal bandpass of the SPCTF with the dispersive element is ~7.23 nm in the range between 550 nm and 850 nm.

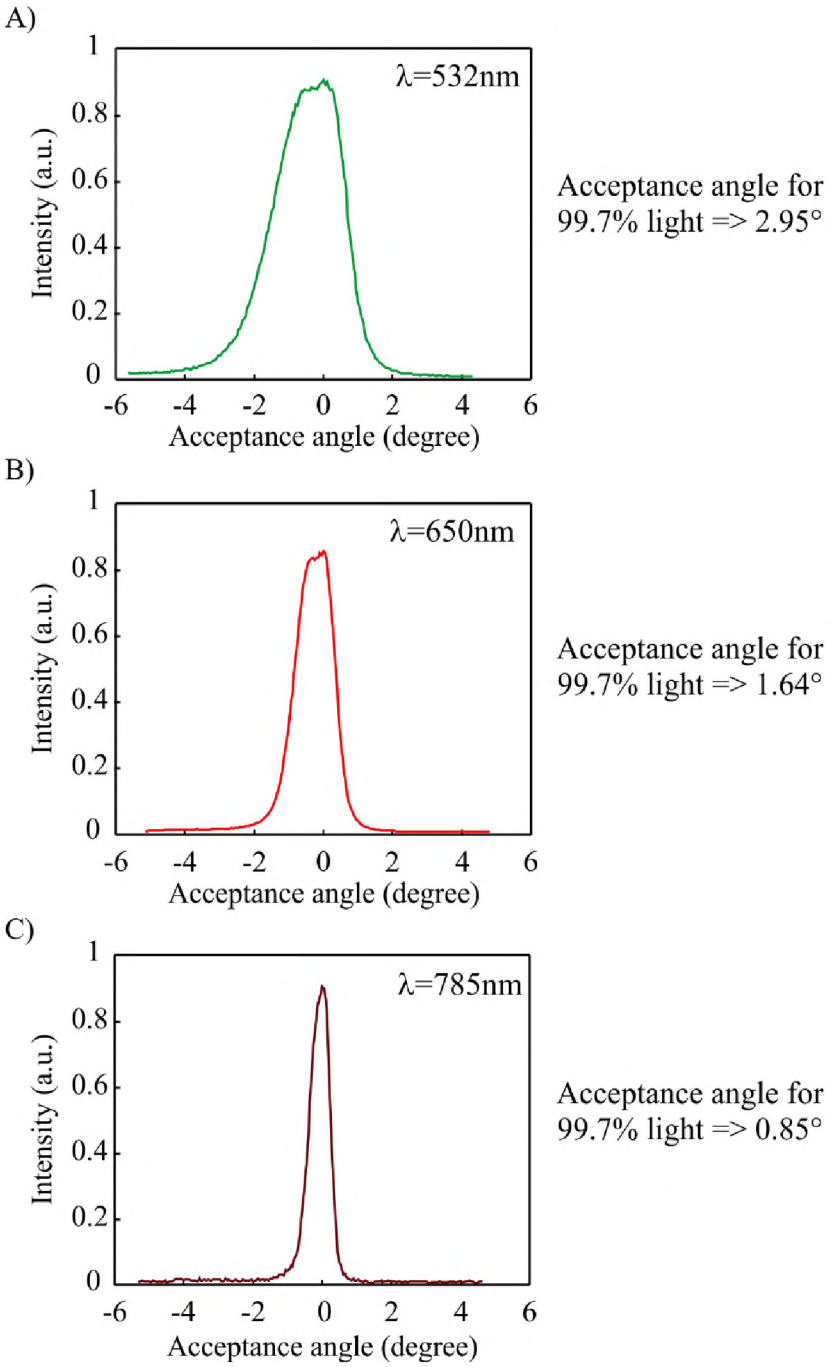

Figure 33. The Acceptance Angle of the SPCTF. Plots of the SPCTF acceptance angle are shown for the passband wavelength A) 532 nm, B) 650 nm, and C) 785 nm. The zero-angle position is selected as the angle in which the transmittance of the tuning wavelength is optimal.

The use of the SPCTF in widefield imaging applications requires the use of lenses before and after the SPCTF, which places the SPCTF in the Fourier space. The nominal Fourier space NA observed for SPCTF in the presence of angularly dispersed light was 0.04°,0.02°, and 0.01° for tuning wavelength 532 nm, 650 nm and 785 nm respectively. While the use of a grating in the optical path before a widefield tunable filter seems questionable and counterintuitive, the SPCTF is designed to be miniaturized into a monolithic element so that it can be directly integrated with detector arrays as described in section 6.2 and Figure 35.

CHAPTER 6

CONCLUSION AND RECOMMENDATIONS FOR FUTURE WORK

6.1 Conclusion

A new type of tunable wavelength filter, based on surface plasmon coupling in a resonant cavity, has been introduced. The SPCTF filter is constructed from two Kretschmann-Raether metal-coated prisms. Empirical reflectance data from the glass-metal interface of the individual prism-element showed qualitative agreement with theoretical estimates. While very sensitive to the illumination angle (<2°), surface plasmon generation occurs over a broad range of wavelengths and produced a nominal bandpass of ~70 nm for a metal film thickness of 48 nm at wavelengths between 550 nm and 850 nm. To exploit the angular sensitivity as a way of reducing the SPCTF bandwidth, the prism-element reflectance was measured using angularly dispersed light.

Nominal bandwidths below 10 nm were achieved within the spectral region between 550 nm and 850 nm. Without any narrowing of the passband, the two-prism SPCTF also produced a bandpass of ~70 nm over the spectral range from 550 nm to 850 nm and exhibited a nominal percent transmittance of ~32%. Diffraction limited spatial resolution of the SPCTF has been demonstrates using 1951 USAF resolution target. In addition, Proof-of-concept spectral imaging was demonstrated using the SPCTF and the spectral identity map of the spectral image data confirmed wavelength dependent variability related to the qualitative compositional differences in the model sample. The use of dispersive element coupled to the SPCTF resulted in a 10-fold narrowing of the bandpass to ~7 nm (FWHM). The acceptance angle under these conditions was ~1.5°.

6.2 Recommendations for the Future Work

If the airgap in the SPCTF is replaced with low-index electro-optic material as shown in Figure 34, its refractive index can be controlled under the influence of an applied electric field. By changing the refractive index of the dielectric, the transmitted SPCTF wavelength can be altered. Hence a fixed angle input beam can be made to excite a specific SPP mode by varying the applied voltage.

Integrating the SPCTF with a highly dispersive tunable etalon (Figure 35A) enable compact, narrowband filtering of an optical signal. In addition, each pixel of an array detector could be integrated with its own hybrid SPCTF element (Figure 35B). Hence the SPCTF can be used to exploit the wavelength filtering superiority of (transmissive) dispersive gratings without having to rely on intensive computational methods for wavelength deconvolution in the image scene. In this case, the SPCTF effectively suppresses unwanted wavelength from the dispersed output of the etalon from being detected.

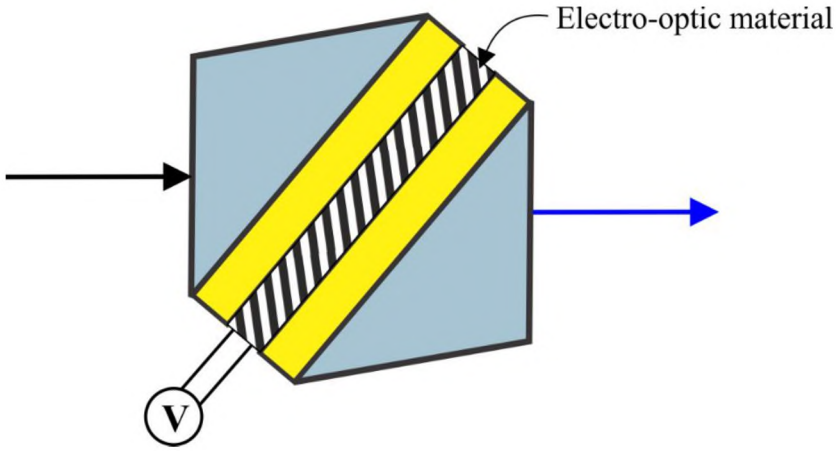

Figure 34: An Electro Optically Tuned SPCTF. Applying the electric field across the electro-optic material enables tuning of the SPCTF under electric control.

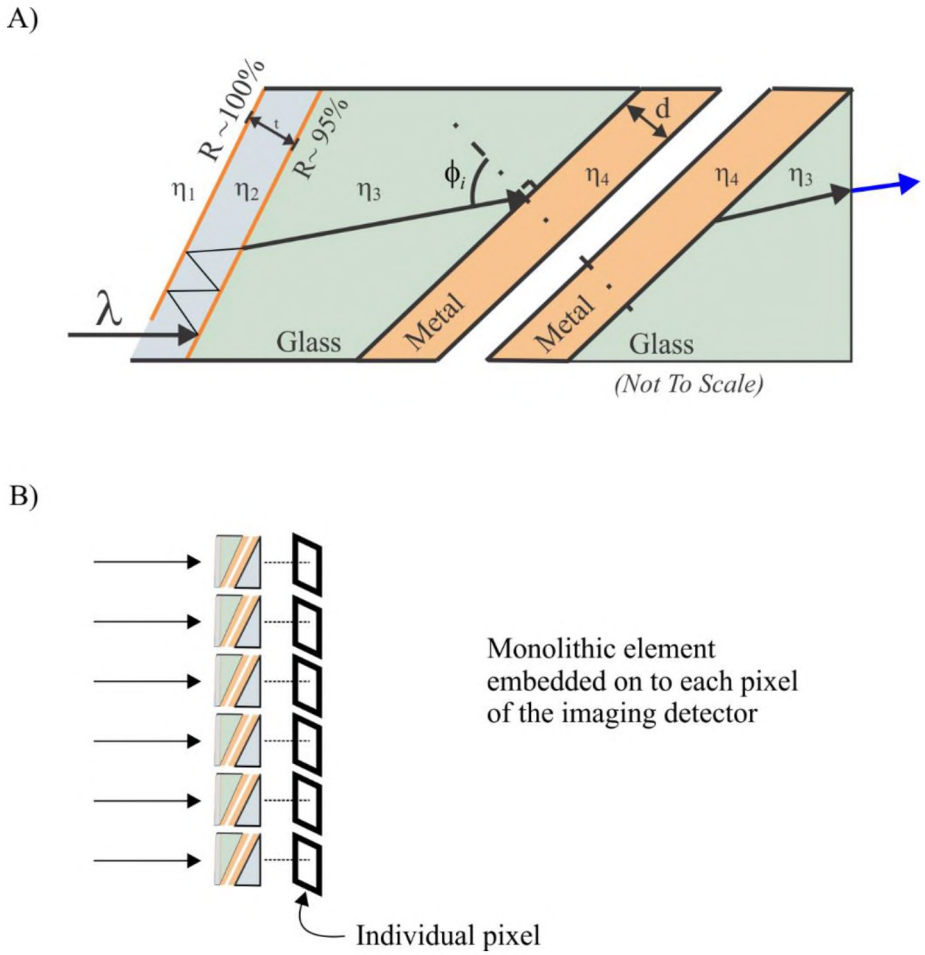

Figure 35: A Conceptual Design of a Monolithic Element. A) SPCTF when combined with interference filter can be miniaturized in to an integrated monolithic element. B) Monolithic SPCTF embedded on to each pixel of the imaging detector chip, it can be a 2-dimensional or a 3-dimensional array of pixels such as in the CCD or CMOS detector.

REFERENCES

1. Abuleil, M.; Abdulhalim, I., Narrowband multispectral liquid crystal tunable filter. *Optics Letters* **2016,** *41* (9), 1957-1960.

2. Zheng, J.; Wang, K.; Gao, H.; Lu, F.; Sun, L.; Zhuang, S. In *Multi-wavelength sensitive holographic polymer dispersed liquid crystal grating applied within image splitter for autostereoscopic display*, SPIE Optical Engineering+ Applications, International Society for Optics and Photonics: 2016; pp 995818-995818-9.

3. Patel, J. S.; Saifi, M. A.; Berreman, D. W.; Lin, C.; Andreadakis, N.; Lee, S. D., Electrically tunable optical filter for infrared wavelength using liquid crystals in a Fabry-Perot etalon. *Appllied Physics Letters* **1990,** *57* (17), 1718-1720.

4. Schaeberle, M. D.; Morris, H. R.; II, J. F. T.; Treado, P. J., Peer reviewed: Raman chemical imaging spectroscopy. *Analytical Chemistry* **1999,** *71* (5), 175A-181A.

5. Morris, H. R.; Turner, J. F.; Munro, B.; Ryntz, R. A.; Treado, P. J., Chemical imaging of thermoplastic olefin (TPO) surface architecture. *Langmuir* **1999,** *15* (8), 2961-2972.

6. Turner II, J. F.; Treado, P. J. In *LCTF Raman chemical imaging in the near infrared*, AeroSense'97, 1997; pp 280-283.

7. Marinelli, W. J.; Gittins, C. M.; Gelb, A. H.; Green, B. D., Tunable Fabry-Perot etalon-based long-wavelength infrared imaging spectroradiometer. *Applied Optics* **1999,** *38* (12), 2594-2604.

8. Pappas, D.; Matveev, O. I.; Smith, B. W.; Shepard, M. R.; Podshivalov, A. A.; Winefordner, J. D., Sealed-cell mercury resonance ionization imaging detector. *Applied Optics* **2000,** *39* (27), 4911-4917.

9. Temirov, J.; Chigarev, N.; Matveev, O.; Omenetto, N.; Smith, B.; Winefordner, J., A resonance ionization imaging detector based on cesium atomic vapor. *Spectrochimica Acta Part B: Atomic Spectroscopy* **2004,** *59* (5), 677-687.

10. Daly, J. T.; Bodkin, A.; Schneller, W. J.; Kerr, R. B.; Noto, J.; Haren, R.; Eismann, M. T.; Karch, B. K. In *Tunable narrow-band filter for LWIR hyperspectral imaging*, Proceedings of SPIE, 2000; pp 104-115.

11. Hufziger, K. T.; Bykov, S. V.; Asher, S. A., Raman Hyperspectral Imaging Spectrometer Utilizing Crystalline Colloidal Array Photonic Crystal Diffraction. *Applied Spectroscopy* **2014,** *68* (11), 1219-1223.

12. Hufziger, K. T.; Bykov, S. V.; Asher, S. A., Ultraviolet Raman Wide-Field Hyperspectral Imaging Spectrometer for Standoff Trace Explosive Detection. *Applied Spectroscopy* **2017,** *71* (2), 173-185.

13. Goetz, A. F. H., Three decades of hyperspectral remote sensing of the Earth: A personal view. *Remote Sensing of Environment* **2009,** *113*, S5-S16.

14. Ergin, L. N.; Bobba, V. N. R.; Turner, J. F. In *Unassisted reduction and segmentation of large hyperspectral image datasets*, Optics and Photonics for Information Processing XI, International Society for Optics and Photonics: 2017; p 103950M.

15. Calin, M. A.; Parasca, S. V.; Savastru, D.; Manea, D., Hyperspectral imaging in the medical field: present and future. *Applied Spectroscopy Reviews* **2014,** *49* (6), 435-447.

16. Kester, R. T.; Gao, L.; Bedard, N.; Tkaczyk, T. S. In *Real-time hyperspectral endoscope for early cancer diagnostics*, Advanced Biomedical and Clinical Diagnostic Systems Viii, International Society for Optics and Photonics: 2010; p 75550A.

17. Sahu, A.; McGoverin, C.; Pleshko, N.; Sorenmo, K.; Won, C.-H. In *Hyperspectral imaging system to discern malignant and benign canine mammary tumors*, Smart Biomedical and Physiological Sensor Technology X, International Society for Optics and Photonics: 2013; p 87190W.

18. Li, Q.; He, X.; Wang, Y.; Liu, H.; Xu, D.; Guo, F., Review of spectral imaging technology in biomedical engineering: achievements and challenges. *Journal of Biomedical Optics* **2013,** *18* (10), 100901.

19. Dhawan, A. P.; D'Alessandro, B.; Fu, X., Optical imaging modalities for biomedical applications. *IEEE Reviews in Biomedical Engineering* **2010,** *3*, 69-92.

20. Gowen, A.; O'donnell, C.; Cullen, P. J.; Bell, S., Recent applications of chemical imaging to pharmaceutical process monitoring and quality control. *European Journal of Pharmaceutics and Biopharmaceutics* **2008,** *69* (1), 10-22.

21. Gowen, A.; O'Donnell, C.; Cullen, P.; Downey, G.; Frias, J., Hyperspectral imaging–an emerging process analytical tool for food quality and safety control. *Trends in Food Science & Technology* **2007,** *18* (12), 590-598.

22. Gendrin, C.; Roggo, Y.; Collet, C., Pharmaceutical applications of vibrational chemical imaging and chemometrics: a review. *Journal of Pharmaceutical and Biomedical Analysis* **2008,** *48* (3), 533-553.

23. Lelong, C. C.; Pinet, P. C.; Poilvé, H., Hyperspectral imaging and stress mapping in agriculture: a case study on wheat in Beauce (France). *Remote Sensing of Environment* **1998,** *66* (2), 179-191.

24. Thenkabail, P. S.; Smith, R. B.; De Pauw, E., Hyperspectral vegetation indices and their relationships with agricultural crop characteristics. *Remote Sensing of Environment* **2000,** *71* (2), 158-182.

25. Inoue, Y.; Penuelas, J., An AOTF-based hyperspectral imaging system for field use in ecophysiological and agricultural applications. *International Journal of Remote Sensing* **2001,** *22* (18), 3883-3888.

26. Dale, L. M.; Thewis, A.; Boudry, C.; Rotar, I.; Dardenne, P.; Baeten, V.; Pierna, J. A. F., Hyperspectral imaging applications in agriculture and agro-food product quality and safety control: a review. *Applied Spectroscopy Reviews* **2013,** *48* (2), 142-159.

27. Xie, Y.; Sha, Z.; Yu, M., Remote sensing imagery in vegetation mapping: a review. *Journal of Plant Ecology* **2008,** *1* (1), 9-23.

28. Eismann, M. T. In *Hyperspectral remote sensing*, SPIE Bellingham: 2012.

29. Treitz, P. M.; Howarth, P. J., Hyperspectral remote sensing for estimating biophysical parameters of forest ecosystems. *Progress in Physical Geography* **1999,** *23* (3), 359-390.

30. Heiden, U.; Segl, K.; Roessner, S.; Kaufmann, H., Determination of robust spectral features for identification of urban surface materials in hyperspectral remote sensing data. *Remote Sensing of Environment* **2007,** *111* (4), 537-552.

31. Cucci, C.; Delaney, J. K.; Picollo, M., Reflectance hyperspectral imaging for investigation of works of art: old master paintings and illuminated manuscripts. *Accounts of Chemical Research* **2016,** *49* (10), 2070-2079.

32. Kubik, M., Hyperspectral imaging: a new technique for the non-invasive study of artworks. In *Physical Techniques in the Study of Art, Archaeology and Cultural Heritage*, Elsevier: 2007; Vol. 2, pp 199-259.

33. Padoan, R.; Steemers, T. A.; Klein, M.; Aalderink, B.; De Bruin, G., Quantitative hyperspectral imaging of historical documents: technique and applications. *Art Proceedings* **2008**, 25-30.

34. Cavalli, R. M.; Colosi, F.; Palombo, A.; Pignatti, S.; Poscolieri, M., Remote hyperspectral imagery as a support to archaeological prospection. *Journal of Cultural Heritage* **2007,** *8* (3), 272-283.

35. Liang, H., Advances in multispectral and hyperspectral imaging for archaeology and art conservation. *Applied Physics A* **2012,** *106* (2), 309-323.

36. Lau, D.; Villis, C.; Furman, S.; Livett, M., Multispectral and hyperspectral image analysis of elemental and micro-Raman maps of cross-sections from a 16th century painting. *Analytica Chimica Acta* **2008,** *610* (1), 15-24.

37. Liang, H.; Lange, R.; Howard, H.; Spooner, J. In *Non-invasive investigations of a wall painting using optical coherence tomography and hyperspectral imaging*, O3A: Optics for Arts, Architecture, and Archaeology III, International Society for Optics and Photonics: 2011; p 80840F.

38. Cucci, C.; Casini, A.; Picollo, M.; Stefani, L. In *Extending hyperspectral imaging from Vis to NIR spectral regions: a novel scanner for the in-depth analysis of polychrome surfaces*, Optics for Arts, Architecture, and Archaeology IV, International Society for Optics and Photonics: 2013; p 879009.

39. Reed, G.; Savage, K.; Edwards, D.; Daeid, N. N., Hyperspectral imaging of gel pen inks: An emerging tool in document analysis. *Science and Justice* **2014,** *54* (1), 71-80.

40. Flynn, K.; O'Leary, R.; Lennard, C.; Roux, C.; Reedy, B. J., Forensic applications of infrared chemical imaging: multi-layered paint chips. *Journal of Forensic Science* **2005,** *50* (4), JFS2004502-10.

41. de la Ossa, M. Á. F.; Amigo, J. M.; García-Ruiz, C., Detection of residues from explosive manipulation by near infrared hyperspectral imaging: A promising forensic tool. *Forensic Science International* **2014,** *242*, 228-235.

42. Silva, C. S.; Pimentel, M. F.; Honorato, R. S.; Pasquini, C.; Prats-Montalbán, J. M.; Ferrer, A., Near infrared hyperspectral imaging for forensic analysis of document forgery. *Analyst* **2014,** *139* (20), 5176-5184.

43. Edelman, G.; Gaston, E.; Van Leeuwen, T.; Cullen, P.; Aalders, M., Hyperspectral imaging for non-contact analysis of forensic traces. *Forensic Science International* **2012,** *223* (1-3), 28-39.

44. Edelman, G.; van Leeuwen, T. G.; Aalders, M. C., Hyperspectral imaging for the age estimation of blood stains at the crime scene. *Forensic Science International* **2012,** *223* (1-3), 72-77.

45. Feng, Y.-Z.; Sun, D.-W., Application of hyperspectral imaging in food safety inspection and control: a review. *Critical Reviews in Food Science and Nutrition* **2012,** *52* (11), 1039-1058.

46. ElMasry, G.; Wang, N.; ElSayed, A.; Ngadi, M., Hyperspectral imaging for nondestructive determination of some quality attributes for strawberry. *Journal of Food Engineering* **2007,** *81* (1), 98-107.

47. ElMasry, G.; Sun, D.-W.; Allen, P., Near-infrared hyperspectral imaging for predicting colour, pH and tenderness of fresh beef. *Journal of Food Engineering* **2012,** *110* (1), 127-140.

48. Qin, J.; Chao, K.; Kim, M., Raman chemical imaging system for food safety and quality inspection. *Transactions of the ASABE* **2010,** *53* (6), 1873-1882.

49. Qin, J.; Chao, K.; Kim, M. S.; Lu, R.; Burks, T. F., Hyperspectral and multispectral imaging for evaluating food safety and quality. *Journal of Food Engineering* **2013,** *118* (2), 157-171.

50. Qiao, J.; Ngadi, M. O.; Wang, N.; Gariépy, C.; Prasher, S. O., Pork quality and marbling level assessment using a hyperspectral imaging system. *Journal of Food Engineering* **2007,** *83* (1), 10-16.

51. Kim, M. S.; Chen, Y.; Mehl, P., Hyperspectral reflectance and fluorescence imaging system for food quality and safety. *Transactions of the ASAE* **2001,** *44* (3), 721.

52. Mehl, P. M.; Chen, Y.-R.; Kim, M. S.; Chan, D. E., Development of hyperspectral imaging technique for the detection of apple surface defects and contaminations. *Journal of Food Engineering* **2004,** *61* (1), 67-81.

53. Rajkumar, P.; Wang, N.; EImasry, G.; Raghavan, G.; Gariepy, Y., Studies on banana fruit quality and maturity stages using hyperspectral imaging. *Journal of Food Engineering* **2012,** *108* (1), 194-200.

54. Wang, W.; Paliwal, J., Near-infrared spectroscopy and imaging in food quality and safety. *Sensing and Instrumentation for Food Quality and Safety* **2007,** *1* (4), 193-207.

55. Wu, D.; Sun, D.-W., Advanced applications of hyperspectral imaging technology for food quality and safety analysis and assessment: A review—Part I: Fundamentals. *Innovative Food Science & Emerging Technologies* **2013,** *19*, 1-14.

56. Wu, D.; Sun, D.-W., Advanced applications of hyperspectral imaging technology for food quality and safety analysis and assessment: A review—Part II: Applications. *Innovative Food Science & Emerging Technologies* **2013,** *19*, 15-28.

57. Strycker, P. D.; Chanover, N.; Voelz, D.; SimonMiller, A., Hyperspectral Imaging of Jupiter and Saturn. *Planetary Atmospheres* **2007,** *1*, 120-121.

58. Strycker, P. D.; Chanover, N.; Voelz, D.; SimonMiller, A., Jovian Ammonia Cloud Identification and Color Analyses from Hyperspectral Imaging. **2007**.

59. Yushkov, K.; Anikin, S.; Chizhikov, S.; Esipov, V.; Kolesnikov, A.; Makarov, O. Y.; Molchanov, V. Y.; Potanin, S.; Tatarnikov, A., Recent advances in acousto-optic instrumentation for astronomy. *Acta Phys. Pol. A* **2015,** *127*, 81-83.

60. Li, C.; Ingersoll, A.; Janssen, M.; Levin, S.; Bolton, S.; Adumitroaie, V.; Allison, M.; Arballo, J.; Bellotti, A.; Brown, S., The distribution of ammonia on Jupiter from a preliminary inversion of Juno Microwave Radiometer data. *Geophysical Research Letters* **2017**.

61. Montmessin, F.; Gondet, B.; Bibring, J. P.; Langevin, Y.; Drossart, P.; Forget, F.; Fouchet, T., Hyperspectral imaging of convective CO2 ice clouds in the equatorial mesosphere of Mars. *Journal of Geophysical Research: Planets* **2007,** *112* (E11).

62. Bell, J.; Wolff, M.; Noll, K.; Lubenow, A.; Noe-Dobrea, E.; Hubbard, M.; Morris, R.; Videen, G.; Shkuratov, Y. In *Hubble space telescope imaging and spectroscopy of Mars during the extremely close approach of 2003*, AGU Fall Meeting Abstracts, 2003.

63. Scholl, J. F.; Hege, E. K.; Hart, M.; O'Connell, D.; Dereniak, E. L. In *Flash hyperspectral imaging of non-stellar astronomical objects*, Mathematics of Data/Image Pattern Recognition, Compression, and Encryption with Applications XI, International Society for Optics and Photonics: 2008; p 70750H.

64. Slawson, R. W.; Ninkov, Z.; Horch, E. P., Hyperspectral Imaging: Wide-Area Spectrophotometry Using a Liquid-Crystal Tunable Filter. *Publications of the Astronomical Society of the Pacific* **1999,** *111* (759), 621.

65. Rafert, B.; Sellar, R. G.; Holbert, E.; Blatt, J. H.; Tyler, D. W.; Durham, S. E.; Newby, H. D. In *Hyperspectral imaging Fourier transform spectrometers for astronomical and remote sensing observations*, Instrumentation in Astronomy VIII, International Society for Optics and Photonics: 1994; pp 338-350.

66. Hege, E. K.; O'Connell, D.; Johnson, W.; Basty, S.; Dereniak, E. L. In *Hyperspectral imaging for astronomy and space surviellance*, Imaging Spectrometry IX, International Society for Optics and Photonics: 2004; pp 380-392.

67. Gares, K. L.; Hufziger, K. T.; Bykov, S. V.; Asher, S. A., Review of explosive detection methodologies and the emergence of standoff deep UV resonance Raman. *Journal of Raman Spectroscopy* **2016,** *47* (1), 124-141.

68. Chamberland, M.; Farley, V.; Giroux, J.; Villemaire, A.; Legault, J.-F.; Schwantes, K. R. In *Development and testing of a hyperspectral imaging instrument for standoff chemical detection*, Chemical and Biological Standoff Detection II, International Society for Optics and Photonics: 2004; pp 135-144.

69. Wentworth, R. M.; Neiss, J.; Nelson, M. P.; Treado, P. J. In *Standoff Raman hyperspectral imaging detection of explosives*, Antennas and Propagation Society International Symposium, 2007 IEEE, IEEE: 2007; pp 4925-4928.

70. Blake, T. A.; Kelly, J. F.; Gallagher, N. B.; Gassman, P. L.; Johnson, T. J., Passive standoff detection of RDX residues on metal surfaces via infrared hyperspectral imaging. *Analytical and Bioanalytical Chemistry* **2009,** *395* (2), 337-348.

71. Bernacki, B. E.; Phillips, M. C. In *Standoff hyperspectral imaging of explosives residues using broadly tunable external cavity quantum cascade laser illumination*, Chemical, Biological, Radiological, Nuclear, and Explosives (CBRNE) Sensing XI, International Society for Optics and Photonics: 2010; p 76650I.

72. Weatherbee, O.; Janaskie, J.; Hyvärinen, T. In *Advanced hyperspectral imaging solutions for near real-time target detection*, Electro-Optical Remote Sensing, Photonic Technologies, and Applications VI, International Society for Optics and Photonics: 2012; p 854223.

73. Rousset-Rouviere, L.; Coudrain, C.; Fabre, S.; Poutier, L.; Løke, T.; Fridman, A.; Blaaberg, S.; Baarstad, I.; Skauli, T.; Mocoeur, I. In *SYSIPHE system: a state of the art airborne hyperspectral imaging system: initial results from the first airborne campaign*, Electro-Optical and Infrared Systems: Technology and Applications XI, International Society for Optics and Photonics: 2014; p 92490V.

74. Renhorn, I.; Axelsson, M.; Benoist, K.; Bourghys, D.; Boucher, Y.; Briottet, X.; De Ceglie, S.; Dekker, R.; Dimmeler, A.; Dost, R. In *Detection in urban scenario using combined airborne imaging sensors*, Infrared Technology and Applications XXXVIII, International Society for Optics and Photonics: 2012; p 83530I.

75. Dupont, A., Intelligence for the twenty-first century. *Intelligence and National Security* **2003,** *18* (4), 15-39.

76. Briottet, X.; Boucher, Y.; Dimmeler, A.; Malaplate, A.; Cini, A.; Diani, M.; Bekman, H.; Schwering, P.; Skauli, T.; Kasen, I. In *Military applications of hyperspectral imagery*, Targets and Backgrounds XII: Characterization and Representation, International Society for Optics and Photonics: 2006; p 62390B.

77. Puckrin, E.; Turcotte, C. S.; Gagnon, M.-A.; Bastedo, J.; Farley, V.; Chamberland, M. In *Airborne infrared hyperspectral imager for intelligence, surveillance, and reconnaissance applications*, Airborne Intelligence, Surveillance, Reconnaissance (ISR) Systems and Applications IX, International Society for Optics and Photonics: 2012; p 836004.

78. Thompson, D. R.; Boardman, J. W.; Eastwood, M. L.; Green, R. O., A large airborne survey of Earth's visible-infrared spectral dimensionality. *Optics Express* **2017,** *25* (8), 9186-9195.

79. Green, R. O.; Eastwood, M. L.; Sarture, C. M.; Chrien, T. G.; Aronsson, M.; Chippendale, B. J.; Faust, J. A.; Pavri, B. E.; Chovit, C. J.; Solis, M., Imaging spectroscopy and the airborne visible/infrared imaging spectrometer (AVIRIS). *Remote Sensing of Environment* **1998,** *65* (3), 227-248.

80. Fuentes, D. A.; Gamon, J. A.; Cheng, Y.; Claudio, H. C.; Qiu, H.-l.; Mao, Z.; Sims, D. A.; Rahman, A. F.; Oechel, W.; Luo, H., Mapping carbon and water vapor fluxes in a chaparral ecosystem using vegetation indices derived from AVIRIS. *Remote Sensing of Environment* **2006,** *103* (3), 312-323.

81. Riaño, D.; Chuvieco, E.; Ustin, S.; Zomer, R.; Dennison, P.; Roberts, D.; Salas, J., Assessment of vegetation regeneration after fire through multitemporal analysis of AVIRIS images in the Santa Monica Mountains. *Remote Sensing of Environment* **2002,** *79* (1), 60-71.

82. Dar Roberts, M. G.; Regelbrugge, J.; Pedreros, D.; Ustin, S. In *Mapping the distribution of wildfire fuels using AVIRIS in the Santa Monica Mountains*, Summaries of the Seventh JPL Airborne Earth Science Workshop. Washington, DC: NASA, 1998; pp 345-352.

83. King, T. V.; Clark, R. N.; Ager, C.; Swayze, G. A., Remote mineral mapping using AVIRIS data at Summitville, Colorado and the adjacent San Juan Mountains. **1995**.

84. Kruse, F. *Mineral mapping for environmental hazards assessment using AVIRIS data, Leadville, Colorado, USA*; Environmental Research Institute of Michigan (ERIM), Ann Arbor, MI (United States): 1996.

85. Swayze, G.; Clark, R. N.; Kruse, F.; Sutley, S.; Gallagher, A., Ground-truthing AVIRIS mineral mapping at Cuprite, Nevada. **1992**.

86. Fingas, M.; Brown, C., Review of oil spill remote sensing. *Marine Pollution Bulletin* **2014,** *83* (1), 9-23.

87. Leifer, I.; Lehr, W. J.; Simecek-Beatty, D.; Bradley, E.; Clark, R.; Dennison, P.; Hu, Y.; Matheson, S.; Jones, C. E.; Holt, B., State of the art satellite and airborne marine oil spill remote sensing: Application to the BP Deepwater Horizon oil spill. *Remote Sensing of Environment* **2012,** *124*, 185-209.

88. McNutt, M. K.; Camilli, R.; Crone, T. J.; Guthrie, G. D.; Hsieh, P. A.; Ryerson, T. B.; Savas, O.; Shaffer, F., Review of flow rate estimates of the Deepwater Horizon oil spill. *Proceedings of the National Academy of Sciences* **2012,** *109* (50), 20260-20267.

89. Xiao, Q.; Ustin, S.; McPherson, E., Using AVIRIS data and multiple-masking techniques to map urban forest tree species. *International Journal of Remote Sensing* **2004,** *25* (24), 5637-5654.

90. Smith, M.-L.; Martin, M. E.; Plourde, L.; Ollinger, S. V., Analysis of hyperspectral data for estimation of temperate forest canopy nitrogen concentration: comparison between an airborne (AVIRIS) and a spaceborne (Hyperion) sensor. *IEEE Transactions on Geoscience and Remote Sensing* **2003,** *41* (6), 1332-1337.

91. Townsend, P. A.; Foster, J. R.; Chastain, R. A.; Currie, W. S., Application of imaging spectroscopy to mapping canopy nitrogen in the forests of the central Appalachian Mountains using Hyperion and AVIRIS. *IEEE Transactions on Geoscience and Remote Sensing* **2003,** *41* (6), 1347-1354.

92. Beeri, O.; Phillips, R.; Hendrickson, J.; Frank, A. B.; Kronberg, S., Estimating forage quantity and quality using aerial hyperspectral imagery for northern mixed-grass prairie. *Remote Sensing of Environment* **2007,** *110* (2), 216-225.

93. Asner, G. P.; Borghi, C. E.; Ojeda, R. A., Desertification in central Argentina: changes in ecosystem carbon and nitrogen from imaging spectroscopy. *Ecological Applications* **2003,** *13* (3), 629-648.

94. Martin, M. E.; Aber, J. D., High spectral resolution remote sensing of forest canopy lignin, nitrogen, and ecosystem processes. *Ecological Applications* **1997,** *7* (2), 431-443.

95. Martin, M.; Newman, S.; Aber, J.; Congalton, R., Determining forest species composition using high spectral resolution remote sensing data. *Remote Sensing of Environment* **1998,** *65* (3), 249-254.

96. Clark, M. L.; Roberts, D. A.; Ewel, J. J.; Clark, D. B., Estimation of tropical rain forest aboveground biomass with small-footprint lidar and hyperspectral sensors. *Remote Sensing of Environment* **2011,** *115* (11), 2931-2942.

97. Broge, N. H.; Leblanc, E., Comparing prediction power and stability of broadband and hyperspectral vegetation indices for estimation of green leaf area index and canopy chlorophyll density. *Remote Sensing of Environment* **2001,** *76* (2), 156-172.

98. Xavier, A. C.; Rudorff, B. F. T.; Moreira, M. A.; Alvarenga, B. S.; Freitas, J. G. d.; Salomon, M. V., Hyperspectral field reflectance measurements to estimate wheat grain yield and plant height. *Scientia Agricola* **2006,** *63* (2), 130-138.

99. Shanahan, J. F.; Schepers, J. S.; Francis, D. D.; Varvel, G. E.; Wilhelm, W. W.; Tringe, J. M.; Schlemmer, M. R.; Major, D. J., Use of remote-sensing imagery to estimate corn grain yield. *Agronomy Journal* **2001,** *93* (3), 583-589.

100. Haboudane, D.; Tremblay, N.; Miller, J. R.; Vigneault, P., Remote estimation of crop chlorophyll content using spectral indices derived from hyperspectral data. *IEEE Transactions on Geoscience and Remote Sensing* **2008,** *46* (2), 423-437.

101. Galvão, L. S.; Formaggio, A. R.; Couto, E. G.; Roberts, D. A., Relationships between the mineralogical and chemical composition of tropical soils and topography from hyperspectral remote sensing data. *ISPRS Journal of Photogrammetry and Remote Sensing* **2008,** *63* (2), 259-271.

102. Goel, P. K.; Prasher, S. O.; Landry, J. A.; Patel, R. M.; Viau, A. A.; Miller, J. R., Estimation of crop biophysical parameters through airborne and field hyperspectral remote sensing. *Transactions of the ASAE* **2003,** *46* (4), 1235.

103. Yuen, P. W.; Richardson, M., An introduction to hyperspectral imaging and its application for security, surveillance and target acquisition. *The Imaging Science Journal* **2010,** *58* (5), 241-253.

104. Hagen, N.; Kester, R. T.; Morlier, C. G.; Panek, J. A.; Drayton, P.; Fashimpaur, D.; Stone, P.; Adams, E. In *Video-rate spectral imaging of gas leaks in the longwave infrared*, Chemical, Biological, Radiological, Nuclear, and Explosives (CBRNE) Sensing XIV, International Society for Optics and Photonics: 2013; p 871005.

105. Samson, E.; Blanca, C.; Saloma, C., Near-IR Spectral Imaging of Semiconductor Absorption Sites in Integrated Circuits. *Science Diliman* **2007,** *16* (2),101-105.

106. Porat, R.; Dotan, K.; Hemar, S.; Levin, L.; Li, K.; Sung, G.; Lin, C.-T.; Lin, S.-K.; Wang, H.-I. In *SEM-based methodology for root cause analysis of wafer edge and bevel defects*, Advanced Semiconductor Manufacturing Conference, 2008. ASMC 2008. IEEE/SEMI, IEEE: 2008; pp 11-14.

107. Hattori, T., Detection and identification of particles on silicon surfaces. *Particles on Surfaces, Detection, Adhesion, and Removal, Edited by KL Mittal, Marcel Dekker, Inc., New York* **1995**, 201.

108. Laskin, A.; Cowin, J. P., Automated single-particle SEM/EDX analysis of submicrometer particles down to 0.1 μm. *Analytical Chemistry* **2001,** *73* (5), 1023-1029.

109. Takada, N.; Kamata, T., Spectral imaging for electroluminescence characterization of a polymer-blend light-emitting diode. *Japanese Journal of Applied Physics* **2005,** *44* (12R), 8670.

110. Bobba, V. N. K. R. High Fidelity Raman Chemical Imaging of Materials. Cleveland State University, 2016.

111. Kruse, F., Identification and mapping of minerals in drill core using hyperspectral image analysis of infrared reflectance spectra. *International Journal of Remote Sensing* **1996,** *17* (9), 1623-1632.

112. Moghaddam, T. M.; Razavi, S. M.; Taghizadeh, M., Applications of hyperspectral imaging in grains and nuts quality and safety assessment: a review. *Journal of Food Measurement and Characterization* **2013,** *7* (3), 129-140.

113. Monteiro, S. T.; Minekawa, Y.; Kosugi, Y.; Akazawa, T.; Oda, K., Prediction of sweetness and amino acid content in soybean crops from hyperspectral imagery. *ISPRS Journal of Photogrammetry and Remote Sensing* **2007,** *62* (1), 2-12.

114. Gowen, A. A.; Taghizadeh, M.; O'Donnell, C. P., Identification of mushrooms subjected to freeze damage using hyperspectral imaging. *Journal of Food Engineering* **2009,** *93* (1), 7-12.

115. Iqbal, S. M.; Gopal, A. In *Automated quality inspection of citrus fruits–a review*, Proceedings of the 2014 ICAM International Conference on Advanced and Agile Manufacturing. Held at Oakland University, Rochester, MI, 2014; pp 1-17.

116. Pu, Y.-Y.; Feng, Y.-Z.; Sun, D.-W., Recent progress of hyperspectral imaging on quality and safety inspection of fruits and vegetables: a review. *Comprehensive Reviews in Food Science and Food Safety* **2015,** *14* (2), 176-188.

117. Kamruzzaman, M.; ElMasry, G.; Sun, D.-W.; Allen, P., Application of NIR hyperspectral imaging for discrimination of lamb muscles. *Journal of Food Engineering* **2011,** *104* (3), 332-340.

118. Kamruzzaman, M.; ElMasry, G.; Sun, D.-W.; Allen, P., Non-destructive prediction and visualization of chemical composition in lamb meat using NIR hyperspectral imaging and multivariate regression. *Innovative Food Science & Emerging Technologies* **2012,** *16*, 218-226.

119. Kamruzzaman, M.; ElMasry, G.; Sun, D.-W.; Allen, P., Non-destructive assessment of instrumental and sensory tenderness of lamb meat using NIR hyperspectral imaging. *Food Chemistry* **2013,** *141* (1), 389-396.

120. Menesatti, P.; Costa, C.; Aguzzi, J., Quality evaluation of fish by hyperspectral imaging. In *Hyperspectral Imaging for Food Quality Analysis and Control*, Elsevier: 2010; pp 273-294.

121. Cheng, J.-H.; Sun, D.-W., Rapid and non-invasive detection of fish microbial spoilage by visible and near infrared hyperspectral imaging and multivariate analysis. *LWT-Food Science and Technology* **2015,** *62* (2), 1060-1068.

122. Zhu, F.; Zhang, D.; He, Y.; Liu, F.; Sun, D.-W., Application of visible and near infrared hyperspectral imaging to differentiate between fresh and frozen–thawed fish fillets. *Food and Bioprocess Technology* **2013,** *6* (10), 2931-2937.

123. Roggo, Y.; Edmond, A.; Chalus, P.; Ulmschneider, M., Infrared hyperspectral imaging for qualitative analysis of pharmaceutical solid forms. *Analytica Chimica Acta* **2005,** *535* (1-2), 79-87.

124. Hamilton, S. J.; Lodder, R. A. In *Hyperspectral imaging technology for pharmaceutical analysis*, Biomedical Nanotechnology Architectures and Applications, International Society for Optics and Photonics: 2002; pp 136-148.

125. Malik, I.; Poonacha, M.; Moses, J.; Lodder, R. A., Multispectral imaging of tablets in blister packaging. *AAPS PharmSciTech* **2001,** *2* (2), 38-44.

126. Gioux, S.; Choi, H. S.; Frangioni, J. V., Image-guided surgery using invisible near-infrared light: fundamentals of clinical translation. *Molecular Imaging* **2010,** *9* (5), 7290.2010. 00034.

127. Gotoh, K.; Yamada, T.; Ishikawa, O.; Takahashi, H.; Eguchi, H.; Yano, M.; Ohigashi, H.; Tomita, Y.; Miyamoto, Y.; Imaoka, S., A novel image-guided

surgery of hepatocellular carcinoma by indocyanine green fluorescence imaging navigation. *Journal of Surgical Oncology* **2009,** *100* (1), 75-79.

128. Schaafsma, B. E.; Mieog, J. S. D.; Hutteman, M.; Van der Vorst, J. R.; Kuppen, P. J.; Löwik, C. W.; Frangioni, J. V.; Van de Velde, C. J.; Vahrmeijer, A. L., The clinical use of indocyanine green as a near-infrared fluorescent contrast agent for image-guided oncologic surgery. *Journal of Surgical Oncology* **2011,** *104* (3), 323-332.

129. Keereweer, S.; Van Driel, P. B.; Snoeks, T. J.; Kerrebijn, J. D.; de Jong, R. J. B.; Vahrmeijer, A. L.; Sterenborg, H. J.; Löwik, C. W., Optical image-guided cancer surgery: challenges and limitations. *Clinical Cancer Research* **2013,** *19* (14), 3745-3754.

130. Boppart, S. A.; Luo, W.; Marks, D. L.; Singletary, K. W., Optical coherence tomography: feasibility for basic research and image-guided surgery of breast cancer. *Breast Cancer Research and Treatment* **2004,** *84* (2), 85-97.

131. Vahrmeijer, A. L.; Hutteman, M.; Van Der Vorst, J. R.; Van De Velde, C. J.; Frangioni, J. V., Image-guided cancer surgery using near-infrared fluorescence. *Nature Reviews Clinical Oncology* **2013,** *10* (9), 507.

132. Lu, G.; Fei, B., Medical hyperspectral imaging: a review. *Journal of Biomedical Optics* **2014,** *19* (1), 010901-010901.

133. Johnson, W. R.; Wilson, D. W.; Fink, W.; Humayun, M. S.; Bearman, G. H., Snapshot hyperspectral imaging in ophthalmology. *Journal of Biomedical Optics* **2007,** *12* (1), 014036.

134. Srinivasan, S.; Pogue, B. W.; Jiang, S.; Dehghani, H.; Kogel, C.; Soho, S.; Gibson, J. J.; Tosteson, T. D.; Poplack, S. P.; Paulsen, K. D., Interpreting hemoglobin and water concentration, oxygen saturation, and scattering measured

in vivo by near-infrared breast tomography. *Proceedings of the National Academy of Sciences* **2003,** *100* (21), 12349-12354.

135. Cancio, L. C.; Batchinsky, A. I.; Mansfield, J. R.; Panasyuk, S.; Hetz, K.; Martini, D.; Jordan, B. S.; Tracey, B.; Freeman, J. E., Hyperspectral imaging: a new approach to the diagnosis of hemorrhagic shock. *Journal of Trauma and Acute Care Surgery* **2006,** *60* (5), 1087-1095.

136. Chin, J. A.; Wang, E. C.; Kibbe, M. R., Evaluation of hyperspectral technology for assessing the presence and severity of peripheral artery disease. *Journal of Vascular Surgery* **2011,** *54* (6), 1679-1688.

137. Usenik, P.; Bürmen, M.; Fidler, A.; Pernuš, F.; Likar, B. In *Evaluation of cross-polarized near infrared hyperspectral imaging for early detection of dental caries*, Lasers in Dentistry XVIII, International Society for Optics and Photonics: 2012; p 82080G.

138. Blanco, F.; López-Mesas, M.; Valiente, M.; Serranti, S.; Bonifazi, G.; Havel, J., Hyperspectral imaging based method for fast characterization of kidney stone types. *Journal of Biomedical Optics* **2012,** *17* (7), 076027.

139. Martin, R.; Thies, B.; Gerstner, A. O., Hyperspectral hybrid method classification for detecting altered mucosa of the human larynx. *International Journal of Health Geographics* **2012,** *11* (1), 21.

140. Akbari, H.; Kosugi, Y.; Kojima, K.; Tanaka, N. In *Hyperspectral imaging and diagnosis of intestinal ischemia*, Engineering in Medicine and Biology Society, 2008. EMBS 2008. 30th Annual International Conference of the IEEE, IEEE: 2008; pp 1238-1241.

141. Akbari, H.; Kosugi, Y.; Kojima, K.; Tanaka, N. In *Blood vessel detection and artery-vein differentiation using hyperspectral imaging*, Engineering in Medicine

and Biology Society, 2009. EMBC 2009. Annual International Conference of the IEEE, IEEE: 2009; pp 1461-1464.

142. Best, S. L.; Thapa, A.; Holzer, M. S.; Jackson, N.; Mir, S. A.; Donnally, C. J.; Wehner, E.; Raj, G. V.; Livingston, E.; Cadeddu, J. A. In *Assessment of renal oxygenation during partial nephrectomy using DLP hyperspectral imaging*, Emerging Digital Micromirror Device Based Systems and Applications III, International Society for Optics and Photonics: 2011; p 793202.

143. Holzer, M. S.; Best, S. L.; Jackson, N.; Thapa, A.; Raj, G. V.; Cadeddu, J. A.; Zuzak, K. J., Assessment of renal oxygenation during partial nephrectomy using hyperspectral imaging. *The Journal of Urology* **2011,** *186* (2), 400-404.

144. Niehörster, T.; Löschberger, A.; Gregor, I.; Krämer, B.; Rahn, H.-J.; Patting, M.; Koberling, F.; Enderlein, J.; Sauer, M., Multi-target spectrally resolved fluorescence lifetime imaging microscopy. *Nature Methods* **2016,** *13* (3), 257.

145. Chernenko, T.; Matthäus, C.; Milane, L.; Quintero, L.; Amiji, M.; Diem, M., Label-free Raman spectral imaging of intracellular delivery and degradation of polymeric nanoparticle systems. *ACS Nano* **2009,** *3* (11), 3552-3559.

146. Nallala, J.; Piot, O.; Diebold, M.-D.; Gobinet, C.; Bouché, O.; Manfait, M.; Sockalingum, G. D., Infrared and Raman imaging for characterizing complex biological materials: a comparative morpho-spectroscopic study of colon tissue. *Applied Spectroscopy* **2014,** *68* (1), 57-68.

147. Gao, L.; Kester, R. T.; Hagen, N.; Tkaczyk, T. S., Snapshot image mapping spectrometer (IMS) with high sampling density for hyperspectral microscopy. *Optics Express* **2010,** *18* (14), 14330-14344.

148. Golub, M. A.; Nathan, M.; Averbuch, A.; Lavi, E.; Zheludev, V. A.; Schclar, A., Spectral multiplexing method for digital snapshot spectral imaging. *Applied Optics* **2009,** *48* (8), 1520-1526.

149. Morampudi, R. Development of A High Resolution Wavelength Filter and A Spatially Multiplexed Raman Imaging System. Cleveland State University, 2014.

150. Schaeberle, M. D.; John F. Turner, I. I.; Treado, P. J. In *Multiplexed acousto-optic tunable filter (AOTF) spectral imaging microscopy*, IS$\&$T/SPIE 1994 International Symposium on Electronic Imaging: Science and Technology, International Society for Optics and Photonics: 1994; pp 11-20.

151. Schaeberle, M. D.; Morris, H. R.; John F. Turner, I. I.; Treado, P. J., Peer reviewed: Raman chemical imaging spectroscopy. *Analytical Chemistry* **1999,** *71* (5), 175A-181A.

152. Turner, J. F.; Treado, P. J., Near-infrared acousto-optic tunable filter Hadamard transform spectroscopy. *Applied Spectroscopy* **1996,** *50* (2), 277-284.

153. Wachman, E. S.; Niu, W.-h.; Farkas, D. L., Imaging acousto-optic tunable filter with 0.35-micrometer spatial resolution. *Applied Optics.* **1996,** *35* (25), 5220-5226.

154. Wachman, E. S.; Niu, W.; Farkas, D. L., AOTF microscope for imaging with increased speed and spectral versatility. *Biophys.J.* **1997,** *73* (3), 1215-1222.

155. Gupta, N.; Dahmani, R.; Choy, S. J., Acousto-optic tunable filter-based visible-to-near-infrared spectroploarimetric imager. *Optical Engineering* **2002,** *41* (5), 1033-1039.

156. Indebetouw, G., Tunable spatial filtering with a Fabry-Perot etalon. *Applied Optics* **1980,** *19* (5), 761-764.

157. Neumann, N.; Ebermann, M.; Kurth, S.; Hiller, K., Tunable infrared detector with integrated micromachined Fabry-Perot filter. *Journal of Micro/Nanolithography, MEMS, and MOEMS* **2008,** *7* (2), 021004.

158. Atherton, P.; Reay, N. K.; Ring, J.; Hicks, T., Tunable fabry-perot filters. *Optical Engineering* **1981,** *20* (6), 206806.

159. Miller, P. J.; Hoyt, C. C. In *Multispectral imaging with a liquid crystal tunable filter*, Optics in Agriculture, Forestry, and Biological Processing, International Society for Optics and Photonics: 1995; pp 354-366.

160. Morris, H. R.; Hoyt, C. C.; Miller, P.; Treado, P. J., Liquid crystal tunable filter Raman chemical imaging. *Applied Spectroscopy* **1996,** *50* (6), 805-811.

161. Gebhart, S. C.; Thompson, R. C.; Mahadevan-Jansen, A., Liquid-crystal tunable filter spectral imaging for brain tumor demarcation. *Applied Optics* **2007,** *46* (10), 1896-1910.

162. Hardeberg, J. Y.; Schmitt, F. J.; Brettel, H., Multispectral color image capture using a liquid crystal tunable filter. *Optical Engineering* **2002,** *41* (10), 2532-2549.

163. Winefordner, J. D.; Matveev, O. I.; Smith, B. W., High resolution resonance ionization imaging detector and method. Google Patents: 1999.

164. Wilkinson, T. D.; Butt, H.; Montelongo, Y., Holographic Liquid Crystals for Nanophotonics. In *Nanoscience with Liquid Crystals*, Springer: 2014; pp 1-34.

165. Schaeberle, M. D.; Turner II, J. F.; Treado, P. J. In *Multiplexed acousto-optic tunable filter (AOTF) spectral imaging microscopy*, IS&T SPIE 1994 International Symposium on Electronic Imaging: Science and Technology, 1994; pp 11-20.

166. Storey, A. P.; Ray, S. J.; Hoffmann, V.; Voronov, M.; Engelhard, C.; Buscher, W.; Hieftje, G. M., Wavelength Scanning with a Tilting Interference Filter for Glow-Discharge Elemental Imaging. *Applied Spectroscopy* **2017,** *71* (6), 1280-1288.

167. Hashimoto, M.; Kawata, S., Multichannel Fourier-transform infrared spectrometer. *Applied Optics* **1992,** *31* (28), 6096-6101.

168. Lewis, E. N.; Treado, P. J.; Reeder, R. C.; Story, G. M.; Dowrey, A. E.; Marcott, C.; Levin, I. W., Fourier transform spectroscopic imaging using an infrared focal-plane array detector. *Analytical Chemistry* **1995,** *67* (19), 3377-3381.

169. Marx, B.; Czerwinski, L.; Light, R.; Somekh, M.; Gilch, P., Multichannel detectors for femtosecond stimulated Raman microscopy–ideal and real ones. *Journal of Raman Spectroscopy* **2014,** *45* (7), 521-527.

170. Fell, A. F.; Clark, B. J.; Scott, H. P., Novel applications of multichannel spectroscopy in pharmaceutical analysis. *Journal of Pharmaceutical and Biomedical Analysis* **1983,** *1* (4), 557-572.

171. Deverse, R. A., Multiplexed hyperspectral imaging and spectrometry using spatial light modulators. **1999**.

172. Schlücker, S.; Schaeberle, M. D.; Huffman, S. W.; Levin, I. W., Raman microspectroscopy: a comparison of point, line, and wide-field imaging methodologies. *Analytical Chemistry* **2003,** *75* (16), 4312-4318.

173. Sun, B.; Edgar, M. P.; Bowman, R.; Vittert, L. E.; Welsh, S.; Bowman, A.; Padgett, M. J., 3D computational imaging with single-pixel detectors. *Science (New York, N.Y.)* **2013,** *340* (6134), 844-847.

174. Otto, A., Excitation of nonradiative surface plasma waves in silver by the method of frustrated total reflection. *Zeitschrift für Physik* **1968,** *216* (4), 398-410.

175. Raether, H., *Surface plasmons on smooth surfaces*. Springer: 1988.

176. Kretschmann, E., Determination of optical constants of metals by excitation of surface plasmons. *Zeitschrift Fur Physik* **1971,** *241* (4), 313.

177. Kretschmann, E., Die bestimmung optischer konstanten von metallen durch anregung von oberflächenplasmaschwingungen. *Zeitschrift für Physik* **1971,** *241* (4), 313-324.

178. Ingle Jr, J. D.; Crouch, S. R., Spectrochemical analysis. **1988**.

179. Kretschmann, E.; Raether, H., Notizen: radiative decay of non radiative surface plasmons excited by light. *Zeitschrift für Naturforschung A* **1968,** *23* (12), 2135-2136.

180. Barchiesi, D.; Otto, A., Excitations of surface plasmon polaritons by attenuated total reflection, revisited. *Riv.Nuovo Cimento* **2013,** *36*, 173-209.

181. Nash, D. J.; Sambles, J. R., Surface plasmon-polariton study of the optical dielectric function of silver. *Journal of Modern Optics* **1996,** *43* (1), 81-91.

182. Weber, M. J., *Handbook of optical materials*. CRC press: 2002; Vol. 19.

183. Novotny, L.; Hecht, B., *Principles of Nano-Optics*. Cambridge university press: 2012.

184. Dever, J. A.; Rutledge, S. K.; Hambourger, P. D.; Bruckner, E.; Ferrante, R.; Pal, A. M.; Mayer, K.; Pietromica, A. J. In *Indium Tin Oxide-Magnesium Fluoride Co-Deposited Films for Spacecraft Applications*, American Vacuum Society: 1998.

185. Ersoy, M.; Hambourger, P. D., Ti-B-N and Ti-B-O Scratch Resistant Weakly Conductive Transparent Coatings for Aerospace Applications. *SVC 51st Annual Technical Conference Proceedings* **2008**, 475-475-477.

186. Welford, K. R.; Sambles, J. R., Coupled surface plasmons in a symmetric system. *Journal of Modern Optics* **1988,** *35* (9), 1467-1483.

187. Turner, J. F., 2nd; Zhang, J.; O'Connor, A., A spectral identity mapper for chemical image analysis. *Appllied Spectroscopy.* **2004,** *58* (11), 1308-1317.

188. Turner, I.; John, F. In *Spectral identity mapping for enhanced chemical image analysis*, Proceedings. of SPIE Vol, 2005; p 25.

189. Berini, P., Long-range surface plasmon polaritons. *Advances in Optics and Photonics* **2009,** *1* (3), 484-588.

190. Sarid, D., Long-range surface-plasma waves on very thin metal films. *Physical Review Letters* **1981,** *47* (26), 1927.

191. Sarid, D.; Deck, R. T.; Craig, A. E.; Hickernell, R. K.; Jameson, R. S.; Fasano, J. J., Optical field enhancement by long-range surface-plasma waves. *Applied Optics* **1982,** *21* (22), 3993-3995.

APPENDIX A

In order to model the transmittance as a function of wavelength in the SPCTF, it is necessary to employ Maxwell's equations of electromagnetism. In particular, the divergence and curl of the electric field which are given by

$$\nabla \cdot \vec{E} = 0$$

and

$$\nabla \times \vec{E} = -\mu \frac{\partial \vec{H}}{\partial t} = -\frac{\partial \vec{B}}{\partial t} \quad .$$

The SPCTF geometry is similar to the Kretschmann-Raether geometry employed for surface plasmon resonance spectroscopy (SPR) and is illustrated in Figure. 4. Only the π-polarized component generates a strong plasmon coupling at Brewster's angles above the critical angle. Consequently, a polarizer must be placed in the optical path prior to the SPCTF. It is important to note that the successful conversion between a photon and a surface plasmon requires a negative permittivity, the absolute value of which is larger than that of the dielectric. Metals such as gold and silver meet this requirement and have large negative permittivities. The permittivity of metals have both real and imaginary parts; the imaginary part is the result of damping. Described below is a fully theoretical description of surface plasmon condition in a semi-infinite system, explained by Maxwell's equation and classical electromagnetic theory. For notations, refer to Figure 7.

Given:

$$E_g = \left(E_{x_g}, 0, E_{z_g}\right) e^{-i\left(k_x x + k_{z_g} z - \omega t\right)} \quad (1)$$

$$H_g = \left(0, H_{g_g}, 0\right) e^{-i\left(k_x x + k_{z_g} z - \omega t\right)} \quad (2)$$

$$E_m = \left(E_{x_m}, 0, E_{z_m}\right) e^{-i\left(k_x x + k_{z_m} z - \omega t\right)} \quad (3)$$

$$H_m = \left(0, H_{g_m}, 0\right) e^{-i\left(k_x x + k_{z_g} z - \omega t\right)} \quad (4)$$

Vector representation,

$$\overrightarrow{E_g} = E_{x_g} e^{-i\left(k_x x + k_{z_g} z - \omega t\right)} \hat{x} + 0\,\hat{y} + E_{z_g} e^{-i\left(k_x x + k_{z_g} z - \omega t\right)} \hat{z} \quad (5)$$

From Maxwell's equation, The divergence of , $\nabla \cdot \vec{E} = 0$, or

$$\left(\frac{\partial}{\partial x} + \frac{\partial}{\partial y} + \frac{\partial}{\partial z}\right) \cdot \vec{E} = 0 \quad (6)$$

and

$$\nabla \cdot \overrightarrow{E_g} = \frac{\partial \overrightarrow{E_g}}{\partial x} + \frac{\partial \overrightarrow{E_g}}{\partial y} + \frac{\partial \overrightarrow{E_g}}{\partial z} = 0 \quad (7)$$

substituting Eq. 1-4:

$$E_{x_g} e^{-i\left(k_x x + k_{z_g} z - \omega t\right)} i k_x + 0 + E_{z_g} e^{-i\left(k_x x + k_{z_g} z - \omega t\right)} i k_{z_g} = 0 \quad (8)$$

Solving for E_{z_g}:

$$E_{z_g} k_{z_g} = -E_{x_g} k_x \quad (9)$$

$$E_{z_g} = -E_{x_g} \left(\frac{k_x}{k_{z_g}}\right) \quad (10)$$

For the metal E_{z_m} can be derived same way:

$$E_{z_m} = -E_{x_m} \left(\frac{k_x}{k_{z_m}}\right) \quad (11)$$

At this point the relationship between the x and z components of the electric field in the glass and the metal have been established, where k_x is a boundary condition.

So, solving Eq. 10 for k_x:

$$k_x = -\left(\frac{E_{z_g}}{E_{x_g}}\right) k_{z_g} \tag{12}$$

and solving Eq. 11 for k_x:

$$k_x = -\left(\frac{E_{z_m}}{E_{x_m}}\right) k_{z_m}. \tag{13}$$

Therefore,

$$-\left(\frac{E_{z_g}}{E_{x_g}}\right) k_{z_g} = -\left(\frac{E_{z_m}}{E_{x_m}}\right) k_{z_m}. \tag{14}$$

At the interface $E_{x_g} = E_{x_m}$, So:

$$E_{z_g} k_{z_g} = E_{z_m} k_{z_m} . \tag{15}$$

From the Faraday's law of electromagnetic induction, the curl of $E, \nabla \times \vec{E}$ is:

$$\nabla \times \vec{E} = -\mu \frac{\partial \vec{H}}{\partial t} = -\frac{\partial \vec{B}}{\partial t} \tag{16}$$

or

$$\nabla \times \vec{E} = \begin{vmatrix} \hat{\imath} & \hat{\jmath} & \hat{k} \\ \frac{\partial}{\partial x} & \frac{\partial}{\partial y} & \frac{\partial}{\partial z} \\ E_x & E_y & E_z \end{vmatrix} \tag{17}$$

where,$\hat{\imath}$, $\hat{\jmath}$ and $\hat{k}$ are unit vectors along x, y and z axis respectively.

Hence,

$$\nabla \times \vec{E} = \left(\frac{\partial E_z}{\partial y} - \frac{\partial E_y}{\partial z}\right)\hat{\imath} - \left(\frac{\partial E_z}{\partial x} - \frac{\partial E_x}{\partial z}\right)\hat{\jmath} + \left(\frac{\partial E_y}{\partial x} - \frac{\partial E_x}{\partial y}\right)\hat{k} \quad , \tag{18}$$

$$\nabla \times \vec{E} = 0 - \left(E_{z_g} e^{i\left(k_x x + k_{z_g} z - \omega t\right)} i k_x - E_{x_g} e^{i\left(k_x x + k_{z_g} z - \omega t\right)} i k_{z_g}\right)\hat{\jmath} + 0, \tag{19}$$

And

$$\nabla \times \vec{E} = -\left(E_{z_g} k_x - E_{x_g} k_{z_g}\right)\left(i\, e^{i\left(k_x x + k_{z_g} z - \omega t\right)}\right) = -\mu_g \frac{\partial H_g}{\partial t} . \tag{20}$$

Solving for $\frac{\partial H_g}{\partial t}$:

$$\frac{\partial H_g}{\partial t} = \left(E_{z_g} k_x - E_{x_g} k_{z_g}\right)\left(\frac{i\, e^{i\left(k_x x + k_{z_g} z - \omega t\right)}}{\mu_g}\right) \tag{21}$$

and $$H_g = \int \frac{\partial H_g}{\partial t}\, \partial t \ , \tag{22}$$

$$H_g = \frac{E_{z_g} k_x\, i - E_{x_g} k_{z_g} i}{\mu_g} \int e^{i\left(k_x x + k_{z_g} z - \omega t\right)} \partial t \ , \tag{23}$$

and $$H_g = \left(\frac{E_{z_g} k_x\, i - E_{x_g} k_{z_g} i}{\mu_g}\right) \frac{e^{i\left(k_x x + k_{z_g} z - \omega t\right)}}{-\omega} + \ constant. \tag{24}$$

From Eq. 10; $E_{z_g} = -E_{x_g}\left(\frac{k_x}{k_{z_g}}\right)$ and

$$H_g = \left(\frac{E_{x_g} {k_x}^2\, i + E_{x_g} {k_{z_g}}^2 i}{k_{z_g} \mu_g \omega}\right) e^{i\left(k_x x + k_{z_g} z - \omega t\right)} \tag{25}$$

where μ_g is the permeability of glass;

in a vacuum $$\sqrt{\mu_o \mathcal{E}_o} = \frac{1}{c_o} \tag{26}$$

and $$c_o = \frac{\omega}{k_o} \quad , \tag{27}$$

$$\mu_o = \frac{{k_o}^2}{\mathcal{E}_o \omega^2} \ . \tag{28}$$

hence, $$\mu_g = \frac{{k_g}^2}{\mathcal{E}_o \mathcal{E}_g \omega^2} = \frac{{k_g}^2}{\mathcal{E}_g \omega^2} \ . \tag{29}$$

From Eq. 25 and 29

$$H_g = \left(\frac{E_{x_g} i\, \mathcal{E}_g \omega}{k_{z_g}}\right) e^{i\left(k_x x + k_{z_g} z - \omega t\right)} \ . \tag{30}$$

Similarly, for the metal:

$$H_m = \left(\frac{E_{x_m} i\, \varepsilon_m \omega}{k_{z_m}}\right) e^{i\left(k_x x + k_{z_g} z - \omega t\right)} \quad . \tag{31}$$

At the boundary between the glass and metal, $H_g = H_m$ or:

$$\left(\frac{E_{x_g} i\, \varepsilon_g \omega}{k_{z_g}}\right) e^{i\left(k_x x + k_{z_g} z - \omega t\right)} = \left(\frac{E_{x_m} i\, \varepsilon_m \omega}{k_{z_m}}\right) e^{i\left(k_x x + k_{z_g} z - \omega t\right)} \tag{32}$$

or
$$\frac{E_{x_g}\, \varepsilon_g}{k_{z_g}} = \frac{E_{x_m}\, \varepsilon_m}{k_{z_m}} \, . \tag{33}$$

From $E_{x_g} = E_{x_m}$:

$$\frac{\varepsilon_g}{k_{z_g}} = \frac{\varepsilon_m}{k_{z_m}} \tag{34}$$

But it is known that ${k_g}^2 = {k_x}^2 + {k_{z_g}}^2$, where ${k_g}^2 = \varepsilon_g {k_o}^2$. (35)

likewise, ${k_m}^2 = {k_x}^2 + {k_{z_m}}^2$,where ${k_m}^2 = \varepsilon_m {k_o}^2$. (36)

So, Eq. 34 becomes:

$$\frac{{\varepsilon_g}^2}{\varepsilon_g {k_o}^2 - {k_x}^2} = \frac{{\varepsilon_m}^2}{\varepsilon_m {k_o}^2 - {k_x}^2} \quad . \tag{37}$$

Solving for ${k_x}^2$,

$${k_x}^2 \left(\frac{1}{{\varepsilon_m}^2} - \frac{1}{{\varepsilon_g}^2}\right) = {k_o}^2 \left(\frac{1}{\varepsilon_m} - \frac{1}{\varepsilon_g}\right). \tag{38}$$

and
$$k_x = k_o \left(\frac{\varepsilon_g \varepsilon_m}{\varepsilon_g + \varepsilon_m}\right)^{1/2} \quad . \tag{39}$$

Yet, $\mathcal{E}_m = \mathcal{E}_{m_{real}} + \mathcal{E}_{m_{imaginary}}$ such that:

$$k_x = k_o \left(\frac{\mathcal{E}_g \left(\mathcal{E}_{m_{real}} + \mathcal{E}_{m_{imaginary}} \right)}{\mathcal{E}_g + \mathcal{E}_{m_{real}} + \mathcal{E}_{m_{imaginary}}} \right)^{1/2}. \tag{40}$$

From $k_0 = \frac{\omega}{c_o}$, and solving for $\omega = \omega\,(k_x)$, the dispersion relation becomes:

$$\omega = k_x c_o \left(\frac{\mathcal{E}_g + \mathcal{E}_m}{\mathcal{E}_g \mathcal{E}_m} \right). \tag{41}$$

At very high frequencies $\omega\tau \gg 1$, where τ is the electron scatter time, the bound electrons are too slow to respond so $\varepsilon_{\text{real}} \sim 1$ and $\sigma = i\frac{\sigma_o}{\omega\tau}$, where σ_o is the Drude conductivity at $\omega = 0$.

The inertia of mobile electrons makes the conductivity purely imaginary at high frequencies than $\omega = 0$, but not above plasma frequency ω_p. Thus,

$$\varepsilon^* = 1 - \frac{\sigma_o}{\varepsilon_o \omega^2 \tau} = 1 - \left(\frac{\omega_p}{\omega} \right)^2 \tag{42}$$

where, $\omega_p = \left(\frac{4\pi n e^2}{m} \right)^{1/2}$ is the plasma frequency. Here, n is the electron density and m is the electron mass.

From Eq. 41 and Eq. 42

$$\omega = k_x c_o \left(\frac{\mathcal{E}_g + 1 - \left(\frac{\omega_p}{\omega} \right)^2}{\mathcal{E}_g \left(1 - \left(\frac{\omega_p}{\omega} \right)^2 \right)} \right)^{1/2} \tag{43}$$

where $k_x = \frac{2\pi}{\Lambda_x}$, here $\Lambda_x$is wavelength of the plasmons.

If the $\vec{E}$ in the z direction (in metal) is $\vec{E}_z \approx e^{-|k_z|z}$

The value of the characteristic length (skin depth) $\hat{z}$, at which the field is reduced by a factor, $\frac{1}{e}$ is $\hat{Z} = \frac{1}{|k_z|}$

At $z = 0,\ E_z = 1$. So now find the z value such that $E_z = \frac{1}{e}1 = \frac{1}{e}$.

The skin depth ($\hat{z}$) becomes $e^{-|k_z|z} = \frac{1}{e}$. (44)

Solving for z , $$1\left(\frac{1}{e}\right) = e^{-|k_z|z} \tag{45}$$

$$\frac{1}{e} = \frac{1}{e^{|k_z|z}} \tag{46}$$

$$e^{(-1+|k_z|z)} = 1 \tag{47}$$

$$|k_z|z - 1 = \ln 1 \tag{48}$$

$$|k_z|z = 1 \tag{49}$$

$$z = \hat{Z} = \frac{1}{|k_z|} \tag{50}$$

substituting $k_m{}^2 = k_x{}^2 + k_{z_m}{}^2$ in Eq. 36 and Eq. 39:

$$k_{z_m}{}^2 = \mathcal{E}_m k_o{}^2 - k_o{}^2\left(\frac{\mathcal{E}_g\mathcal{E}_m}{\mathcal{E}_g+\mathcal{E}_m}\right) \tag{51}$$

or $$\frac{1}{k_{z_m}} = \frac{1}{k_o}\left(\frac{\mathcal{E}_g+\mathcal{E}_m}{\mathcal{E}_m{}^2}\right)^{1/2} \tag{52}$$

where, $\frac{1}{k_{z_m}} = z$ or (skin depth) and $k_o = \frac{2\pi}{\lambda_o}$.

Hence, $$\hat{Z} = \frac{\lambda_o}{2\pi}\left(\frac{\mathcal{E}_g+\mathcal{E}_m}{\mathcal{E}_m{}^2}\right)^{1/2} \tag{53}$$

APPENDIX B

Attached here is the code written in MATLAB to calculate the reflectance for glass-metal-air interface in the Kretschmann-Raether configuration using Eq 9 which is as described in section 2.4. The *sp_reflectance* function was employed to model the reflectance as a function of wavelength and incident angle in section 3.2.1.

```
function [R]=sp_reflectance(iwave,IncidentAngle,metal,thickness)
%
% The  sp_reflectance function calculates the reflectance for glass-metal-air...
% interface of the Kretchman-Raether configuration
%
% Input variables:
% iwave = range* of wavelengths in nm
% IncidentAngle = range** of incident angles onto hypotenuse in degrees
% metal = 'silver' or 'gold' as a string
% thickness = thickness of metal film in nm
%
% Usage Example:
%       R = sp_reflectance(400:1:900,42.8,'silver',48)
%  or
%       R = sp_reflectance(650,35:0.1:55,'silver',48)
%
%  *  only use one incident angle at a time if using range of wavelength
% ** only use one wavelength at a time if using range of incident angles

% Complex Refractive Index of Silver and Gold
if strcmpi(metal,'silver')
   [rEag_calc,iEag_calc]=getEag(iwave,'Nash');
   e1=rEag_calc+1i*iEag_calc;
elseif strcmpi(metal,'gold')
   [rEau_calc,iEau_calc]=getEau(iwave,'CRC');
   e1=rEau_calc+1i*iEau_calc;
else
   error('Invalid metal interface OR metal interface not programmed')
end

% Refractive index of Air at STP
Na=1.00029;
```

```
e2=(Na)^2;
% Refractive index of BK-7 (Normal Dispersion)
n3=getnBK7(iwave);
e3=(n3).^2;



% Calculate Reflection Using Fresnel's Equation for 3-layer System
k0=2*pi./iwave;
kx=(n3.*k0).*sin(IncidentAngle.*pi/180);
k1z=(e1.*k0.^2-kx.^2).^0.5;
k2z=(e2.*k0.^2-kx.^2).^0.5;
k3z=(e3.*k0.^2-kx.^2).^0.5;
g31=(e1.*k3z-e3.*k1z)./(e1.*k3z+e3.*k1z);
g12=(e2.*k1z-e1.*k2z)./(e2.*k1z+e1.*k2z);

R=(abs((g31+g12.*exp(1i*2.*k1z.*thickness))./...
(1+g31.*g12.*exp(1i*2.*k1z.*thickness)))).^2;
end
%%%%%%%%%%%%%%%%%%%%%%%%%%%%%%%%%%%%%%%%%%%%%%%%

function [nBK7] = getnBK7(iwave)
%
% Get refractive index values as a function of wavelength (nm)
% for BK7 dispersion curve
% Example:
%       n = getnBK7(785)
% or,
%       n = getnBK7(400:1:1000)
%

nwl_rii=[0.3 0.322 0.344 0.366 0.388 0.41 0.432 0.454 0.476...
 0.498 0.52 0.542 0.564 0.586 0.608 0.63 0.652 0.674 0.696...
 0.718 0.74 0.762 0.784 0.806 0.828 0.85 0.872 0.894 0.916...
 0.938 0.96 0.982 1.004 1.026 1.048 1.07 1.092 1.114 1.136...
 1.158 1.18 1.202 1.224 1.246 1.268 1.29 1.312 1.334 1.356...
 1.378 1.4 1.422 1.444 1.466 1.488 1.51 1.532 1.554 1.576...
 1.598 1.62 1.642 1.664 1.686 1.708 1.73 1.752 1.774 1.796...
 1.818 1.84 1.862 1.884 1.906 1.928 1.95 1.972 1.994 2.016...
 2.038 2.06 2.082 2.104 2.126 2.148 2.17 2.192 2.214 2.236...
 2.258 2.28 2.302 2.324 2.346 2.368 2.39 2.412 2.434 2.456 2.478 2.5];

n_rii=[1.552770264 1.545869929 1.540446687 1.536090528...
 1.532527732 1.529568767 1.527078429 1.524957846 1.523133174...
```

```
 1.521548253 1.520159688 1.518933478 1.517842648 1.516865557...
 1.515984669 1.515185645 1.51445666 1.51378789 1.513171112...
 1.512599402 1.512066895 1.51156859 1.511100206 1.510658057...
 1.510238956 1.509840135 1.50945918 1.509093978 1.508742673...
 1.508403627 1.508075392 1.507756683 1.507446357 1.507143392...
 1.506846874 1.506555982 1.506269979 1.505988198 1.505710037...
 1.50543495 1.505162442 1.50489206 1.504623394 1.504356065...
 1.50408973 1.503824072 1.503558798 1.503293642 1.503028354...
 1.502762706 1.502496485 1.502229493 1.501961547 1.501692477...
 1.501422121 1.501150331 1.500876967 1.500601898 1.500324999...
 1.500046155 1.499765255 1.499482196 1.499196879 1.498909211...
 1.498619104 1.498326472 1.498031236 1.497733318 1.497432645...
 1.497129146 1.496822753 1.4965134 1.496201026 1.495885568...
 1.495566968 1.49524517 1.494920117 1.494591757 1.494260036...
 1.493924904 1.49358631 1.493244207 1.492898546 1.49254928...
 1.492196363 1.49183975 1.491479396 1.491115257 1.490747289...
 1.49037545 1.489999697 1.489619988 1.48923628 1.488848531...
 1.488456702 1.488060749 1.487660633 1.487256312 1.486847745...
 1.486434891 1.48601771];

kwl_rii=[0.3 0.31 0.32 0.334 0.35 0.365 0.37 0.38 0.39 0.4 0.405...
 0.42 0.436 0.46 0.5 0.546 0.58 0.62 0.66 0.7 1.06 1.53 1.97 2.325 2.5];

k_rii=[2.86E-06 1.37E-06 6.66E-07 2.64E-07 9.29E-08 3.42E-08...
 2.74E-08 2.07E-08 1.37E-08 1.02E-08 9.06E-09 9.39E-09 1.11E-08...
 1.03E-08 9.58E-09 6.97E-09 9.25E-09 1.19E-08 1.26E-08 8.93E-09...
 1.01E-08 9.84E-08 1.09E-06 4.29E-06 8.13E-06 ];

nBK7=interp1(1000*nwl_rii,n_rii,iwave,'spline');
end
%%%%%%%%%%%%%%%%%%%%%%%%%%%%%%%%%%%%%%%%%%%%%%%%%%%%%%%%

function [rEag,iEag]=getEag(iwave,ref)
% Get Real and Imaginary part of dielectric function for SILVER
% from Nash and Sambles Artical OR CRC values
% Accepted wavelength range 450 nm to 900nm for Nash and Sambles
% Accepted wavelength range 382 nm to 1239 nm for CRC

if nargin < 2
  ref = 'Nash';
end
if strcmpi(ref,'Nash')
        NS(:,1)=[450;475;500;525;550;575;600;625;650;675;700;725;750;...
     775;800;825;850;875;900];
```

```
        NS(:,2)=[-7.16;-8.58;-9.98;-11.55;-13.19;-14.8;-16.4;-18.18;...
    -19.93;-21.92;-23.13;-25.23;-26.72;-29.38;-30.07;-32.78;...
    -34.99;-36.16;-38.83];
        NS(:,3)=[0.28;0.31;0.34;0.35;0.39;0.41;0.44;0.43;0.58;0.52;...
    0.59;0.69;0.7;0.86;0.95;1.06;1.14;1.16;1.35];

        mu = 675;       sigma = 140.68;
        z = (NS(:,1)-mu)/sigma;
        p1 = -0.49421; p2 = -9.8636;  p3 = -21.583;
        q1 = 0.099486;          q2 = 0.31789;  q3 = 0.56628;

        rEag_calc = p1*z.^2 + p2*z +  p3;
        rEag=interp1(NS(:,1),rEag_calc,iwave,'spline');
        iEag_calc = q1*z.^2 + q2*z +  q3;
        iEag=interp1(NS(:,1),iEag_calc,iwave,'spline');

elseif strcmpi(ref,'CRC')
   wl=[1239.8000 826.5600 619.9200 495.9400 413.2800 381.4900]';
   n4=[0.28 0.27 0.27 0.24 0.23 0.23]';
   k=[9.03 5.79 4.18 3.09 2.27 1.86]';

   Eag=(n4+1i*k).^2;

   realcoef=[-2.02311424321238e-08,-7.14756247707261e-06,...
      -0.0357227659878438,12.3687259955177];
   rEag=realcoef(1)*iwave.^3+realcoef(2)*iwave.^2+...
      realcoef(3).*iwave +realcoef(4);
   iEag=spline(flipud(wl),flipud(imag(Eag)),iwave);
else
                error('Reference not valid')
end

%%%%%%%%%%%%%%%%%%%%%%%%%%%%%%%%%%%%%%%%%%%%%%%%%%%%%%%%%%%%%%%%%%%%%%%%%%%%%%%
```